

An experimental study on flared folding wingtips

Effects of wing stiffness, aeroelastic tailoring and hinge release threshold on gust load alleviation performance

Xavier Carrillo Córcoles



An experimental study on flared folding wingtips

**Effects of wing stiffness, aeroelastic tailoring
and hinge release threshold on gust load
alleviation performance**

by

Xavier Carrillo Córcoles

to obtain the degree of Master of Science
at the Delft University of Technology,
to be defended publicly on Friday, February 25th, 2022 at 09:00 AM.

Student number:	5002613	
Project duration:	February 2021 - February 2022	
Thesis comitee:	Dr. ir. B.W. van Oudheusden,	TU Delft, Chair
	Dr. A. Sciacchitano,	TU Delft, supervisor
	Ir. C. Mertens,	TU Delft, daily supervisor
	Dr. J. Sodja,	TU Delft, ASCM, daily supervisor
	Dr. ir. R. De Breuker,	TU Delft, ASCM, external examiner
	Dr. A. Castrichini,	Airbus UK, Loads & Aeroelastics

An electronic version of this thesis is available at: <http://repository.tudelft.nl/>.

Contents

List of Figures	vii
List of Tables	xi
1 Introduction	1
1.1 Aeroelasticity	2
1.2 Gusts	2
1.3 Gust load alleviation	4
1.3.1 Active alleviation	4
1.3.2 Passive alleviation	5
1.4 Outline	5
2 The Flared Folding Wingtip	7
2.1 History.	7
2.2 The concept.	8
2.3 State of the art	9
2.3.1 Numerical studies	9
2.3.2 Wind tunnel tests	11
2.3.3 Scaled flight tests.	12
2.4 Research questions and objectives	13
2.4.1 Research questions	14
2.4.2 Research objective	15
3 Wing Model Design	17
3.1 Wind tunnel wing model	17
3.1.1 Requirements.	17
3.1.2 Wing characteristics and dimensions	18
3.2 Numerical analysis	19
3.2.1 Finite element model	20
3.2.2 Wing spar design	21
3.2.3 Numerical simulations	27
3.3 Hinge mechanism design	33
3.3.1 Requirements.	33
3.3.2 Design procedure.	33
3.3.3 Hinge prototype and final design	36

4	Experimental Setup and Procedures	39
4.1	Wing model	39
4.1.1	Structural elements	39
4.1.2	Sensors	40
4.2	Data acquisition system	43
4.3	Sensor calibration and data processing	44
4.3.1	Strain gauge calibration	44
4.3.2	Metrics for GLA assessment	47
4.4	Wind tunnel setup	48
4.5	Acquisition strategy	49
4.5.1	Stability analysis: flutter	50
4.5.2	Modal analysis: modal impact test	50
4.5.3	Static loads analysis: bending moment coefficient polars	50
4.5.4	Dynamic loads analysis: 1-cosine gusts	50
5	Results	53
5.1	Stability study: flutter	53
5.2	Modal analysis: modal impact test	54
5.3	Static loads analysis: bending moment coefficient polars	55
5.4	Dynamic load: 1-cosine gusts	56
5.4.1	System characterization	56
5.4.2	GLA performance	58
6	Conclusions and Recommendations	65
6.1	Conclusions	65
6.2	Recommendations	66
6.2.1	Practical tips	66
6.2.2	Future work	67
6.2.3	New research directions	67
A	Set Up of Real-time Measurements	69
A.1	Requirements	69
A.2	Procedure	70
A.2.1	Setting up TestLab	70
A.2.2	Setting up LabVIEW	76
A.2.3	Running a program	80
A.3	Troubleshooting	80
A.3.1	TestLab	80
A.3.2	LabVIEW	81
A.3.3	Running real-time program	82

B Ground Vibration Test	83
B.1 Methodology	83
B.2 Setup	83
B.3 Procedure.	84
Bibliography	87

List of Figures

1.1	Collar’s triangle diagram, representation of load interactions in aeroelastic problems. Retrieved from [23]	2
1.2	Representation of gusts in different directions. Retrieved from [53]	3
1.3	Shape of a 1-cosine gust. Retrieved and edited from [53]	3
1.4	Representation of load distribution modification caused by active alleviation system. Retrieved from [32]	4
1.5	Example of a control diagram of an active load alleviation system. Retrieved from [53]	4
1.6	Passive twist load alleviation system. Retrieved from [31]	5
2.1	Representation of the hinge and its flare and fold angles. Retrieved from [14]	8
2.2	Low-fidelity stick-beam structural model coupled to aerodynamic panels solved using DLM. Retrieved from [14].	9
2.3	Schematic of the applied hinge moments. Retrieved from [17]	10
2.4	Wind tunnel models used in the different studies.	12
2.5	AlbatrossONE scaled model. Retrieved from [51]	13
2.6	Position of the folding wingtips depending on operation conditions. Retrieved from [6, 9]	14
3.1	Wing model design procedure	17
3.2	Sketch of wing deflection effects on maximum allowable fold angle	18
3.3	CAD representation of the wind tunnel model without skin with an overview of dimensions	19
3.4	Iterative process used to size the composite plates comprising the wing core.	20
3.5	FE model of the wing with a detail of the rib and the glue connection to the plate. Structural elements represented in green and aerodynamic mesh represented in yellow	20
3.6	Details of the FEM used for the hinge	21
3.7	Force (N) and moment (M) resultants in a laminated composite. Extracted from [19].	22
3.8	Representation of special balanced stacking sequence including $[0,90]_s$ layers in the antisymmetry plane	23
3.9	Comparison of optimized compliance results to UD plate results	24
3.10	Sensitivity analysis comparing the bending compliance, d_{11} , and the bend-twist compliance, d_{16} , normalized with the nominal value.	26
3.11	Comparison of $\tilde{E}_{11}(\theta)$ and $\tilde{D}_{11}(\theta)$. Parameters normalized with maximum value of reference plate, B.	27
3.12	Natural modes shapes from simulation (SOL 103/SOL 145).	29
3.13	Sensitivity analysis of flutter speed to hinge stiffness for the different wings.	29
3.14	Comparison of damping ratio and frequency flutter plots of Wing B at different hinge stiffnesses, K_β	30

3.15 Comparison of damping ratio and frequency flutter plots between wings B, B_{WI} and B_{WO} in locked hinge condition.	31
3.16 Results of gust simulations (SOL 146). Comparison between locked-hinge and free-hinge conditions for different gust frequencies.	32
3.17 Peak WRBM load comparison between plates for different gust frequencies in locked-hinge condition (SOL 146).	33
3.18 Load diagram for hinge moment estimation	34
3.19 Example of bi-stable mechanism used to lock the hinge. Retrieved from [16].	34
3.20 Bending moment coefficient time signal example to illustrate the changes in hinge condition when using a bistable mechanism.	35
3.21 Sketch of the locking mechanism introducing an electromagnet to replace the springs of the bi-stable mechanism.	35
3.22 Sketch of the friction-based locking mechanism. The pin is pressed against the hinge shaft to create friction and lock the rotation of the wingtip.	36
3.23 Reduced model prototype used for testing the hinge mechanism	37
3.24 Detail of the hinge mechanism in free-hinge condition	37
4.1 Details of skin deformation at the different regions of the wing.	40
4.2 Detail of the strain gauge rosette. The directions with respect to the spanwise direction are annotated while their original direction, as named by the manufacturer, is presented between parentheses.	41
4.3 Detail of the electrical connections between strain gauges. Each number represents a connection, giving the number to the strain gauge at the top face of the plate and the number with the apostrophe to the strain gauge at the bottom face of the plate.	41
4.4 Strains on the different strain gauges for pure bending and pure torque loads.	42
4.5 Wing model used in the experiments. Image before assembling the skin of the main wing	42
4.6 Schematic of the data acquisition and control system	44
4.7 Strain gauges calibration test rig	45
4.8 Diagrams of applied loads during the calibration procedure	46
4.9 Strain-Load curves obtained in the calibration procedure to compute the calibration constants	46
4.10 Comparison between applied load and loads computed from the strain gauge signals using the calibration matrices from Table 4.2.	47
4.11 Terminology used for processing the data	48
4.12 Wind tunnel setup	49
4.13 Filtering procedure for dynamic test cases. Example from wing C at $\alpha = 5^\circ$, 3.5 Hz (1st bending natural frequency) and hinge release at 50% of the peak load.	51
5.1 Comparison of flutter speeds at different angles of attack for each wing	53
5.2 Wing B interpolated C_B and β polars	55
5.3 Bending moment coefficient polars comparison between tailored wings	56
5.4 Example of delay between actuator signal release and wingtip response. Example of Wing A, $\alpha = 0^\circ$, 5 Hz gust and 50% release	57
5.5 Comparison of time response for different release thresholds at different gust frequencies. Example from Wing A at $\alpha = 0^\circ$	57

5.6	Relative peak load reduction with respect to peak load in locked hinge condition for $\alpha = 0^\circ$.	60
5.7	Relative peak load reduction with respect to peak load in locked hinge condition for $\alpha = 5^\circ$.	61
5.8	Bending moment coefficient time response examples	62
5.9	Relative RMS reduction with respect to peak load in locked hinge condition for $\alpha = 0^\circ$.	63
5.10	Relative RMS reduction with respect to peak load in locked hinge condition for $\alpha = 5^\circ$.	64
A.1	Representation of the ESO64 card	70
A.2	Modifications required on the "TRMConfig.xml" file	72
A.3	Instructions to modify "RemTRM" configuration	72
A.4	Instructions to share the "TurbineTesting" folder	73
A.5	Instructions to follow in the "Turbine Test Recording Manager" application	73
A.6	Instructions in the "HighSpeedTimeDataRecordingStandard", steps 1 to 3	74
A.7	Instructions in the "HighSpeedTimeDataRecordingStandard", steps 4 to 9	75
A.8	Setting the IP Address for the Real-Time Controller.	77
A.9	Installing Software on the Real-Time Controller.	78
A.10	Selecting EtherCAT Mode for the Ethernet Port of the Real-Time Controller.	78
A.11	Using LabVIEW to discover controllers connected to the network.	79
A.12	Selecting the EtherCAT Master Port on the Real-Time Controller.	79
A.13	Final look of the LabVIEW project after configuring the EtherCAT network.	79
A.14	Sketch of connections between elements in the network.	80
A.15	The program to run should be saved under the chassis node (EtherCAT Master).	80
A.16	Dragging I/O variables from the LabVIEW project to the block diagram	81
A.17	Error message when the ADC bandwidth is not set up correctly	81
A.18	Error message when mapping a disabled channel	81
B.1	Test setup used for the GVT using the SLDV system.	85
B.2	Detail of the setup seen from behind including a grid with the measurement points and the point where the excitation is applied.	85

Some figures retrieved from external sources have been modified to keep consistency with the nomenclature used in this document. This modification mainly affects the folding angle, β (θ in the references), which might be confused with the ply angle from Composite Laminar Plate Theory, θ .

List of Tables

2.1	Comparison of wing root bending moment alleviation capabilities of different load alleviation methods.	10
3.1	Overview of model dimensions	19
3.2	Stacking sequence of the best results of the optimization problem	24
3.3	Results of the sensitivity analysis	25
3.4	Stacking sequence of the wing core plates. Defined using reference system from Figure 3.3.	26
3.5	Overview of bending compliance and coupling terms of the wing core plates	27
3.6	Comparison between wings of natural frequencies of first modes of free hinge (flapping) and locked hinge (locked) conditions (SOL 103/SOL 145).	28
3.7	Instability speed comparison between wings in free-hinge and locked-hinge conditions (SOL 145).	29
3.8	Maximum vertical displacements from static simulations (SOL 144).	32
3.9	Overview of hinge mechanism characteristics, where '+' means that the property is satisfied as desired, '0' indicates the property is satisfied but could be improved and '-' means the property is not satisfied.	35
4.1	Calibration constants (Equation 4.4) of each wing computed using the least-squares (LS) methodology.	46
4.2	Comparison of maximum relative error between the calibrated measured load and the applied load	47
4.3	Overview of test cases	51
5.1	Comparison between experimental and simulated flutter speeds at $\alpha = 0^\circ$	54
5.2	Comparison of natural frequencies obtained from modal impact test and simulation	55
5.3	Slopes and stall angles obtained from C_B polars. Slopes presented in counts ($C_B = 0.0001 = 1$ count)	55
5.4	Comparison between gust periods and time delays introduced during the release	57
A.1	Software requirements for real-time system setup	70

Nomenclature

Acronyms

AR	Aspect Ratio
CAD	Computer Aided Design
CFD	Computational Fluid Dynamics
CLPT	Classical Laminar Plate Theory
DAQ	Data Acquisition
DASML	Delft Aerospace Structures and Materials Laboratory
DLM	Doublet Lattice Method
DOF	Degree of Freedom
EASA	European Aviation Safety Agency
EU	European Union
FAA	Federal Aviation Administration
FEM	Finite Element Model
FFWT	Flared Folding Wingtip
GA	Genetic Algorithm
GLA	Gust Load Alleviation
GVT	Ground Vibration Test
LCO	Limit Cycle Oscillation
LMS-VLM	LMS Virtual Lab Motion
PSD	Power Spectral Density
RMS	Root Mean Square
SAH	Semi Aeroelastic Hinge
SAW	Spanwise Adaptive Wing
SLS	Selective Laser Sintering
UD	Unidirectional
UVLM	Unsteady Vortex Lattice Method
WRBM	Wing Root Bending Moment

Symbols

α	Angle of attack	[°]
β	Fold angle	[°]

δ_g	Gust amplitude	[°]
γ	Ply angle misalignment	[°]
Λ	Flare angle	[°]
μ	Normal distribution average	[–]
μ_f	Friction coefficient	[–]
\bar{C}	Inverse strain gauge calibration matrix	[N · m/V]
\bar{c}	Strain gauge calibration matrix	[V/N · m]
ρ	Air density	[kg/m ³]
σ	Normal distribution deviation	[–]
θ	Ply angle	[°]
\tilde{D}_{11}	Engineering bending modulus of elasticity	[N · m]
\tilde{E}_{11}	Engineering modulus of elasticity	[N/m]
ε_i	Constrain threshold of optimization problem	[–]
A	Wing area	[m ²]
B	Wing semi-span	[m]
b	Main wing semi-span	[m]
B'	Wingspan	[m]
c	Chord	[m]
C_B	Bending moment coefficient	[–]
C_{Di}	Lift induced drag	[–]
C_l	Section lift coefficient	[–]
f	Wingtip length	[m]
G	Strain gauge bridge signal	[V]
H	Gust gradient distance	[m]
h	Distance between strain gauges and calibration load point	[m]
K_β	Torsional spring stiffness	[N · m/rad]
K_s	Rotation around s axis	[rad]
l	Distributed lift	[N/m]
M_h	Hinge moment	[N · m]
M_{max}	Hinge moment threshold	[N · m]
M_{spring}	Hinge spring moment	[N · m]
M_s	Torque	[N · m]
M_x	Bending moment	[N · m]
n	Laminate number of plies	[–]

q	Dynamic pressure	[Pa]
Re	Reynolds number	[-]
S	Semi-wing area	[m ²]
t	Time	[s]
$t_{release}$	Hinge release instant	[s]
t_{rel}	Hinge release instant	[s]
U	Gust peak velocity	[m/s]
U_{∞}	Wind tunnel airspeed	[m/s]
V	Gust encounter freestream velocity	[m/s]
V_e	Gust encounter total velocity	[m/s]
W	Calibration weight	[N]

Introduction

Nowadays, society is increasingly aware of the effects of climate change, which is reflected in the efforts of the governments in reaching a consensus on how to address the problem, like the Paris agreement [41] or the European Green Deal [24].

The latter deal aims to set the next steps of the European Union (EU) to develop its society and economy sustainably, with a final objective of having no net emissions of greenhouse gases by 2050. One of the contributors to this impact is the transportation sector, for which the deal sets ambitious milestones in all the means of transportation. For aviation, the objective is to have zero-emission large aircraft available by 2035 [25], including the whole life-cycle, from design and manufacturing to the end-of-life. In this thesis, a solution related to the reduction of the operational emissions of the aircraft is studied.

The first way of reducing aircraft emissions is by modifying its propulsion plant: combustion engines powered by fossil fuels have limited efficiency and present the problem of emissions, hence alternative approaches are being studied. On the one hand, current engines could be substituted with hybrid-hydrogen powered engines, like in the ZEROe concepts presented by Airbus [1], which are more efficient than combustion ones and could eliminate the emission of greenhouse gases. On the other hand, current jet fuels could be replaced with more sustainable alternatives like biofuels and electro-fuels.

Another approach to reducing emissions is the improvement of the aerodynamic efficiency of the aircraft. By reducing the drag resistance that is generated, less energy is required to move the aircraft, hence less fuel needs to be burned. In general flight conditions, an important component of the resistance is lift induced drag, C_{Di} , which is inversely proportional to the aspect ratio (AR) of the wing [11]. Looking at the definition of AR in Equation 1.1 and its effect on the drag in Equation 1.2, it can be seen that increasing the wingspan, B' , would be beneficial for emissions.

$$AR = \frac{Wingspan^2}{Area} = \frac{B'^2}{A} \quad (1.1)$$

$$C_{Di} \propto \frac{1}{AR} \propto \frac{1}{B'^2} \quad (1.2)$$

Finally, reducing the weight of the aircraft would also help with the emission reduction objective, as the energy consumption would be reduced or the payload, i.e. passengers, could be increased. Therefore, aircraft would become more efficient by reducing the fuel consumption per passenger.

In this document, a solution that affects both the aerodynamics and structure of the aircraft is presented: the flared folding wingtip (FFWT). An increase of the wingspan, as previously presented, would not only have an impact on the aerodynamics but also other aspects like the structure, the handling qualities or operation in airports, as the increase in wingspan could imply a change in the ICAO classification of the aircraft [3], leading to an increase in airport fees and limitations on the airports at which

the aircraft can operate, which goes against the interest of the airlines. However, the flared folding wingtip could solve part of these problems.

As will be seen in the following chapters, this system would fold the wingtip to fulfil gate requirements on land and then extend the wing for improved aerodynamics during flight. Furthermore, it could also help to reduce the impact on the structural design of the aircraft by alleviating the loads in case of gust encounter, one of the critical load cases used for sizing the structure.

Nevertheless, before addressing the concept and its benefits, the following sections present an introduction to the concepts of aeroelasticity, gusts and gust load alleviation, which are relevant to understanding the operational aspects of the FFWT. To conclude this chapter, the outline of this document is presented.

1.1. Aeroelasticity

Aeroelasticity is the field that studies the interaction between structures and the surrounding airflow. These interactions can be represented with Collar's triangle [23], shown in Figure 1.1. The diagram is a representation of the forces involved in aeroelastic problems and how each problem, like gusts, is connected to them. First, the aerodynamic forces are those caused by the interaction with the flow. Second, elastic forces arise from the structural properties of the studied object and appear when it is subject to deformation. Finally, inertial forces are related to the acceleration and mass of the object.

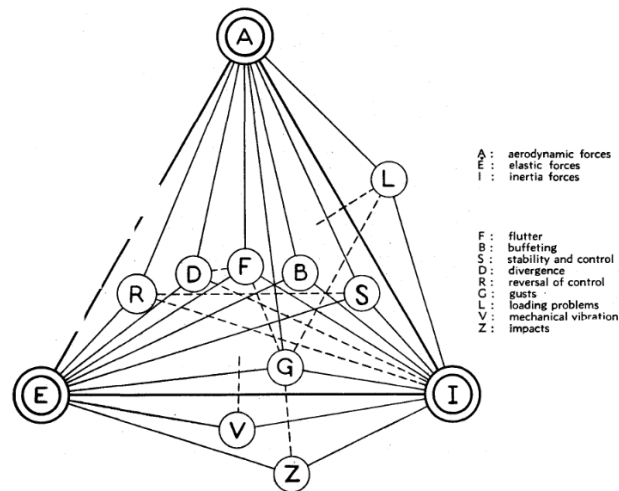


Figure 1.1: Collar's triangle diagram, representation of load interactions in aeroelastic problems. Retrieved from [23]

As can be seen in the diagram, gusts (G) involve all of the forces: aerodynamic (A), elastic (E) and inertial (I). A gust is a perturbation of the flow that modifies the aerodynamic loads, as will be seen in the following section. This variation changes the deformation produced on the wing, which will have an impact on the elastic forces. Furthermore, since gusts are a dynamic event, inertial forces will act as well.

These relations show that, although the structure could be safe in regular conditions, an overload produced by a gust could lead to failure. For this reason, aircraft manufacturers design the structure of the wing conservatively following certification procedures. Therefore, if these overloads could be reduced, lighter structures could be used hence helping towards the zero-emission objective.

1.2. Gusts

Gusts are perturbations of the freestream velocity caused by air currents that can be aligned, or not, with the flow. As represented in Figure 1.2, where gusts perpendicular to the wing plane, parallel to the wing and parallel to the longitudinal axis of the fuselage, namely vertical, lateral and head-on gusts, are presented. There, the mean freestream velocity, V , is combined with the perturbation, U , into the

total velocity, V_e .

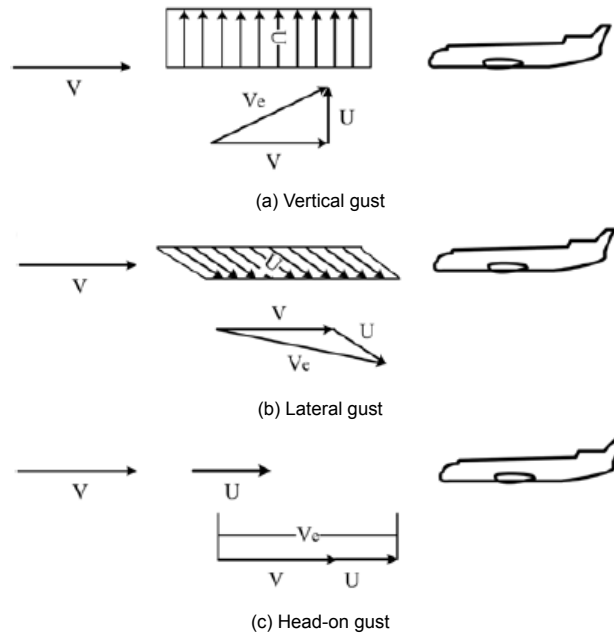


Figure 1.2: Representation of gusts in different directions. Retrieved from [53]

These gusts affect the aerodynamic loads, as they depend on the angle of attack, hence they will modify the handling qualities and the structure, as seen in Figure 1.1. Consequently, they are currently included in the aircraft certification process, defined by agencies like the Federal Aviation Administration (FAA) [8] or the European Aviation Safety Agency (EASA) [7].

Since this process establishes a set of requirements to achieve certification, in both turbulence and discrete gusts, it is necessary to define the gusts that need to be tested. On the one hand, models of the velocity profile for discrete gusts are used. Although other models like sharp-edge or the linear ramp gust are used, this document will only present the 1-cosine gust, which is currently applied in certification and will be later referred to during the document. Its shape, $u(s)$, normalised with the peak velocity of the gust, U , is defined in Equation 1.3 and presented in Figure 1.3, where H is the gradient distance, the distance to the peak velocity [53].

$$\begin{cases} \frac{u(s)}{U} = \frac{1}{2} \left(1 - \cos \frac{\pi s}{H} \right) = \sin^2 \left(\frac{\pi s}{2H} \right) & \text{for } 0 < s < 2H \\ \frac{u(s)}{U} = 0 & \text{for } s < 0 \text{ and } s \geq 2H \end{cases} \quad (1.3)$$

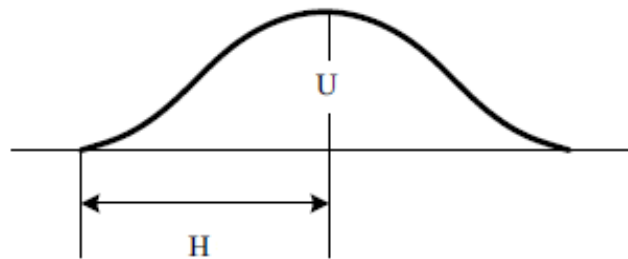


Figure 1.3: Shape of a 1-cosine gust. Retrieved and edited from [53]

On the other hand, it is also possible to represent continuous random gusts, which are more similar to the continuous turbulence that can be found during flight. This turbulence is described with shapes of the gust velocity power spectral density (PSD) like the von Kármán spectrum used in certification [7, 53], which describes the gust variation with frequency.

1.3. Gust load alleviation

Having seen the influence that gusts can have on the critical load cases used to design the wing structure, the next question would be how to reduce its impact. This is known as gust load alleviation (GLA) and has the objective of reducing the overloads produced by gusts. GLA can be achieved by introducing active and passive means of alleviation, which will be presented in subsection 1.3.1 and 1.3.2, respectively.

1.3.1. Active alleviation

Active alleviation occurs when an actuated surface is used to reduce the loads, for example, the wing root bending moment (WRBM). This can be applied to manoeuvres to keep the flight conditions constant, i.e. the lift, but modifying the load distribution for alleviation [32, 53]. An example of this application is presented in Figure 1.4, in which the use of the ailerons reduces the loads near the wingtip, where the lift produces a higher WRBM. Then, to compensate for the reduction in lift, it is necessary to increase the loads near the root, ending with the same total force but a lower root moment thanks to the new lift distribution. Similarly, in the case of a gust encounter, the aileron actuation can adapt to the gust so the peak loads produced by the gust are reduced.

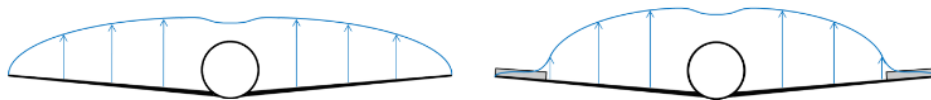


Figure 1.4: Representation of load distribution modification caused by active alleviation system. Retrieved from [32]

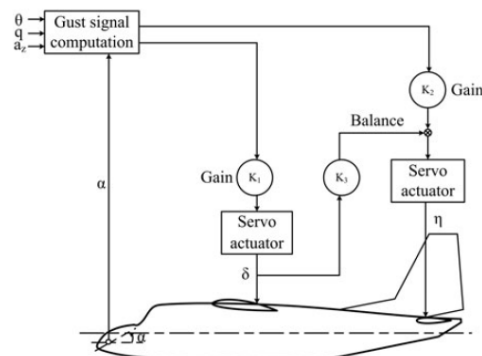


Figure 1.5: Example of a control diagram of an active load alleviation system. Retrieved from [53]

Furthermore, these changes in the position of the ailerons will modify other flight parameters, such as the pitching moment, hence it is also necessary to compensate for this modification with the tail surfaces (considering regular configuration aircraft). To illustrate this action, an example of a simplified control system is presented in Figure 1.5. In a gust encounter, the wing actuators compensate the gust (or manoeuvre) by changing the lift distribution as previously mentioned. As a consequence, the wing will produce an increment of the pitching moment, which has to be corrected by deflecting the tail to produce a reduction of the pitching moment. Therefore, the control system not only needs to actuate the ailerons to provide load alleviation but also balance the aircraft using the elevators.

To conclude, it is important to mention that the type of control system used is a recurrent research topic that will not be further discussed in this document. However, it has been considered important to introduce the active alleviation concept, as some of the studies presented in chapter 2 include active control on the FFWT.

1.3.2. Passive alleviation

Passive alleviation is achieved with systems or designs that do not require control. Therefore, the alleviation capabilities of the design rely on the aerodynamic and structural forces: when the structure is loaded, its deformation leads to a new aerodynamic state that alleviates the loads. This behaviour can be illustrated with the next two examples.

The first example is the passive twist wingtip presented by Guo et al. [31], shown in Figure 1.6. This system separates the wingtip and connects it to the wing with a sprung shaft, allowing rotation around the wing axis. Since the aerodynamic centre is located behind the shaft, an overload would produce a nose-down rotation, reducing the local angle of attack, hence the loads, also known as wash-out response. With a similar behaviour, the FFWT studied in this document would also be considered a passive system.

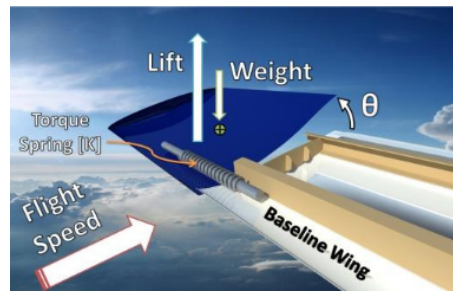


Figure 1.6: Passive twist load alleviation system. Retrieved from [31]

Another way of achieving alleviation is by designing the structure to reduce the loads when it deforms. This would be a form of aeroelastic tailoring, which Shirk et al. [45] define as:

“The embodiment of directional stiffness into an aircraft structural design to control aeroelastic deformation, static or dynamic, in such a fashion as to affect the aerodynamic and structural performance of that aircraft in a beneficial way.”

Therefore, using the passive twist wingtip as a reference, the idea would be, for example, to design the structure in such a way that it produces a wash-out response to reduce the loads. An example of aeroelastic tailoring can be found in the work of Krüger et al. [40], in which the directional properties of composites are used to optimize the weight of the structure. In their study, it is shown that, by making use of anisotropic laminates, it is possible to reduce the structural weight by 30% with respect to a structure with quasi-isotropic laminates. Similarly, the anisotropy of the laminates can be used to control the aeroelastic response of the wing and achieve load alleviation or control the stability of the wing, as presented by Weisshaar [47].

1.4. Outline

This chapter has introduced the FFWT and how it can help achieve zero-emission flights. Next, chapter 2 presents the history and working principles of the FFWT. In addition, it presents a review of the state of the art, from which the research questions and the research objective of this thesis are defined.

These research objectives are addressed with an aeroelastic wind tunnel experiment, hence the design of the wing model and the procedure followed to define its structural properties according to the wind tunnel constraints are presented in chapter 3. Subsequently, chapter 4 describes the wind tunnel facilities, the experimental setup and acquisition strategy to answer the research questions.

Finally, the results of the experiment are presented in chapter 5. The stability analysis and modal analysis are presented first to define the test conditions and assess the results of the numerical model used for the structural design. Then, the research questions are addressed with a study of the wing under static loads and 1-cosine gusts. Last, the answers to the research questions are presented in the conclusions of chapter 6 followed by a series of recommendations for future work.

2

The Flared Folding Wingtip

This chapter focuses on the FFWT concept presented by Airbus as a GLA system. For a better understanding of the concept, section 2.1 presents the history of the folding wingtip and the different applications it can have. Then, section 2.2 introduces the working principles of the FFWT to later review the state of the art of the technology in section 2.3. Finally, based on this review, section 2.4 presents the research questions and the objective that defines this thesis investigation.

2.1. History

The folding wingtip is a concept that has been recently implemented in commercial aviation to increase the efficiency of aircraft but was historically used for other reasons. Therefore, to introduce the context in which the FFWT has been developed, this section will present the history of the folding wingtip and the different applications that the concept was given until it has finally been used as a GLA system [28, 48].

The first time a hinge concept to balance the loads was introduced in aviation was not in a wing but a rotor blade: De la Cierva, the inventor of the autogyro [26], introduced the hinge in the rotor head to allow blade flapping. During the first attempts to make the autogyro fly, it was found that there was a difference of lift between the advancing and retreating blades, which led to a rolling moment that knocked over the aircraft. To solve it, the C.3 autogyro incorporated the hinge at the root of its blades to allow their movement and compensate for this detrimental roll moment. Eventually, this became the foundation of the rotors currently used in helicopters.

Years later, during World War II, the folding wing concept was introduced in naval aviation. Due to the limited space on aircraft carriers, most aircraft had a specific version for these conditions which included a folding wing for better space management. Nowadays, this application has been extended to helicopters, that can align all their blades with their airframe, and other hinge concepts like that of the Grumman F-14, which can modify the sweep of the wing to adapt to flight conditions and use the same system to reduce the space taken when landed.

Furthermore, some prototypes were designed to study the flight performance enhancement produced by folding wingtips. One example is the Rey R.1, which included hinged wings to reduce the peak loads in case of gust encounter [44]. Another example is the XB-70, which had hinged wingtips that could adapt in-flight to improve the performance depending on the flight conditions. Later, this concept was reconsidered by NASA [30]. In the Spanwise Adaptive Wing (SAW) project, a scaled model was created to study the enhancement of lateral-directional stability and drag reduction.

To conclude, the commercial aviation industry has started to show interest in this technology and its benefits. On the one hand, Boeing included a folding wingtip in their 777X to extend the wingspan in-flight and fulfil the gate requirements on land by folding the wingtip [46]. On the other hand, Airbus is studying the system in its Semi Aeroelastic Hinge (SAH) project, which incorporates the FFWT in the AlbatrossONE scaled model [51]. In this project, Airbus is working on the concept of a folding wingtip

used for load alleviation. Starting with a patent of a "Wingtip device" [37], the company has been studying the capabilities of such a system in collaboration with the academic world. The final objective is to understand the effects of this system and include it in the design of the next generation of aircraft. Eventually, these studies have led to a second patent of "An aircraft wing with a moveable wingtip device for load alleviation" [49]. As will be explained in the following subsections, the concept could provide load alleviation in gust encounters, reduce the adverse effects that increasing the wingspan has on the roll capabilities, or reduce the wingspan on land to fulfil gate requirements.

2.2. The concept

As seen before, there is an interest in extending the wingspan to improve the aircraft aerodynamic efficiency. However, this extension also has an adverse effect on the aircraft design, as the higher loads will lead to a heavier structure to carry the loads and the higher wingspan will reduce the roll rate, hence the manoeuvrability. In addition, there are practical constraints such as gate requirements in the airports, which limit the dimensions of the aircraft. The FFWT is a possible solution to these problems.

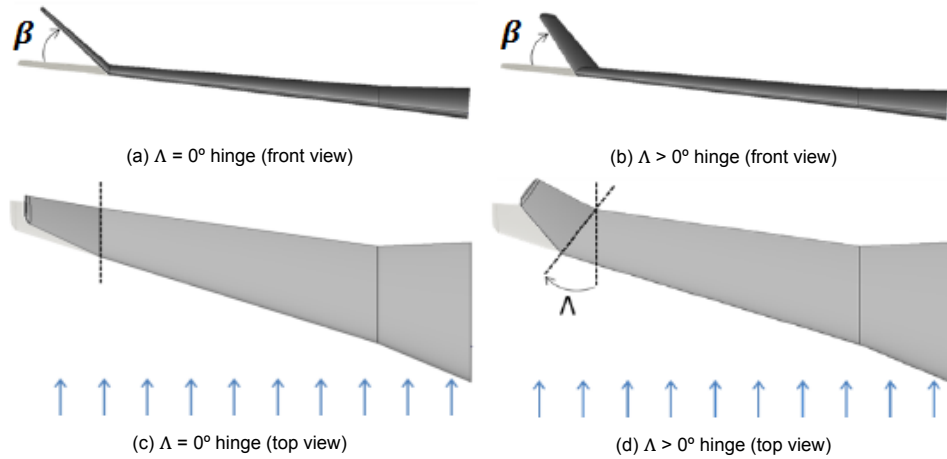


Figure 2.1: Representation of the hinge and its flare and fold angles. Retrieved from [14]

The idea is to introduce a hinge at an angle, Λ , with respect to the freestream direction, referred to as flare angle, as presented in Figure 2.1. Due to this misalignment, when the wingtip folds, with a fold angle β , there is a variation in the local angle of attack, $\Delta\alpha$. This variation is defined by Equation 2.1, which assumes small fold angle deflections and shows that a positive flare angle would provide a method to reduce the angle of attack and thus the loads [14].

$$\Delta\alpha = -atan(\tan\beta\sin\Lambda) \quad (2.1)$$

Focusing on its application, the system would be used similarly to that of the Boeing 777X but including the in-flight load alleviation: in case of overload, like in gust encounters, the hinge could be released to let the wingtip move freely. Then, thanks to the free rotational degree of freedom of the hinge, the moment created by the loads would fold the wingtip until it achieves a stable position in which the weight of the wingtip compensates for the aerodynamic load and no moment is transferred to the main wing. This way, the peak WRBM produced by the gust would be alleviated. After the overload condition has passed, the wingtip would recover the horizontal position for improved efficiency during cruise flight.

Due to this promising principle, several studies have been carried out to assess the load alleviation capabilities as well as the effects on the flight performance of the aircraft. As already mentioned, these studies are addressed in the following section.

2.3. State of the art

The first studies on the FFWT concept are performed with numerical simulations to explore the system capabilities and set the baseline for future work. Afterwards, given the promising results seen in the simulations, the concept is further investigated not only numerically but also in wind tunnel tests and test flights carried out with a scaled model. In this section, the main outcomes of these studies are presented. First, subsection 2.3.1 presents the preliminary numerical studies and the continuation of these investigations using different numerical tools. Next, subsection 2.3.2 presents the wind tunnel studies used to validate and extend the results obtained numerically. Finally, subsection 2.3.3 presents the AlbatrossONE and the flight tests conducted with this scaled model.

2.3.1. Numerical studies

Initially, the FFWT is studied using low-fidelity and high-fidelity models to assess the impact of this concept on load alleviation capabilities and its effects on the stability of the aircraft. On the one hand, Castrichini et al. use the model presented in Figure 2.2 [14], which is a stick-beam structural model that is coupled in MSC Nastran to aerodynamic panels solved with the Doublet Lattice Method (DLM). On the other hand, Pattinson et al. use a flexible multi-body dynamics solver coupled to a Computational Fluid Dynamics (CFD) aerodynamic solver [42].

The results of these preliminary studies are in agreement and show that the FFWT is capable of reducing the WRBM when the wingtip is free to rotate, which would allow increasing the AR of the aircraft with a reduced detrimental impact on the critical load cases. Therefore, considering the effects of increasing the AR seen in chapter 1, this concept could be used to increase the aerodynamic efficiency or to reduce the weight of current aircraft, as the load alleviation would allow lighter structures. In addition, the GLA performance of the concept can be compared to other load alleviation methods. In Table 2.1, the results presented by Castrichini et al. are compared to the passive twist system presented in section 1.3 and active alleviation in a C-5A aircraft. This comparison shows that the FFWT is more promising than the passive twist concept and can achieve WRBM alleviation close to that of active systems. Hence, the FFWT could be combined with active alleviation systems and potentially improve the load alleviation capabilities of the aircraft.

Furthermore, it is found that the flutter speed of the aircraft is reduced by the free hinge but this speed is also sensitive to the flare angle and the mass of the wingtip. Therefore, understanding the impact of the different design parameters on the performance of the system is important to optimize the GLA capabilities while reducing the impact on other aspects, such as the stability or the handling qualities of the aircraft. For this reason, the concept is further studied in the different fields mentioned before.

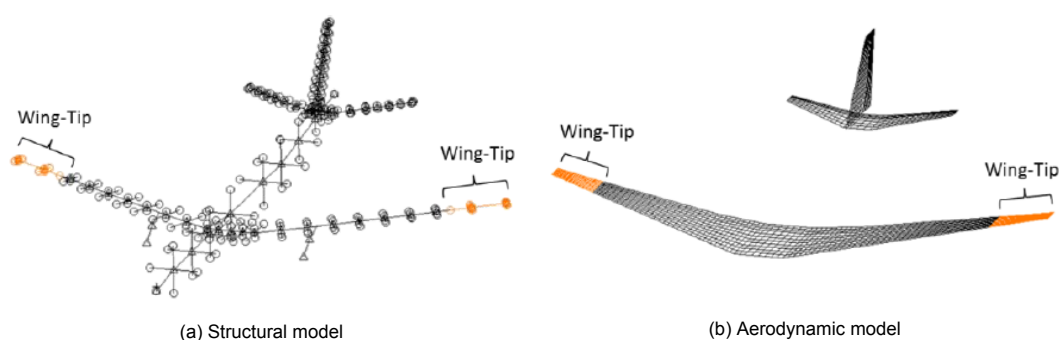


Figure 2.2: Low-fidelity stick-beam structural model coupled to aerodynamic panels solved using DLM. Retrieved from [14].

In the numerical field, the first topic on which the studies focus is the modelling of the aeroelastic problem. On the structural side, Castrichini et al. study LMS Virtual Lab Motion (LMS-VLM), which is a commercial code that allows nonlinear dynamic analysis of rigid and flexible multi-body systems, as an alternative to the linear aeroelastic solver in MSC Nastran [15]. In this study, the LMS-VLM simulation is compared to the previous MSC Nastran model and shows a good correlation in terms of WRBM and wingtip vertical displacement, hence LMS-VLM is a good alternative to previous methodologies.

Table 2.1: Comparison of wing root bending moment alleviation capabilities of different load alleviation methods.

Method	WRBM alleviation	Reference
Active alleviation	30-50%	Wu et al. [53]
Passive twist wingtip	11%	Guo et al. [31]
Flared Folding Wingtip	30%	Castrichini et al. [14]

When it comes to aerodynamic modelling, the wind tunnel tests presented in the following subsection show that the DLM provides limited quantitative agreement in the results, as it is not capable of representing the nonlinearities introduced by the flared hinge. For this reason, Cheung et al. study the Unsteady Vortex-Lattice Method (UVLM) as an alternative aerodynamic model [21]. In this investigation, the UVLM is coupled to the same MSC Nastran structural model as the DLM and the results are compared to the data obtained in the wind tunnel. The comparison reveals a better agreement between the UVLM and the experimental results than the DLM, which shows that the UVLM can better represent the aerodynamics of the FFWT.

Another interesting topic is the instant at which the hinge is released. The previous studies consider the hinge in both released and locked conditions separately but do not address the transition from one to the other. However, since it is desired that the wingtip remains in the planar position during cruise and folds in case of gust encounter, it is necessary to find the optimal release instant and a system capable of automatically recovering the configuration for cruise flight. For this reason, Castrichini et al. present two approaches to study these aspects.

On the one hand, a hinge with piecewise linear stiffness is modelled to study the release instant [17]. Following the reference of Figure 2.3, the hinge stiffness is defined as a release mechanism that is unlocked when a threshold hinge moment, M_{max} , is achieved. Therefore, the hinge moment produced by the spring, M_{spring} , and its stiffness, K_β , are defined by Equation 2.2. Notice that for the locked condition, the stiffness is set to a high order value to convert the hinge into a rigid connection. In contrast, when the hinge is released, the stiffness is given a low order value to model a free rotation but avoiding the numerical divergence that a null stiffness would produce.

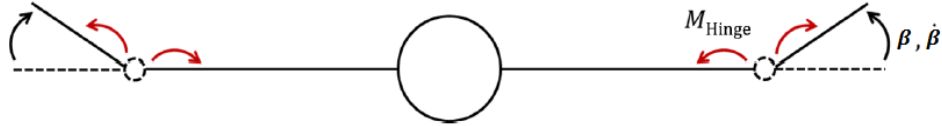


Figure 2.3: Schematic of the applied hinge moments. Retrieved from [17]

$$\begin{aligned}
 & M_{spring} = -K_\beta \beta \\
 & \begin{cases} K_\beta = 1.E^{12} \text{Nm/rad} & \text{if } K_\beta \beta \leq M_{max} & \text{and } 0 < t < t_{release} \\ K_\beta = 1.E^0 \text{Nm/rad} & \text{if } K_\beta \beta > M_{max} & \text{and } t \geq t_{release} \end{cases} \quad (2.2)
 \end{aligned}$$

In this study, it is found that the higher the load threshold, the worse the load alleviation capabilities of the FFWT. Taking into account the load response, a high threshold delays the release of the hinge, hence allowing the loads to increase more before starting the alleviation. Therefore, the release instant is critical for a good performance of the FFWT or, considering the final application, the effectiveness of the system depends on the time it takes between detecting the gust and releasing the wingtip.

On the other hand, a high-static low-dynamic stiffness hinge with a snap-through mechanism is studied as a system capable of recovering the planar position [16]. Accordingly, the objective of this nonlinear spring is to adapt to the flight conditions, keeping the hinge stiff enough in cruise conditions to remain in planar position and allowing a fast response in case of gust encounter. These capabilities are assessed in simulations of 1-cosine gusts and the results show that the system is capable of providing load alleviation and recovering the planar position. However, as it happened with the piecewise linear hinge, the GLA capabilities are sensitive to how fast the wingtip reacts to the gust. In conclusion, both studies show that optimizing the release strategy is a key factor for the load alleviation capabilities of the wingtip.

Thirdly, the impact of the FFWT on the handling qualities of the aircraft is of great interest, as they are also part of the certification process. Due to the increase in wingspan, the roll rate of the aircraft is reduced. However, as found by Castrichini et al. [18] and Dussart et al. [29], releasing the wingtip can help to recover the roll capabilities lost with the increased wingspan.

In these studies, a wing without extension is compared to a wing with the FFWT extension in both locked and released configurations. As expected, the roll rate achieved by the wing with extension in the locked condition is lower than that of the wing without extension. However, when the wingtips are free to rotate, the roll rate reduction caused by the extension is reduced, hence the free wingtips provide a means of restoring the roll capabilities.

Finally, the preliminary studies showed the impact of the FFWT on the flutter speed. For this reason, Wilson et al. study the effects of the folding wingtip on the stability of the aircraft. On the one hand, the influence of the flare angle, the wingtip mass and the position of the hinge on the flutter speed is studied with a low-fidelity model like the one seen in Figure 2.2 [48]. In agreement with the previous studies, it is found that the flutter speed is reduced when the wingtip is free to rotate. Nevertheless, this effect can be mitigated with the proper design of the wingtip.

On the other hand, the nonlinear aeroelastic response of the FFWT is studied with a simplified beam model to assess the possibility of the wingtip entering a Limit Cycle Oscillation (LCO) [50]. In this case, it is found that the appearance of LCOs depends on the structural properties of the main wing. Therefore, it is necessary to consider the wingtip and the main wing simultaneously when studying the dynamic behaviour of the FFWT.

In conclusion, the numerical studies show the complexity behind the FFWT and highlight the importance of further studying the concept. This way, the design could be optimized to reduce the drawbacks that it might have on the dynamics of the wing while maximizing the benefits such as the GLA capabilities or the improved roll rate.

2.3.2. Wind tunnel tests

As already mentioned, the wind tunnel studies are used to validate the results obtained from the numerical simulations and study aspects that can be harder to model, like an actuated wingtip. With this in mind, Cheung et al. use three different models, presented in Figure 2.4, to investigate some aspects seen in the numerical studies.

The first of these models, presented in Figure 2.4a, is used to study the load alleviation capabilities of the FFWT and validate the numerical models used in the preliminary studies [20]. As mentioned before, the GLA capabilities are confirmed but the agreement of the results with those obtained with the DLM aerodynamic model is limited. Furthermore, the results show the sensitivity of the GLA to the direction of the gust, as gravity produces a restoring force in the upward movement of the wingtip and a destabilising one when it is moving downwards.

Secondly, a high aspect ratio wing with an FFWT and a control surface on the wingtip, referred to as wingtip tab and presented in Figure 2.4b, is studied to assess the effects of active control on the load alleviation capabilities [22]. Accordingly, the wing is tested against different types of gusts while a control signal is sent to the wingtip tab. As a result, it is found that active control can increase load alleviation. However, this capability depends on the timing of the actuation with the gust and in the worst case, in which the actuation is in phase with the gust, the loads can be increased instead of alleviated. Therefore, these results combined with the numerical studies on the release of the hinge show that the success of the FFWT as a load alleviation system depends on the capability of detecting gusts and reacting accordingly.

Last, the third model, presented in Figure 2.4c, is used to study the effects of a released hinge on the roll capabilities [35]. Similarly to the numerical studies, three different configurations of the wing are compared: a reference wing, the same wing with a folding wingtip and the latter with the wingtip locked in the horizontal position. As it happened in the previous studies, it is found that the wing with the locked wingtip has a reduced roll rate with respect to the reference wing. However, when the wingtip is released, the roll rate can increase to up to 80% of the roll rate of the reference wing. In addition, it is found that the recovery of the roll rate capabilities depends on the initial position of the wing, hence

these benefits will vary depending on the manoeuvre that is being performed.

Ultimately, these studies validate the results from the numerical simulations but show that the modelling needs to be improved for better quantitative agreement with the experimental results. Furthermore, the study with the second model presents the opportunity of further improving the GLA capabilities by making use of an active control surface, which could also be used to recover the horizontal position of the wingtip. Finally, the third model shows that the benefits of the FFWT are not limited to the GLA capabilities but the FFWT can also recover the roll capabilities that are lost due to the increase in wingspan.

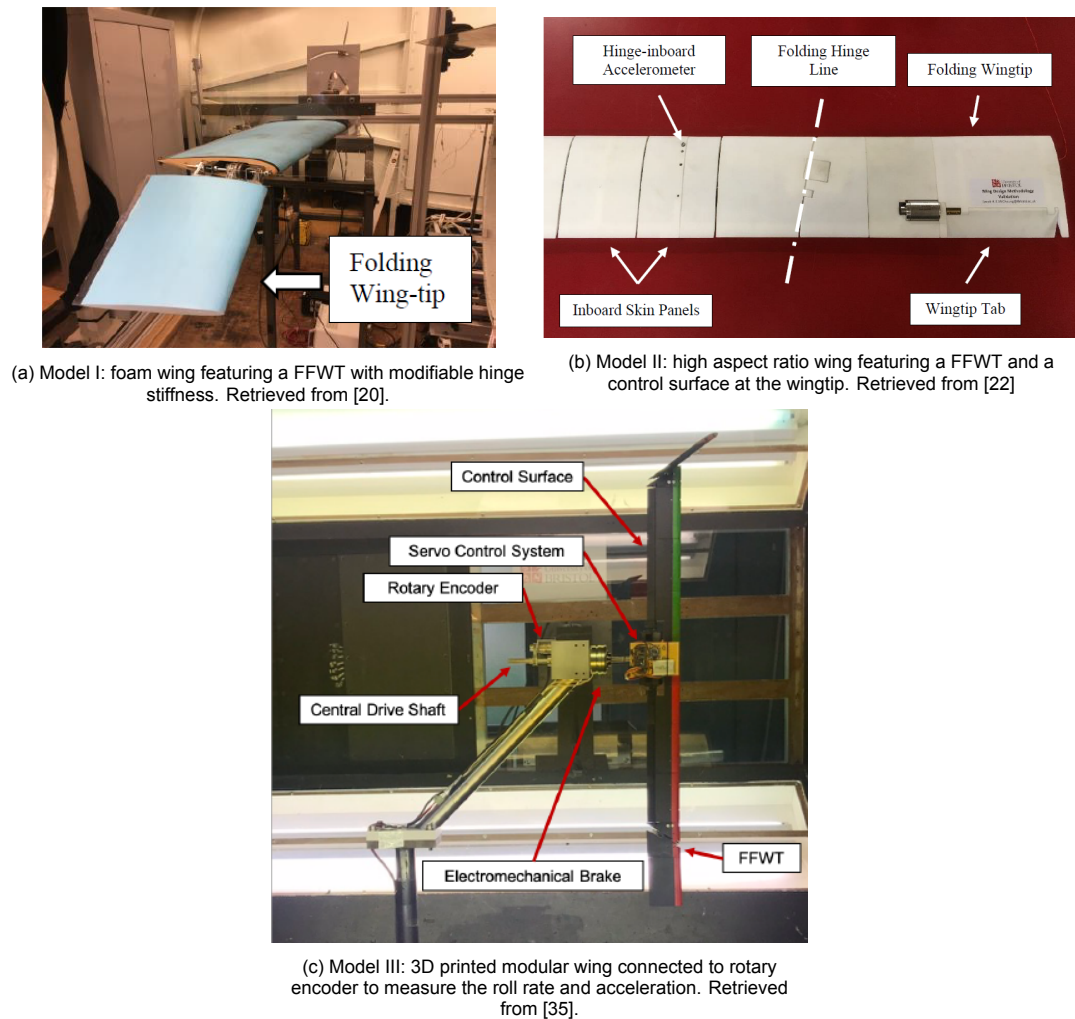


Figure 2.4: Wind tunnel models used in the different studies.

2.3.3. Scaled flight tests

The third method used to study the system is by testing it in flight using a scaled model, the AlbacrossONE [51]. This model, presented in Figure 2.5, is a 1:14 scaled aircraft based on the Airbus A321 with oversized tail surfaces to increase directional stability and a new wing including the FFWT. However, the model is only geometrically scaled, hence its dynamic properties, like the handling qualities or the mass and stiffness properties affecting the aeroelastic response, are not scaled nor does the model fly at the original Mach range. Therefore, the results must be considered qualitatively.

At the present time, two sets of flights have been presented in Airbus promotional videos, one from February of 2019 [4, 10] and the second one from July 2020 [5, 9]. In these videos, an overview of the performed tests and the process before the flight days are presented.



Figure 2.5: AlbatrossONE scaled model. Retrieved from [51]

On the one hand, the results from the first flights are in agreement with the findings from previous studies. The loads are reduced when the wingtip is free to move, hence the FFWT can be used as a means of load alleviation. Additionally, the pilots report not having any particular issues with the aircraft control, which is a good indicator of the aircraft keeping its handling capabilities after the modification.

On the other hand, the second set of flights presents a gate-to-gate demonstration of how this system could be applied in the future. The aircraft has its wingtips in a vertical position during taxiing, as in Figure 2.6a. Before take-off, the wingtips are positioned at 10° and, right before lift-off, the flapping is allowed to improve roll control during the initial manoeuvre. Once the aircraft is flying, the wingtips recover their planar position during cruise flight, as shown in Figure 2.6b, and are released in case of gust encounter, like in Figure 2.6c. Once the aircraft lands, with the same configuration used during take-off, the wingtips recover the vertical position to fulfil the gate requirements.

To conclude, the state of the art review has shown that the current numerical models can provide limited quantitative agreement with respect to experimental results, hence they should be improved for a better prediction of the FFWT response. In addition, the stability and load alleviation capabilities of the FFWT are not only sensitive to the wingtip design but also the structural properties of the main wing. Therefore, given the new designs allowed by the progress in manufacturing technologies (i.e. flexible wings, aeroelastic tailoring), it is important to study the interaction between the main wing and the wingtip in order to assess the final implementation of the FFWT concept in the future aircraft. Finally, the GLA capabilities have a strong dependency on the instant at which the wingtip is released, hence the release instant should be studied to optimize the load alleviation.

2.4. Research questions and objectives

After the review of the state of the art presented in section 2.3, this section presents the research objectives of this thesis and how it will contribute to the development of the FFWT. Given that creating an aeroelastically scaled model of a complete aircraft is beyond the scope of a master thesis and that focusing on improving the numerical model might lead to overlapping with ongoing research, it has been decided to conduct an experimental investigation. Therefore, the thesis will focus on the experimental procedure, from the design of the wing model to the actual experiment in the wind tunnel.



(a) Folding wingtips in vertical position during taxiing



(b) Folding wingtips in horizontal position during cruise



(c) Folding wingtips released for gust load alleviation

Figure 2.6: Position of the folding wingtips depending on operation conditions. Retrieved from [6, 9]

2.4.1. Research questions

In previous studies, it has been seen that the release timing has an important impact on the load alleviation capabilities. In addition, it has also been seen that the structural properties of the main wing affect the stability of the system and can lead to complex responses such as LCOs. Therefore, the stiffness of the wing might also affect the load alleviation capabilities. For this reason, it has been decided to focus the thesis on the interaction between the main wing, the folding wingtip and the hinge release threshold. Accordingly, the research questions and respective subquestions for the thesis are:

1. How does the flexibility of the main wing affect the load alleviation capabilities of the flared folding wingtip?
 - How is the wing root bending moment alleviation affected by the flexibility of the main wing?
2. What is the result of combining the flared folding wingtip and aeroelastic tailoring?
 - How is the wing root bending moment alleviation affected by the directional properties of the main wing?
 - Is the alleviation better when the methods are combined than using them separately?
3. How does the load threshold of the release mechanism affect the load alleviation capabilities of the system?
 - What threshold allows the highest load alleviation?
4. What model would allow studying the previous research questions?
 - How can the stiffness of the wing be modified without major modifications of the model?
 - How can the directional properties of the wing be modified without major modifications of the model?
 - What type of mechanism can allow a parametric study of the load threshold?

2.4.2. Research objective

These questions can be combined to formulate the objective of this thesis as:

“The objective is to study the effects of wing stiffness, stiffness tailoring and hinge release threshold on the gust load alleviation capabilities of a flared folding wingtip by means of an aeroelastic wind tunnel experiment carried out with a parametric wing model.”

This objective can be divided into subobjectives that will define the tasks required to complete the thesis:

1. Design a parametric wind tunnel wing model in which it is possible to modify the following parameters:
 - Wing stiffness
 - Stiffness directional properties
 - Load threshold at which the hinge is released
2. Perform a sizing study to adapt the model to the experiment requirements:
 - Create a numerical model to estimate the results of the experiment.
 - Define the structural properties of the wings required to answer the research questions.
3. Manufacture the wing model according to the results from the second subobjective.
4. Develop a data acquisition and control system that allows the study of the wing model.
5. Design an aeroelastic wind tunnel test and interpret the experimental results to characterise the behaviour of the wing with regard to the first subobjective parameters.
6. Assess the impact of the results on the final implementation of the concept.

3

Wing Model Design

Before the wind tunnel experiment, it is necessary to create a model that can address the research questions posed in section 2.4. Therefore, this chapter presents the wing model used in the experiments and how it was defined. To give an overview of this content, the procedure followed to define and manufacture the model is presented in Figure 3.1. Starting with a CAD model of the Pazy wing, the folding wingtip is implemented by dividing the wing using the characteristics and dimensions presented in section 3.1. Subsequently, two parallel tasks are carried out: the sizing of the composite plates using numerical simulations, addressed in section 3.2, and the design of the hinge mechanism, presented in section 3.3. After testing the mechanism in a prototype of the FFWT and the tip of the main wing, the manufacturing process starts, using the stacking sequences obtained from the sizing analysis and the knowledge obtained from the prototype.

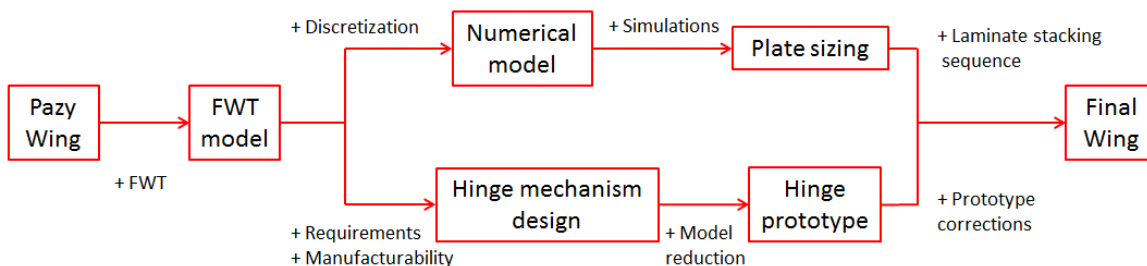


Figure 3.1: Wing model design procedure

3.1. Wind tunnel wing model

This section presents the definition of the wing model that is studied in the wind tunnel. First, subsection 3.1.1 introduces the requirements that the model has to fulfil to address the research objectives. Afterwards, subsection 3.1.2 presents the wing design and its sizing procedure.

3.1.1. Requirements

The objective of this study is to establish the relationship between the stiffness properties of the main wing, the hinge release load threshold, and the GLA performance of the FFWT. For this reason, the model must fulfil two main requirements:

- The design must include a controlled variation of the structural properties.
- A mechanism must allow a controlled release of the hinge based on the load threshold.

In addition to the main functional requirements related to the FFWT and necessary to address the research questions, two more requirements originate from the experimental setup:

- The model must allow the observation of aeroelastic effects pertinent to highly flexible wings (tip deflections above 15% of the semispan) in the wind tunnel.
- The model must remain in the wind tunnel test section, which constrains the size of the model and the magnitude of the structural deformations (maximum allowable tip deflection of 28% of the semispan)

In the following sections, the solutions to the design requirements and the procedure to ensure that the operational conditions are fulfilled will be addressed. Given that these operational requirements conflict with each other, a compromise solution will be necessary.

3.1.2. Wing characteristics and dimensions

From the previous requirements, the wind tunnel test section, with its 40 cm × 40 cm square test section presented in chapter 4, is the most restrictive one. Therefore, to keep the wing within the section at fold angles, β , in the range of $\pm 90^\circ$, the span of the wingtip is limited to 200 mm. Although previous studies show the fold angle range is not necessarily symmetric due to gravity and the direction of the gusts, and the maximum angles are lower than 60° , it is decided to use the broader range to account for the deflections of the main wing. For a static load, the hinge will not necessarily be in the horizontal centerline of the test section, hence the maximum achievable angle will be lower than if the hinge was centred, as sketched in Figure 3.2. Since the deflections are not known at this stage of the design, the 90° constrain is used as an initial magnitude to be verified later in numerical simulations. In addition, taking benefit from the non-symmetrical deflection, the position of the wing could be corrected in the wind tunnel to avoid the wingtip from moving out of the test section.

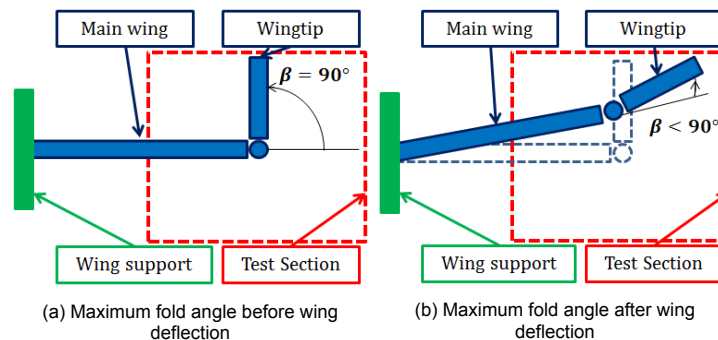


Figure 3.2: Sketch of wing deflection effects on maximum allowable fold angle

Taking these limitations into account, the model is designed as a rectangular half-wing with a chord, c , of 100 mm and a wing aspect ratio (AR) of 14 to maintain similar proportions as the AlbatrossONE but simplifying the geometry to facilitate the parametric study [51]. The main wing has a semi-span, b , of 500 mm and the wingtip extends the full semi-span, B , to a total of 700 mm. In view of the restrictions set by the wing dimensions, a NACA 0018 airfoil is selected to be able to fit the hinge mechanism inside the contour of the airfoil profile. Finally, the flare angle of the hinge, Λ , is set to 15° , as in the AlbatrossONE. The model and an overview of its dimensions are presented in Figure 3.3 and Table 3.1.

With the objective of achieving large deflections at the given size of the model and to easily vary the stiffness properties of the wing, the model is based on the Pazy wing concept proposed by Avin et al. [12]. It consists of a 3D printed chassis covered with shrinking foil to provide the aerodynamic shape to the wing while a plate inside it acts as the primary structural element carrying the majority of the loads. Since the plate represents the primary load-bearing element of the wing, it is possible to effectively control the structural properties of the wing by only modifying the plate. Therefore, the bending stiffness and bend-twist coupling properties can be modified using composite tailoring. Notice then that the plate will need to be replaced between tests or multiple wings with different core plates

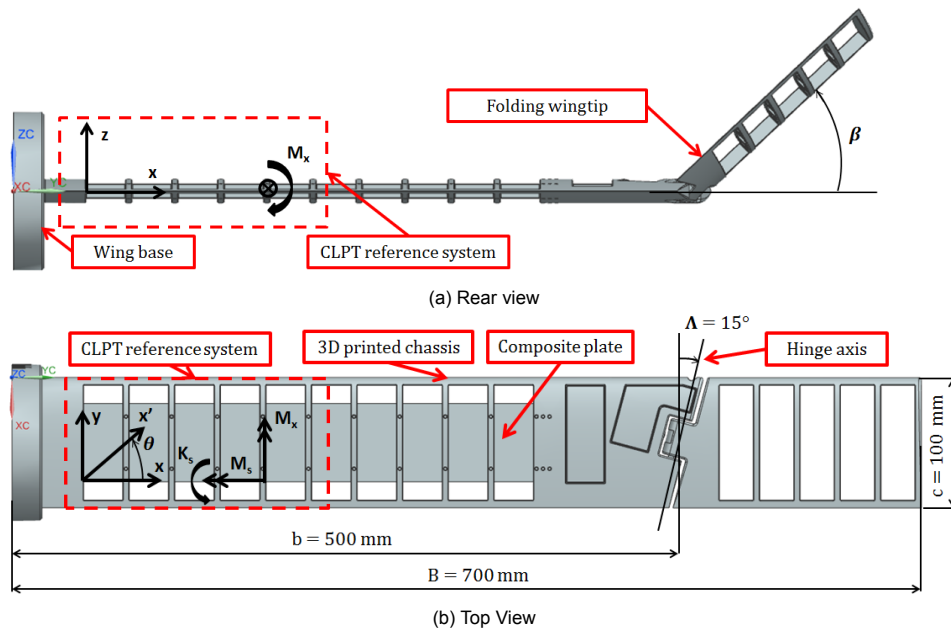


Figure 3.3: CAD representation of the wind tunnel model without skin with an overview of dimensions

Table 3.1: Overview of model dimensions

Symbol	Description	Dimension
Λ	Flare angle	15°
B	Full wing semi-span	700 mm
b	Main wing semi-span	500 mm
c	Chord	100 mm
-	Airfoil	NACA 0018

will need to be manufactured. In this study, different wings have been manufactured to simplify the experimental procedure, as changing the plates would require time and a redesign of the joining method used in the original wing: glueing the plate to the chassis.

3.2. Numerical analysis

The structural design of the wings, in particular the layup of the composite plates acting as the main load-bearing components, requires an assessment of the aeroelastic response to ensure that the desired aeroelastic phenomena can be observed in the wind tunnel. Therefore, the anticipated loads and deflections during the wind tunnel test are studied by performing numerical simulations using Simcenter 3D¹ and MSc Nastran².

This section presents the sizing procedure and the results of the simulations from the final design. A finite element model (FEM), presented in subsection 3.2.1, is obtained from the discretization of the wing presented in the previous section and later used in the simulations to define the plates. Next, the selection procedure of these plates is addressed in subsection 3.2.2 and the numerical results obtained from the final wings are presented in subsection 3.2.3.

Finally, it is important to remark that these numerical studies are conducted iteratively, following the procedure presented in Figure 3.4, to define the wings used for the bending stiffness study. Starting with the CAD model and the respective numerical model, stability simulations are carried out to define

¹“Simcenter 3D,” Siemens, 2021. URL <https://www.plm.automation.siemens.com/global/en/products/simcenter/simcenter-3d.html>, retrieved 25 May 2021.

²“MSc Nastran,” MSc Software, 2021. URL <https://www.mscsoftware.com/product/msc-nastran>, retrieved 25 May 2021.

the speed at which the experiment will be conducted. Subsequently, using this speed, static simulations are used to ensure that the wing is not weight dominated. In the case the wing is weight dominated, the CAD model is updated to reduce its mass. If not, 1-cosine simulations are added to the previous static simulations to assess if the deflections fulfil the maximum and minimum deflection requirements from subsection 3.1.1 or the composite plate needs to be updated. To conclude, using one of the wings of the bending stiffness study as a reference, the optimization process to define the plates for the tailoring study is conducted.

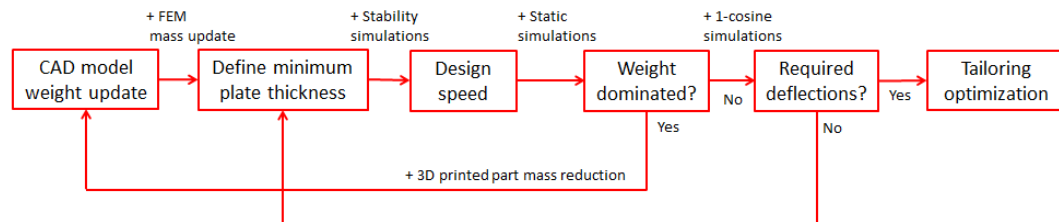


Figure 3.4: Iterative process used to size the composite plates comprising the wing core.

3.2.1. Finite element model

The structure of the wing is modelled using the approach presented by Avin et al. [12]. The leading and trailing edges are modelled as 1D beams while the ribs and the plate are modelled as 2D shells. For the ribs at end of the main wing and the wingtip, where there is no inner plate, ribs are modelled as a single surface. For the other ribs, only the D-shaped part at the front and the rear triangle are modelled and connected to each other with rectangular caps modelled as 1D beams. The glue bonding between the ribs and the plate is modelled using RBE2 1D elements. Finally, the wing skin is modelled as 2D shells. Figure 3.5 shows the FEM representation of the wing without the skin and a detail of a rib and its connection to the plate.

As a simplification of the problem, Avin et al. [12] only modelled the skin when subjected to tensile loads, since buckling of the skin under compressive loads introduces nonlinearities to the analysis. However, both skins are modelled in this sizing study, since the oscillatory motion in the gust response makes both skins face compressive and tensional loads. Therefore, the model becomes stiffer than the real structure when the nonlinearities are ignored so the results are non-conservative.

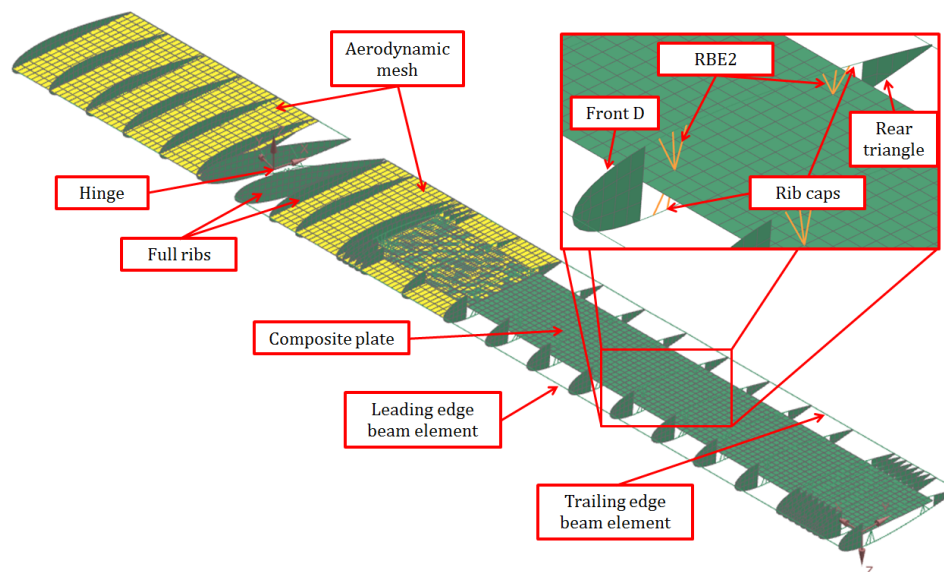


Figure 3.5: FE model of the wing with a detail of the rib and the glue connection to the plate. Structural elements represented in green and aerodynamic mesh represented in yellow

The hinge is modelled following the approach proposed by Castrichini et al. [36]. The FE assembly of the hinge is shown in Figure 3.6. The hinge is modelled using elastic CBUSH elements. Then, RBE2 elements connect the wing and wingtip to the axis nodes and the elastic elements connect both parts, as presented in Figure 3.6. Figure 3.6a shows the FEM representation and Figure 3.6b presents a sketch of the different connections. When the hinge is released, the rotational degree of freedom (DOF) aligned with the hinge spring should be set to zero stiffness, allowing a free rotation. However, this approach leads to a statically underdetermined structure and, ultimately, numerical divergence. To avoid this numerical problem, the stiffness of the rotational DOF is set to relatively low magnitude, two orders of magnitude below the wing stiffness, hence making the spring act similarly to a mechanism. The remaining DOFs are set to relatively high stiffness values, two orders of magnitude above the wing stiffness, to model a rigid connection. On the other hand, when the wingtip is locked, the rotational DOF is also modelled as a rigid connection, hence limiting the rotation of the FFWT.

Finally, the aeroelastic model is completed by coupling the aerodynamic model to the structural model of the wing: Doublet Lattice Method (DLM) is used to determine the aerodynamic forces acting on the wing. As shown by Cheung et al. [20], DLM can only be applied to small deflections of the wingtip, hence only the time up to the hinge release is studied. On the other hand, the results obtained with the free hinge are used for a qualitative comparison. In addition, due to the wind tunnel setup, part of the wing has to be outside of the flow, so the aerodynamic mesh is only defined on the wingtip and the tip of the main wing, as seen in Figure 3.5.

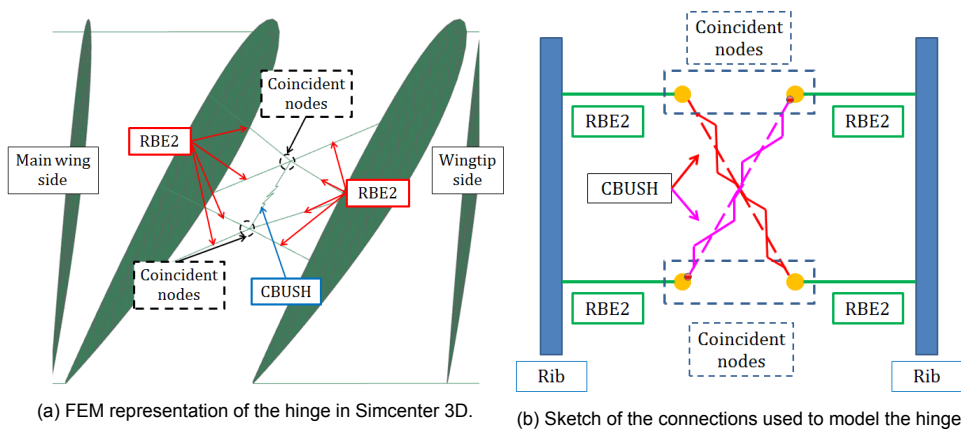


Figure 3.6: Details of the FEM used for the hinge

To conclude, the boundary condition used in the simulations is the same for all the cases: all the nodes at the root are clamped, including the edge of the composite plate. In reality, the plate is clamped to the wing using two metallic supports, hence the DOFs of the root of the plate can be considered fixed as well. Therefore, this connection can be simplified by clamping the plate instead of modelling the wing base and the intermediate parts that fix the plate.

3.2.2. Wing spar design

The wing spar in the form of a composite plate determines the main structural properties of the wing. For this study, five different plates are defined, hence five wings are manufactured. The first three are designed with different bending stiffness to investigate how wing flexibility affects the load alleviation performance of the FFWT. Using one of these plates as a reference, two additional plates are designed with similar bending stiffness but including the bend-twist coupling. The tailored plates are designed to include a wash-in and wash-out response, load enhancing, and load alleviation respectively, so the interaction between different aeroelastic tailoring objectives and the FFWT can be studied. This section presents both the stiffness and tailoring selection procedures and concludes by presenting the final designs.

Classical laminate plate theory

Before addressing the laminate selection procedures, the underlying theory has to be presented. Accordingly, the properties of the laminates are defined using the classical laminate plate theory (CLPT) [19, 39], which establishes the relationships between loads and strains using the properties of each of the plies in the laminate. Therefore, using the reference system from Figure 3.7, CLPT defines the compliance matrix, abd , as the relationship between loads and strains, which is presented in Equation 3.1. As a side note, the orientation of this reference system with respect to the wing model can be found in Figure 3.3.

The abd matrix can be divided into the submatrices a , b and d . First, the matrix a defines the in-plane behaviour of the laminate, introducing shear coupling if the a_{16} and a_{26} terms are not zero. Second, the matrix b defines the in-plane/out-of-plane couplings, which describe how the bending loads affect the in-plane strains and vice versa. Last, the matrix d defines the out-of-plane behaviour, introducing bend-twist coupling if the d_{16} and d_{26} terms are not zero. As will be seen later, matrix d is the main decision criteria in the selection of the stacking sequences used in this study.

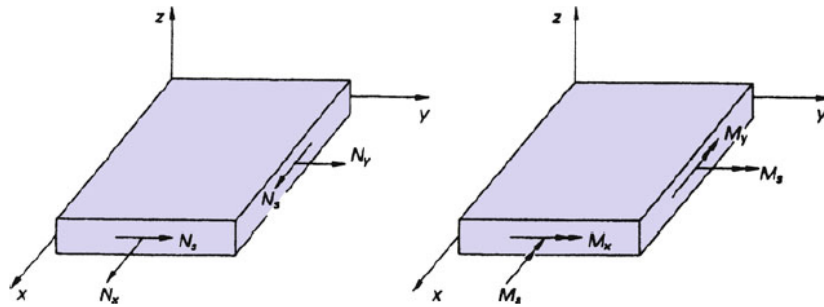


Figure 3.7: Force (N) and moment (M) resultants in a laminated composite. Extracted from [19].

$$\begin{pmatrix} \epsilon_x \\ \epsilon_y \\ \epsilon_s \\ K_x \\ K_y \\ K_s \end{pmatrix} = \begin{pmatrix} a_{11} & a_{12} & a_{16} & b_{11} & b_{12} & b_{16} \\ a_{12} & a_{22} & a_{26} & b_{12} & b_{22} & b_{26} \\ a_{16} & a_{26} & a_{66} & b_{16} & b_{26} & b_{66} \\ b_{11} & b_{12} & b_{16} & d_{11} & d_{12} & d_{16} \\ b_{12} & b_{22} & b_{26} & d_{12} & d_{22} & d_{26} \\ b_{16} & b_{26} & b_{66} & d_{16} & d_{26} & d_{66} \end{pmatrix} \begin{pmatrix} N_x \\ N_y \\ N_s \\ M_x \\ M_y \\ M_s \end{pmatrix} \quad (3.1)$$

Bending stiffness study

For a proper bending stiffness comparison, it is required that all the wings have the same directional properties, avoiding in-plane/out-of-plane couplings and bend-twist couplings, which can be achieved with isotropic materials and changing the stiffness with the thickness of the plate. However, it is decided to use composites for two reasons: i) the thickness can be controlled precisely by changing the number of plies of the laminate and ii) using composites to define these plates allows using one of them as a reference in the tailoring study presented later in this subsection.

Nevertheless, given the anisotropic nature of composites, avoiding the couplings previously mentioned requires of a specific stacking sequence. In this case, special balanced laminates are used to vary the bending stiffness of the first three wings. This stacking sequence is antisymmetric about the mid-plane and, each half is symmetric about its own mid-plane (1/4 plane and 3/4 plane respectively), as shown by Figure 3.8. This combination omits the bend-twist couplings and produces a quasi-isotropic behaviour [39]. Therefore, only the bending stiffness of the plates can be varied by changing the laminate thickness, which is done by adding $[0,90]_s$ layers in the middle plane. As a consequence of this addition, the in-plane quasi-isotropic behaviour is lost, but the out-of-plane quasi-isotropy is conserved. Wings featuring these plates are named A to C, in increasing stiffness order. Finally, the different thicknesses are selected taking into account the deflections obtained from the numerical model to avoid the FFWT moving out of the wind tunnel section, hence the maximum vertical displacements must be below 20 cm, half of the wind tunnel section height.

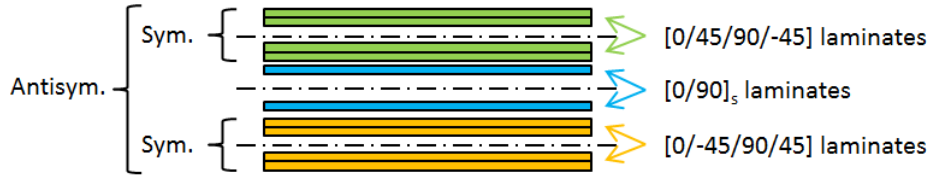


Figure 3.8: Representation of special balanced stacking sequence including $[0,90]_s$ layers in the antisymmetry plane

Stiffness tailoring study

In the tailored wings, symmetric-only laminates are used. Therefore, the in-plane/out-of-plane couplings remain zero thanks to the symmetry but bend-twist couplings appear. The stacking sequence of these laminates is optimized to maximize the bend-twist term of the compliance abd matrix, d_{16} , while keeping the bending compliance term, d_{11} , within $\pm 2\%$ of the reference plate value. Hence, wing B is used as a reference wing, while the wings featuring wash-in and wash-out composite tailoring are designated B_{WI} and B_{WO} , respectively.

According to CLPT [39] and using the reference system introduced in Figure 3.7, for a pure bending load, M_x , a non-zero d_{16} term would produce a rotation, K_s , around the longitudinal axis of the plate, x . Thus, maximizing or minimizing this term maximizes the wash-in or wash-out response, respectively.

The optimization process computes the compliance matrix making use of CLPT using each of the plies as design variables. The total number of plies in the laminate, $2n$, is the same as the reference laminate used in wing B and the sequence is defined as symmetric. Due to this symmetry, the number of design variables is halved to n plies, and the b matrix becomes zero, eliminating the in-plane/out-of-plane couplings. The main constraint of the problem is to achieve bending compliance terms similar to the reference value from wing B, hence the relative difference between the bending compliance terms is constrained to $\varepsilon_{d_{11}}$, equivalent to a 2% difference. In addition, the extension-shear coupling terms of the a matrix, a_{16} and a_{26} , are constrained to a small value, $\varepsilon_{a_{16}}$ and $\varepsilon_{a_{26}}$ respectively, to maintain similarity with respect to the reference plate. Furthermore, the design space is reduced to ply angles in the range of $\pm 90^\circ$ in steps of 15° to simplify the manufacturing process and limit the possible outcome of the optimization.

Given the simplicity of the model and the high number of design variables, the problem is solved using the genetic algorithm (GA) included in Matlab's Optimization library. The GA depends on the initial conditions and randomization of each generation, therefore, the optimization problem is repeated 2000 times with randomized initial conditions to estimate the global optimum and create a set of possible laminates, which are then selected for a subsequent sensitivity analysis. Notice also that, thanks to the symmetry condition, rotating the plate 180° about the longitudinal axis of the wing produces the same bending properties but coupling properties changed in sign. Thus, the optimization process can be carried out once for the wash-in design and rotate the plate about the symmetry plane to create the wash-out design. The optimization problem is presented in Equation 3.2.

$$\begin{aligned}
 & \underset{x}{\text{minimize}} \quad d_{16} \\
 & \text{subject to} \quad \left| \frac{d_{11}}{d_{11,ref}} - 1 \right| < \varepsilon_{d_{11}} = 0.02 \\
 & \quad \quad \quad |a_{16}| < \varepsilon_{a_{16}} = 10^{-9} \\
 & \quad \quad \quad |a_{26}| < \varepsilon_{a_{26}} = 10^{-9} \\
 & \text{where } x = [\theta_1, \theta_2, \dots, \theta_n] \text{ and } \theta_i = [-75 : 15 : 90] \text{ for } i = 1, 2, \dots, n
 \end{aligned} \tag{3.2}$$

It should be noticed that it is not possible to assess the significance of the bend-twist coupling introduced in the optimization process directly from the terms in the abd matrix, as there is no reference value to which it can be compared. Therefore, the results from the optimization are compared to the compliance terms obtained from a unidirectional laminate (UD), which has a stacking sequence with

all the plies oriented in the same direction, to determine how much of the tailoring potential is lost due to the definition of the optimization problem given by Equation 3.2. In Figure 3.9, both the bend-twist coupling term and the bending compliance term are compared. On the one hand, the results from the optimization are presented with respect to the direction of its principal stiffness axis, which is the direction, θ , in which the maximum bending modulus of elasticity, \bar{D}_{11} , is found. This concept will be presented at the end of this section, where it is used to show the directional properties of the different composite plates. On the other hand, the curve represents the compliance value with respect to the direction of the fibres of the UD composite plate.

As can be seen in Figure 3.9a, the direction of the principal stiffness axis of the optimal results tends to the direction in which the UD laminate presents the highest coupling, between 20° and 40° from the longitudinal axis of the plate. However, the best optimization result gives 30% of the coupling term of the UD laminate, which can be explained by the constraint in the bending compliance term. Since the bending compliance is constrained to the reference value, as can be seen in Figure 3.9b, the coupling term cannot achieve the same magnitude as in the UD laminate. Furthermore, for the results with the main stiffness direction close to 90° , it is possible to achieve coupling terms of higher magnitude than the UD laminate. This is because the UD laminate does not add couplings when the main direction is at 90° , hence a slight change in the stacking sequence introduces couplings but barely change the main stiffness direction.

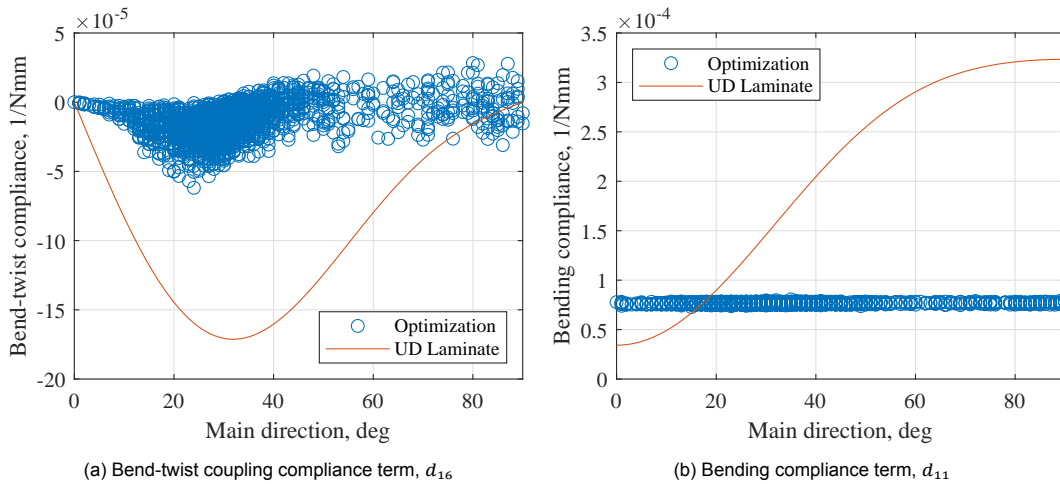


Figure 3.9: Comparison of optimized compliance results to UD plate results

Table 3.2: Stacking sequence of the best results of the optimization problem

Design	Stacking sequence
O1	$[30, 15, 45, 15, 15, -75, 30, -30, 90, 75, -30, -15, 75, -45, -45, -15]_s$
O2	$[30, 45, 15, 0, 60, 90, 75, 30, 0, -15, -60, -75, -30, -15, -60, -15]_s$
O3	$[30, 75, 30, 90, 15, 0, 0, 60, -15, 90, 45, -30, -30, -75, -45, -60]_s$
O4	$[15, 15, -75, 30, 15, -45, 75, 75, 45, -75, -45, -30, -30, 75, -45, 60]_s$
O5	$[30, 90, 45, 15, 30, 15, -45, 15, -15, -45, -15, 15, -30, -30, -30, 60]_s$

In addition, Figure 3.9a shows that the optimization yields several designs of similar performance. Hence, a sensitivity analysis is carried out on the best stacking sequences, presented in Table 3.2, to assess the effect of manufacturing imperfections on the design and select the most robust design. The sensitivity analysis focuses on the variation of the ply angle since ply angle misalignment due to hand layup is considered to be the main manufacturing imperfection. The effects of these misalignments are studied by recomputing the compliance matrix of the best five results of the optimization but including random misalignments in their plies. Each ply, at a nominal angle θ_i , includes a misalignment, γ_i , following a normal distribution such that 95% of the results are within $\pm 5^\circ$, representing the error that can be introduced with the manual lamination. These new laminates are defined by Equation 3.3.

$$[\theta_1 + \gamma_1, \dots, \theta_i + \gamma_i, \dots, \theta_n + \gamma_n]_s \quad \text{for } i = 1, 2, \dots, n \quad (3.3)$$

$$\gamma_i \sim N(\mu = 0^\circ, \sigma = 2.5^\circ)$$

Such a perturbation of the selected laminates is repeated 5000 times to obtain a sensitivity envelope of the selected laminates to such random changes. Then, the objective is to find the plate that keeps the compliance matrix bending component, d_{11} , as similar as possible to the reference plate. This component follows a normal distribution centred on the value of the design without the random deviations, $d_{11,0}$, as shown in Equation 3.4. Thus, the most robust design is the one with the lowest deviation, σ . Finally, the sensitivity envelopes and the summary of these results are presented in Figure 3.10 and Table 3.3 respectively. From these results, the solution O1, which presents the highest coupling, is the most robust design in terms of bending stiffness. This can be seen in Figure 3.10a, which shows that the variations in O1 design produce the lowest spreading in the bending stiffness values. Therefore, the stacking sequence corresponding to O1 is selected for the aeroelastic tailoring study.

$$d_{11} \sim N(\mu = d_{11,0}, \sigma) \quad (3.4)$$

Table 3.3: Results of the sensitivity analysis

Design	d_{11} [1/Nmm]	$\sigma_{d_{11}}$ [%]	d_{16} [1/Nmm]	$\sigma_{d_{16}}$ [%]
O1	$7.64 \cdot 10^{-5}$	2.87	$-6.19 \cdot 10^{-5}$	6.62
O2	$7.75 \cdot 10^{-5}$	3.09	$-5.35 \cdot 10^{-5}$	7.92
O3	$7.67 \cdot 10^{-5}$	3.82	$-5.33 \cdot 10^{-5}$	6.18
O4	$7.54 \cdot 10^{-5}$	4.16	$-5.02 \cdot 10^{-5}$	8.01
O5	$7.68 \cdot 10^{-4}$	3.25	$-4.96 \cdot 10^{-5}$	6.14

Final designs

To conclude this section, the results of the selection process are presented in Table 3.4. Furthermore, Figure 3.11 presents the engineering modulus of elasticity, $\tilde{E}_{11}(\theta)$, and the bending modulus of elasticity, $\tilde{D}_{11}(\theta)$, computed from the abd matrix as presented in Equation 3.5 [27]. This comparison shows the variation in bending stiffness between plates A to C and the variation in directional properties between the tailored plates, B_{WI} and B_{WO} , and the reference plate, B. The properties in the longitudinal axis of the plate, $\theta = 0^\circ$, are presented in Table 3.5.

The modulus plots show the design objectives for each of the plates. Figure 3.11b shows that the wings for the stiffness study have the same quasi-isotropic \tilde{D}_{11} distribution but at different magnitudes because of the difference in thickness, which was the design objective. In addition, Figure 3.11a shows the effects of the $[0,90]_s$ laminates in the mid-plane. On the one hand, wing B presents an isotropic distribution of \tilde{E}_{11} . On the other hand, wings A and C, which include the mentioned laminates to add thickness to the special balanced sequence, are reinforced in the 0° and 90° directions. For the tailored wings, Figure 3.11c shows how \tilde{E}_{11} is the same, as they have the same plies but in a different sequence. However, this difference has an effect on \tilde{D}_{11} . As can be seen in Figure 3.11d, their bending behaviour is completely reversed: while B_{WO} main stiffness direction is at 25° , B_{WI} is at -25° . Finally, the main constrain imposed by the reference bending compliance from wing B can be seen in the 0° direction, where the three wings present the same \tilde{D}_{11} .

$$\tilde{E}_{11}(\theta) = \frac{1}{a_{11}(\theta)} ; \tilde{D}_{11}(\theta) = \frac{1}{d_{11}(\theta)} \quad (3.5)$$

$$a(\theta) = T^T a T ; d(\theta) = T^T d T$$

where:

$$T = \begin{pmatrix} \cos^2(\theta) & \sin^2(\theta) & 2 \cos(\theta) \sin(\theta) \\ \sin^2(\theta) & \cos^2(\theta) & -2 \cos(\theta) \sin(\theta) \\ -\cos(\theta) \sin(\theta) & \cos(\theta) \sin(\theta) & \cos^2(\theta) - \sin^2(\theta) \end{pmatrix} \quad (3.6)$$

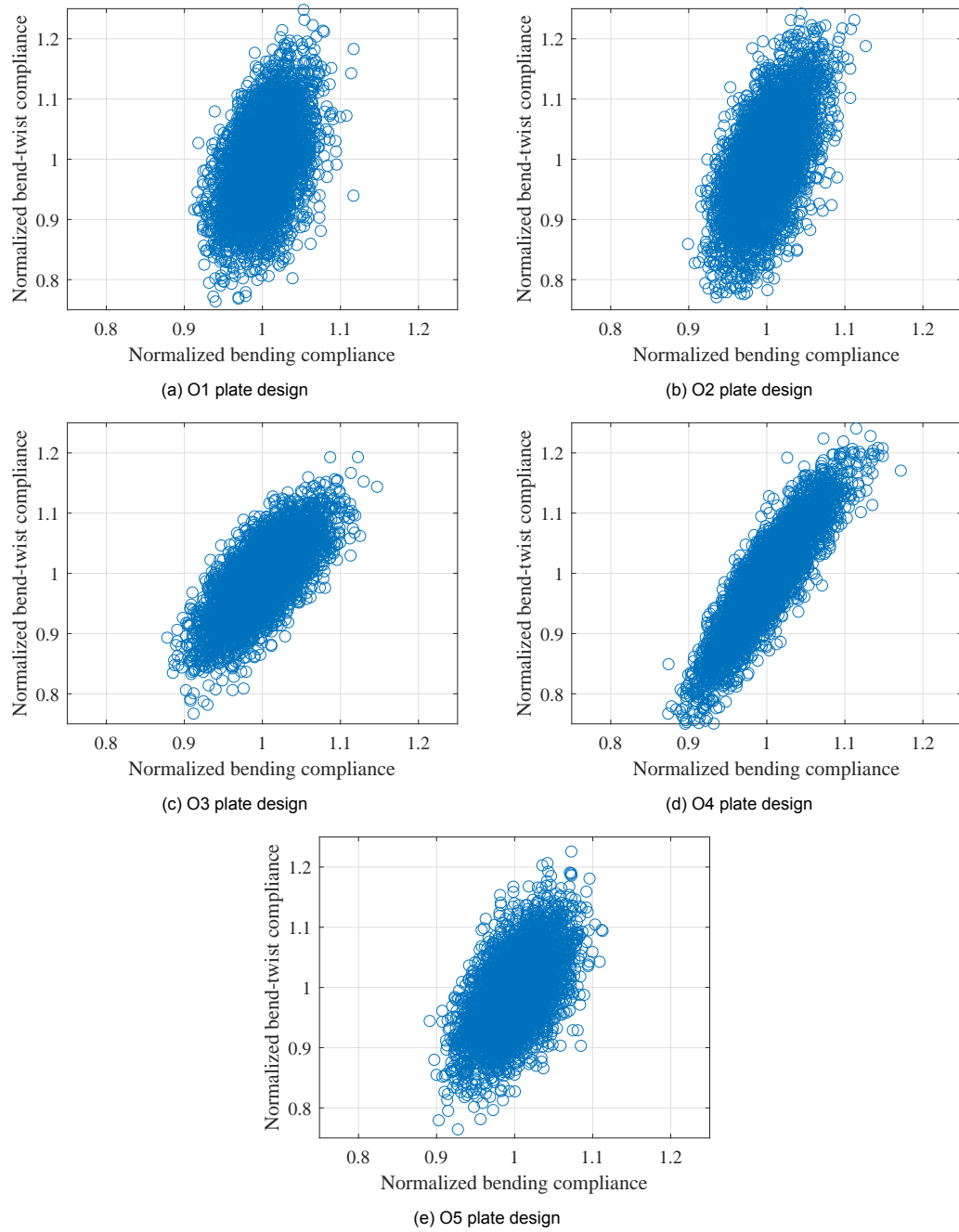


Figure 3.10: Sensitivity analysis comparing the bending compliance, d_{11} , and the bend-twist compliance, d_{16} , normalized with the nominal value.

Table 3.4: Stacking sequence of the wing core plates. Defined using reference system from Figure 3.3.

Plate	Stacking sequence
A	$[0, 45, 90, -45]_s [0, 90, 90, 0]_s [0, -45, 90, 45]_s$
B	$[[0, 45, 90, -45]_2]_s [[0, -45, 90, +45]_2]_s$
C	$[[0, 45, 90, -45]_2]_s [0, 90, 90, 0]_s [[0, -45, 90, +45]_2]_s$
B _{WI}	$[-30, -15, -45, -15, -15, 75, -30, 30, 90, -75, 30, 15, -75, 45, 45, 15]_s$
B _{WO}	$[30, 15, 45, 15, 15, -75, 30, -30, 90, 75, -30, -15, 75, -45, -45, -15]_s$

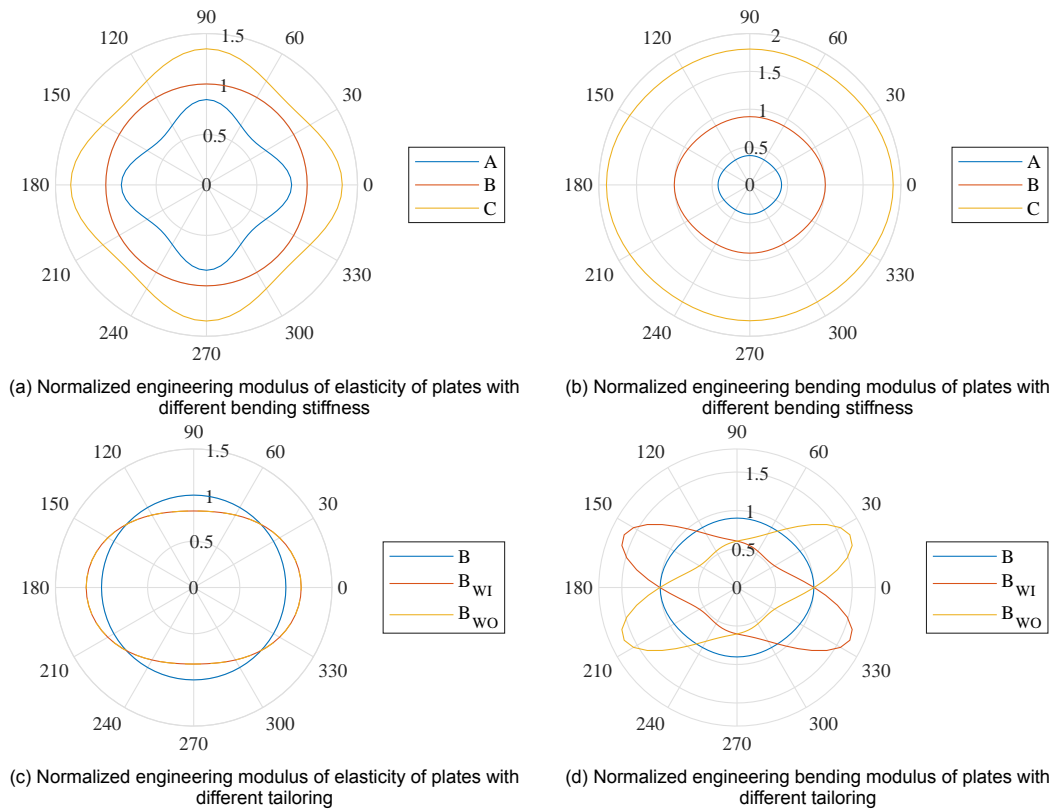


Figure 3.11: Comparison of $\tilde{E}_{11}(\theta)$ and $\tilde{D}_{11}(\theta)$. Parameters normalized with maximum value of reference plate, B.

Table 3.5: Overview of bending compliance and coupling terms of the wing core plates

Plate	d_{11} [1/Nmm]	Thickness [mm]	Coupling	d_{16} [1/Nmm]
A	$1.82 \cdot 10^{-4}$	1.2	-	0
B	$7.67 \cdot 10^{-5}$	1.6	-	0
C	$4.04 \cdot 10^{-5}$	2.0	-	0
B _{WI}	$7.64 \cdot 10^{-5}$	1.6	Wash-in	$6.19 \cdot 10^{-5}$
B _{WO}	$7.64 \cdot 10^{-5}$	1.6	Wash-out	$-6.19 \cdot 10^{-5}$

3.2.3. Numerical simulations

The numerical simulations used for the sizing of the wings are presented in this section. As mentioned before, these simulations are conducted iteratively and are required to check the design constraints, such as the maximum allowable deflection, and provide an estimation of the loads and deflections to be expected during the experiment. For the sake of clarity, subsection 3.2.2 only presented the selection procedure and the final designs. The results obtained for each of these designs are addressed in this subsection.

Modal analysis

Modal analysis is important to understand the dynamic behaviour of the wing and, in the flutter analysis, to see what mode is driving the instability. In Nastran, the normal modes of the wing are computed using SOL 103 or as the first step of the flutter analysis of SOL 145.

The natural frequencies of each of the wings obtained using SOL 103 are presented in Table 3.6. On the one hand, the increasing bending stiffness from wing A to wing C is clearly reflected also in the increasing natural frequencies. Furthermore, the tailoring seems to increase the natural frequencies with respect to reference wing B. This is independent of the wash-in or wash-out tailoring, as both wings

B_{WI} and B_{WO} present higher natural frequencies than wing B. On the other hand, when the hinge is free, the trends of the first flapping mode are different from those of the second flapping mode. The second mode follows the same trends as for the locked-hinge condition while the first one does not seem to be affected by the structural properties of the wings.

The reason for this behaviour change can be found in the shapes of these modes, which are presented in Figure 3.12. It can be seen how both modes in the locked-hinge condition are bending modes affecting the whole wing. However, the first mode in the free-hinge condition is a mode dominated by the folding of the wingtip, referred to as a flapping mode. Since this mode is dominated by the motion of the FFWT, whose properties do not differ between wings, the first flapping natural frequency is barely affected by the main wing design. In addition, the second flapping mode is a combination of wing bending and FFWT folding, hence it is also affected by the main wing stiffness properties.

Finally, the first torsion mode in both free and locked hinge configurations show similar trends as the bending modes: the natural frequency increases when increasing the stiffness. On the other hand, the wash-in tailoring decreases the frequency with respect to wing B while the wash-out increases the frequency. In addition, the comparison of the hinge conditions shows that the locked hinge achieves higher natural frequencies than the free hinge. To conclude, the mode shape of the free hinge configuration shows that this mode is not a pure torsion mode but a combination of torsion and wingtip flapping. In addition, both Figure 3.12e and Figure 3.12f show a local deformation of the skin near the trailing edge, which origin is not clear. However, given that the loads are mainly carried by the plate and the 3D printed part, the impact of the skin on the simulation is limited.

Table 3.6: Comparison between wings of natural frequencies of first modes of free hinge (flapping) and locked hinge (locked) conditions (SOL 103/SOL 145).

Mode	A	B	C	B_{WI}	B_{WO}
Locked - 1st Bending [Hz]	3.28	3.55	3.87	3.62	3.58
Locked - 2nd Bending [Hz]	18.17	18.87	19.55	18.96	19.01
Locked - 1st Torsion [Hz]	32.60	36.31	40.96	35.98	36.43
Free - 1st Flapping [Hz]	1.40	1.41	1.42	1.41	1.41
Free - 2nd Flapping [Hz]	4.82	5.13	5.55	5.25	5.17
Free - 1st Torsion [Hz]	29.75	32.24	35.04	31.66	33.60

Stability analysis: flutter

The wind tunnel experiment is limited to the speeds at which the wings are stable, hence it is important to assess the limits of the wing. For this reason, a flutter analysis is carried out using SOL 145 and the pk-method, which relies on modal analysis to assess the aeroelastic stability of the model.

The results of the flutter analysis are summarized in Table 3.7. The bending stiffness of the wings increases the limiting speeds, as can be seen from the results of wings A, B, and C. In addition, this dependency on bending stiffness is more important when the hinge is locked. In the free-hinge condition, the flutter speed experiences a significant drop with respect to the locked-hinge condition. For a better understanding of this phenomenon, the sensitivity of the flutter speed with respect to the changes in the hinge stiffness is investigated, as shown in Figure 3.13. By gradually increasing the hinge stiffness from 0 to the stiffness in the locked-hinge condition, it is possible to see that a clear jump in flutter speed occurs between hinge stiffness of 20 Nmm/rad and 40 Nmm/rad. To explain the reason for this jump, Figure 3.14 presents the damping ratio and frequency diagrams for the cases of hinge stiffness of 20 Nmm/rad and 40 Nmm/rad, which are close to the sudden variation of flutter speed previously mentioned. It can be seen how, for lower stiffness, the flutter mechanism is the interaction between the first and second modes leading to an instability of the second mode. On the other hand, for the increased hinge stiffness, flutter appears in the fourth mode as a result of an interaction with the third mode. Therefore, the speed drop between conditions is caused by a change in the flutter mechanism that drives the instability.

Finally, the flutter analysis also shows interesting behaviour with respect to the wing tailoring and hinge-free and hinge-locked condition. Considering the reference studies on aeroelastic tailoring presented by Weisshaar [47], it is expected that the wash-in tailoring delays flutter and promotes diver-

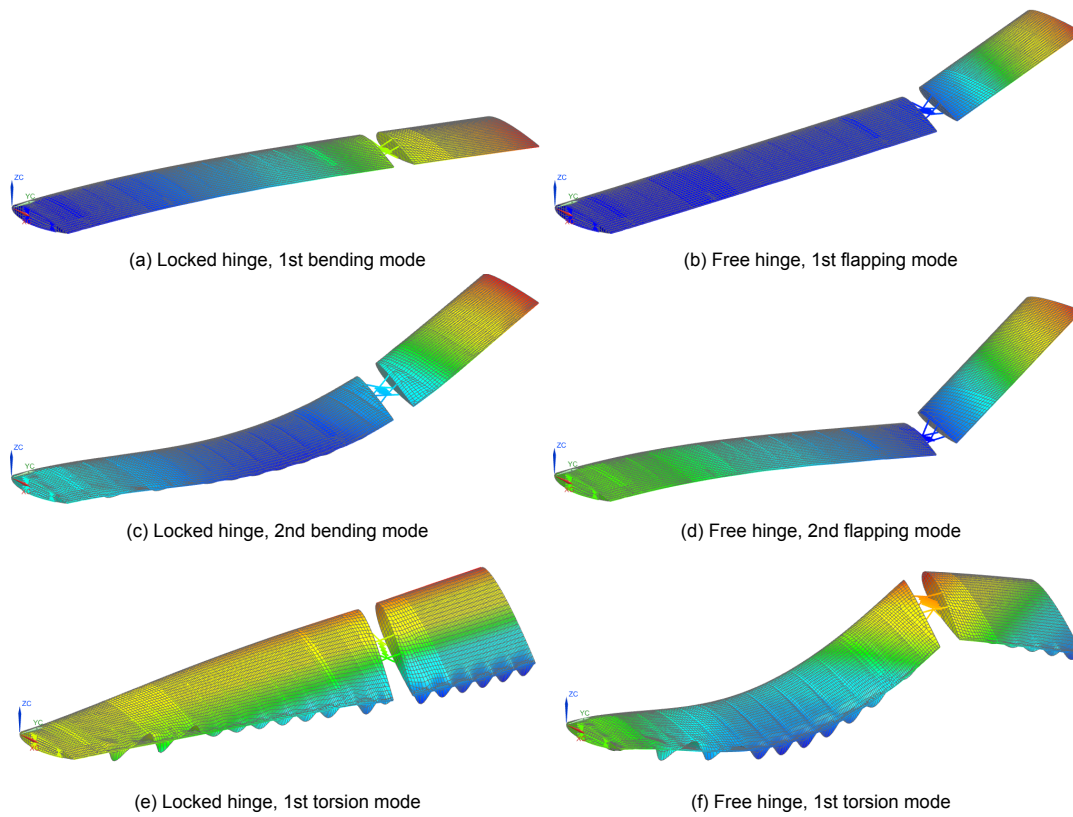


Figure 3.12: Natural modes shapes from simulation (SOL 103/SOL 145).

Table 3.7: Instability speed comparison between wings in free-hinge and locked-hinge conditions (SOL 145).

Wing	A	B	C	B _{WI}	B _{WO}
Free hinge [m/s]	19.9	21.1	23.0	20.4	22.9
Locked hinge [m/s]	67.5	81.4	93.0	56.0	81.3

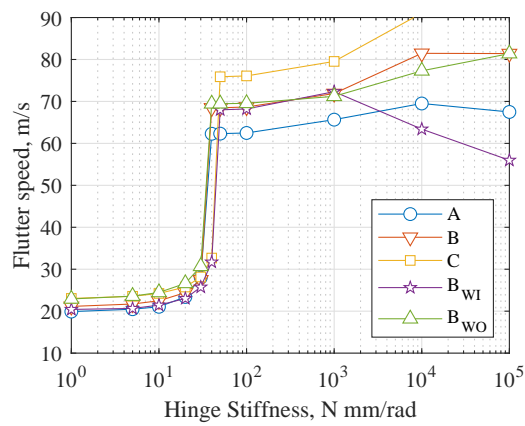


Figure 3.13: Sensitivity analysis of flutter speed to hinge stiffness for the different wings.

gence while the wash-out tailoring has an opposite effect. To explain the behaviour in the locked-hinge condition, which would correspond to a conventional wing, Figure 3.15 presents a comparison of the damping and frequency flutter plots of wings B, B_{WI} and B_{WO}. For wing B_{WI}, there is a sudden drop in damping and frequency of the first mode, leading to a divergence instability. In contrast, the limiting aeroelastic instability for wings B and B_{WO} is flutter. Nevertheless, when comparing the flutter speed of the tailored wings, the flutter speed of the B_{WI} is higher than the flutter speed of the B_{WO}. These

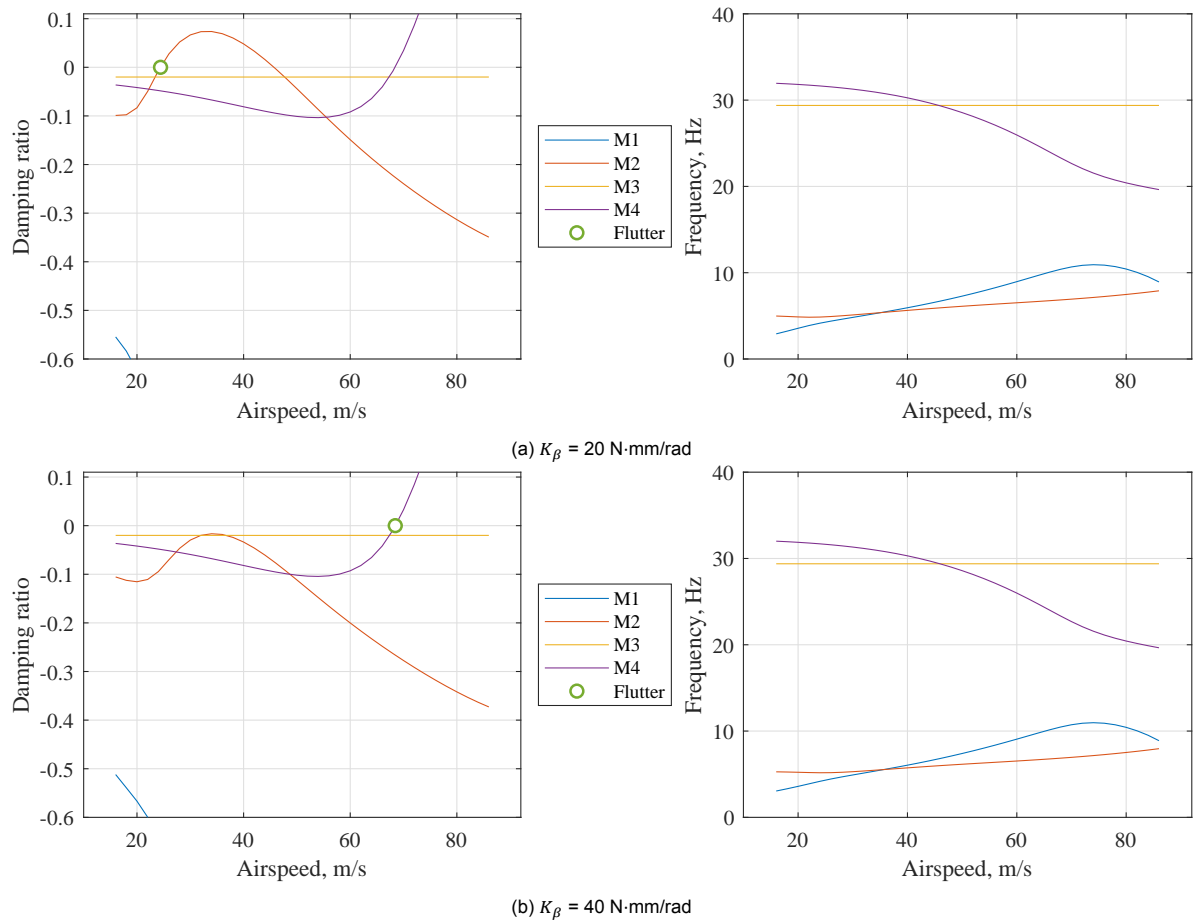


Figure 3.14: Comparison of damping ratio and frequency flutter plots of Wing B at different hinge stiffnesses, K_β .

observations are in agreement with the expectations [47] as wash-in tailoring promotes divergence and delays flutter, while wash-out tailoring promotes flutter and delays divergence.

On the other hand, in the free-hinge condition, in all the wings, the limiting instability is flutter. However, in this case, the flutter speed of the B_{WI} is lower than that of the B_{WO} , which is contrary to the expectations [47]. This finding could be explained by the change in the flutter mechanism seen in the sensitivity analysis, hence the design rules applied for conventional aircraft wings might not be applicable for the FFWT.

To conclude the flutter analysis, the sensitivity of the instabilities to the hinge stiffness and the change in the flutter mechanism show the complexity of the structural response of the hinge, and the drop in flutter speeds presents a possible limitation of the FFWT. Keeping this in mind, the experiment is designed at an airspeed of 15 m/s to avoid unexpected instabilities, corresponding to a Reynolds number of $Re = 100000$.

Loads and deflections

Last, static aeroelastic simulations using SOL 144 are used to estimate the steady-state loads and deflections of the wing. These simulations include gravity and study the wing at $\alpha = 0^\circ$ and $\alpha = 8^\circ$. On the one hand, since the airfoil used is symmetric and given that the aerodynamic mesh does not adapt to the structural deformations, the first condition is equivalent to a static simulation in which the model is only loaded with gravity. On the other hand, the $\alpha = 8^\circ$ condition introduces an aerodynamic load to compare it with the magnitude of the weight and study which force is dominant. To make it as similar as possible to the real flight conditions, it is desired to have a system that is dominated by the aerodynamic force, so the 3D printed part is optimized to reduce its weight using these simulations as reference.

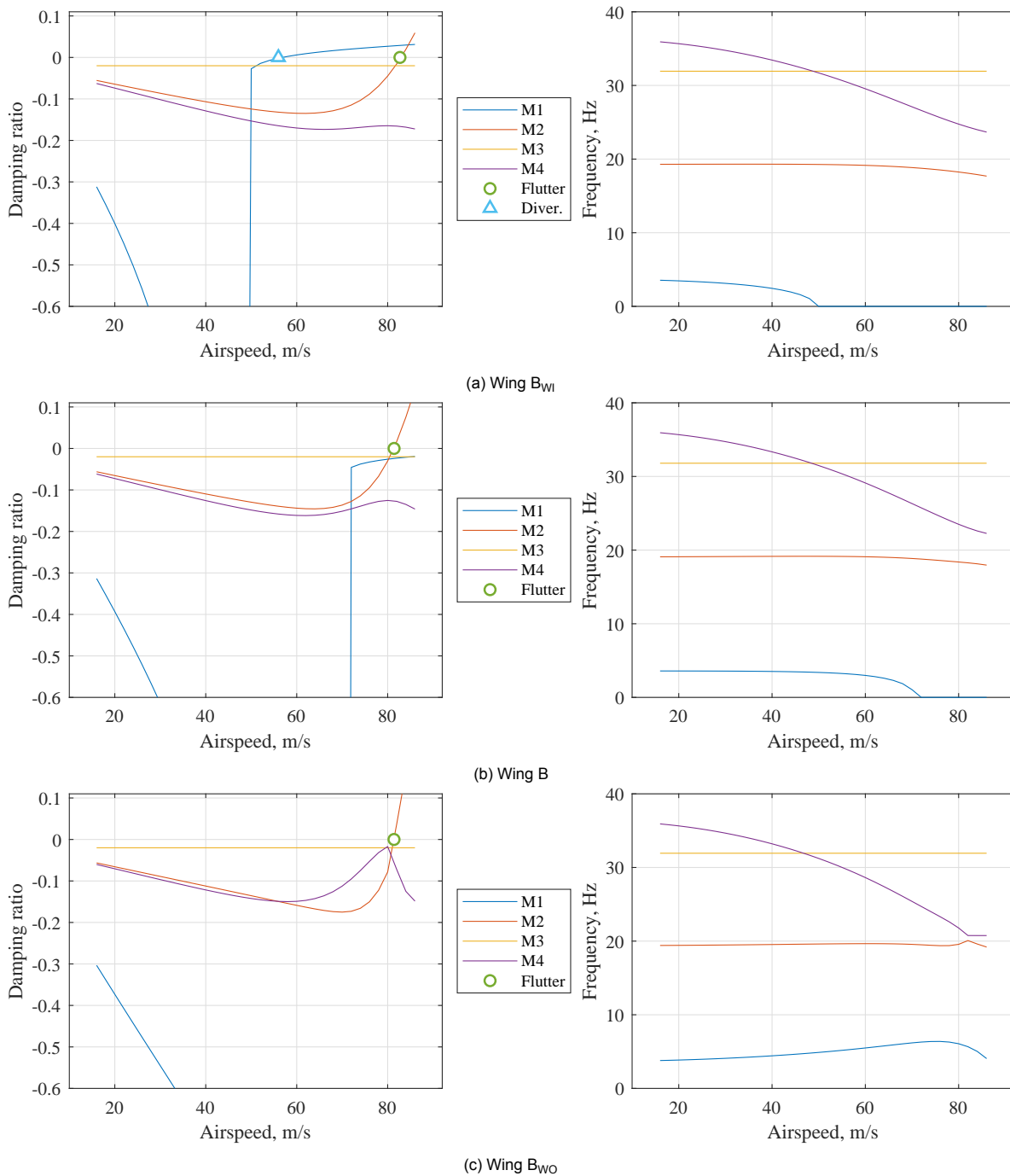


Figure 3.15: Comparison of damping ratio and frequency flutter plots between wings B, B_{WI} and B_{WO} in locked hinge condition.

Finally, the gust response is studied with SOL 146. As explained by Cheung et al. [20], it cannot be used to solve gusts hitting the wing at a given static condition, i.e. $\alpha \neq 0^\circ$, so the problem is solved as a superposition of the static condition and the gust. First, the mesh is pre-deformed according to the results of the static analysis, and, afterwards, the gust is simulated. The final result is then the sum of both. Notice that, given the linearity of the model, the validity of the results is limited to low fold angles, β . For this reason, the locked hinge condition is considered as an indicator of the maximum load and deflections but the free hinge condition is only considered qualitatively to understand its effects. The hinge release based on a load threshold cannot be simulated with the available tools, hence it is not considered.

These results are used to ensure the wing will remain in the wind tunnel section during the experiment, as can be seen in Table 3.8. Notice that the deflection when the hinge is free is close to the maximum deflection of 20 cm previously mentioned and does not consider the added deflection caused by the gust. Therefore, one may think that this deflection might move the wing out of the test section. However, two considerations have been taken into account to accept these results: on the one hand, the model does not take into account the geometrical nonlinearities hence the real loads and deflections will be lower than the ones computed in the simulation; on the other hand, given the discrete nature of the gust and the damping of the response, the magnitude of the maximum upwards deflection will be higher than that of the maximum downwards deflection, as can be seen in Figure 3.16b. Therefore, the non-symmetric response will allow moving the wing to a position below the centre line of the test section, hence increasing the allowed positive deflection. In addition, the dynamic simulations are used to ensure that the different designs and test cases offer a noticeable difference in their response. This can be seen in Figure 3.16, which shows an example of comparison between the locked and free hinge conditions for two different gusts, and Figure 3.17, which shows a comparison of peak loads between wings at different gust frequencies.

Table 3.8: Maximum vertical displacements from static simulations (SOL 144).

Wing	Free ($\alpha = 8^\circ$) [mm]	Locked ($\alpha = 0^\circ$) [mm]	Locked ($\alpha = 8^\circ$) [mm]
A	175	-37	8
B	173	-31	6
C	172	-25	5
B _{WI}	174	-30	7
B _{WO}	173	-30	5

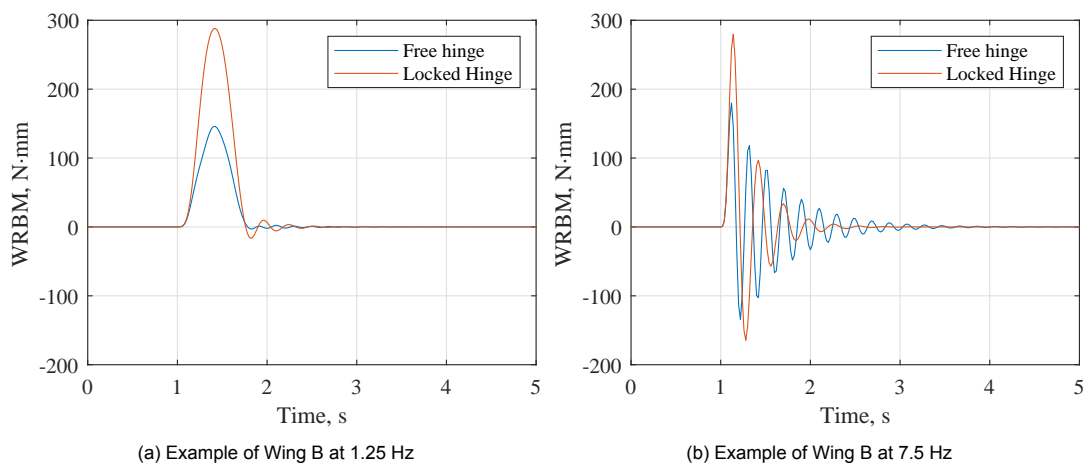


Figure 3.16: Results of gust simulations (SOL 146). Comparison between locked-hinge and free-hinge conditions for different gust frequencies.

From the individual gust responses from Figure 3.16, it is possible to see that the peak loads for different gust frequencies are similar but the time response is not. On the one hand, for the slow gust of 1.25 Hz, the loads smoothly follow the gust but, as expected, the loads are higher when the hinge is locked. In addition, the load presents a small oscillation after the gust when the hinge is locked, which does not occur when it is free. On the other hand, for the fast gust of 7.5 Hz, the load alleviation is similar to the slower gust but there is a clear difference between the free-hinge and the locked-hinge conditions. While the oscillations disappear after a second for the locked hinge condition, the oscillations persist for twice the time in the free-hinge condition. This behaviour is similar for all the wings, hence only these examples are presented.

Finally, in the peak load comparison from Figure 3.17, there is a clear difference between the magnitudes each wing can achieve. The peak loads decrease with the bending stiffness of the wings, hence wing A presents higher peak loads than wing B and wing B presents higher peak loads than wing C. Furthermore, the tailoring also has a prominent effect: wing B_{WO} presents the lowest peak loads, even

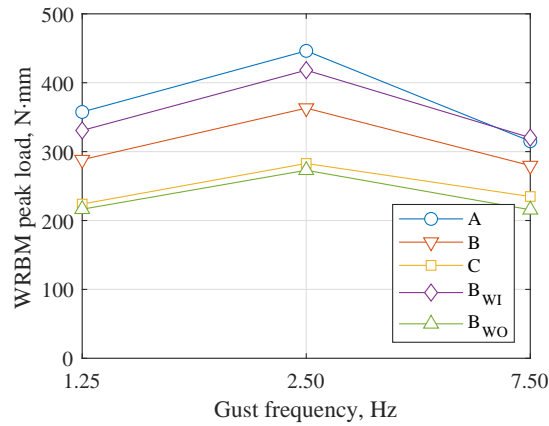


Figure 3.17: Peak WRBM load comparison between plates for different gust frequencies in locked-hinge condition (SOL 146).

lower than wing C, while B_{WI} shows higher peak loads than the reference wing B, comparable to those from wing A.

3.3. Hinge mechanism design

The last parameter to be varied during the experiment is the hinge release threshold. Hence, a mechanism to lock and release the FFWT is required. In this chapter, the requirements for the mechanism and the design procedure are presented.

3.3.1. Requirements

The objective of the mechanism is to release the wingtip at different instants of the gust response (i.e. load thresholds). Therefore, the operational requirements are:

- The release time or load threshold must be controlled.
- The reaction time must be short in comparison to the gust period to be able to react within the gust.
- The release instant must be consistent between samples within a test case to allow for statistical evaluation of the results.

In addition, it is also important to consider the dimensional limitations, as the model has a 100 mm chord and 18 mm maximum thickness.

3.3.2. Design procedure

The design procedure starts with an estimation of the loads that the mechanism would have to resist to keep the wingtip locked. Therefore, the model presented in Figure 3.18 is used as a simplification of the problem. The aerodynamic load is assumed to be uniform and the weight is not considered in the total moment as a conservative estimation, since the weight would reduce the moment at the hinge. Furthermore, the lift distributed force, l , is estimated using thin airfoil theory, hence Equation 3.7 is used to compute the section lift coefficient, C_l . Then, Equation 3.9 defines the estimation of the bending moment at the hinge, where q is the dynamic pressure, U_∞ is the freestream velocity, ρ is the air density, f is the wingtip length and c is the airfoil chord.

$$C_l = 2\pi\alpha \quad (3.7)$$

$$l = \frac{1}{2}\rho U_\infty^2 c C_l = qcC_l \quad (3.8)$$

$$M_h = \int_0^f l x dx = qcC_l \frac{f^2}{2} \quad (3.9)$$

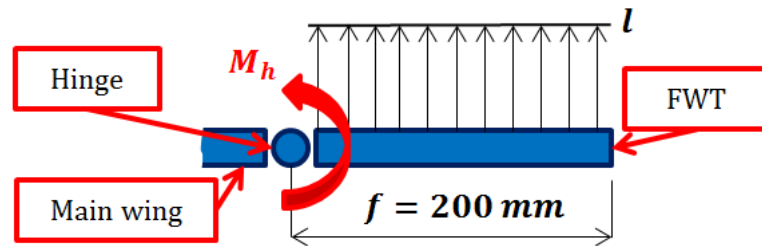


Figure 3.18: Load diagram for hinge moment estimation

For a freestream velocity of 15 m/s and an angle of attack of 13° , used as a combination of the 8° angle of attack used for the static simulations and the 5° from the gust, the hinge moment required to keep the wingtip locked is 390 Nmm.

The first considered design is a bistable mechanism similar to the one assessed by Castrichini et al. [16], presented in Figure 3.19. This type of mechanism has two stable positions and, to switch between both, it is necessary to apply a certain load. Considering the FFWT, this type of mechanism would have one stable position in which the wingtip would be locked, and a second position with the FFWT free to rotate. This passive release design is interesting because of its simplicity, but designing it to change the release threshold adds a lot of complexity to the wing design. It would be possible to change the threshold by changing the geometry of the mechanism, i.e. the angles and position of the springs in Figure 3.19, but that would require access to the locking system. With the chosen model design, accessing the mechanism would require cutting the shrinking foil for every threshold iteration, hence slowing down the testing process. In addition, the oscillatory nature of the problem would limit the use of the mechanism. In Figure 3.20, a load signal example with two hypothetical thresholds is presented. In this case, the position would change after achieving the top threshold but, when achieving negative loads due to the oscillation, the mechanism would recover the locked condition. Therefore, the functionality of the mechanism would be limited by the load thresholds.

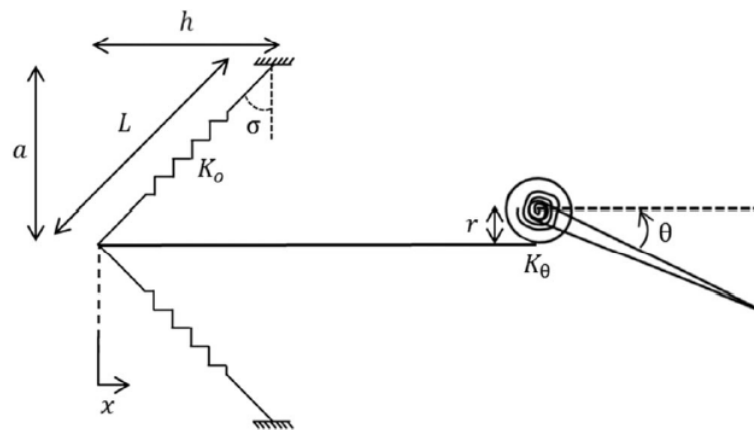


Figure 3.19: Example of bi-stable mechanism used to lock the hinge. Retrieved from [16].

Next, the second iteration of the design process tries to avoid this limitation by replacing the spring system with an electromagnet, as shown in Figure 3.21. This mechanism could be realised by connecting the hinge to a metallic part that would be attracted by the electromagnet, hence avoiding the movement of the wingtip. If the load applied at the wingtip was high enough to separate the metallic part from the magnet, the mechanism would be released, allowing free rotation of the wingtip. Furthermore, the force created by the electromagnet depends on the input current, hence it would be possible to control the load threshold without accessing the mechanism to modify its configuration. Nevertheless, this concept is mainly limited by the dimensions of the wing: an electromagnet capable of locking the hinge would not fit within the airfoil shape.

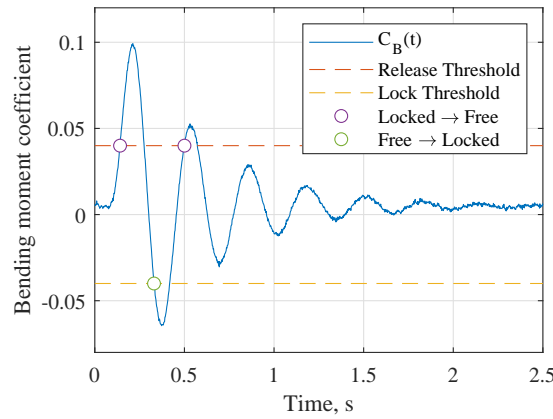


Figure 3.20: Bending moment coefficient time signal example to illustrate the changes in hinge condition when using a bistable mechanism.

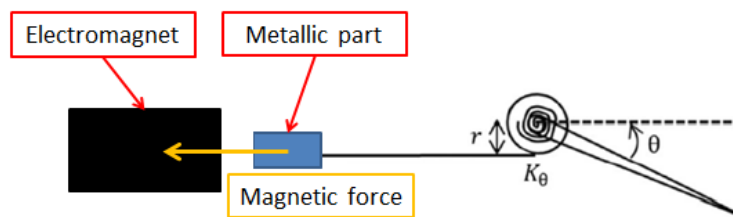


Figure 3.21: Sketch of the locking mechanism introducing an electromagnet to replace the springs of the bi-stable mechanism.

Finally, an active solution is considered: the mechanism would be connected to a microcontroller to release the FFWT based on a load measurement from the sensors. This solution allows a simplification of the mechanism but introduces the necessity of using real-time load measurements and control, addressed in chapter 4, to release the hinge at the desired instant. For this selection, different locking mechanisms are considered taking into account their size, weight, reaction time and the possibility to implement them using standard parts [43]. An overview of the different considered options is presented in Table 3.9, which presents a comparison of the characteristics of each type of mechanism.

In this table, the three most promising options are compared: a latch, an electromagnet and a friction-based lock. First, due to the dimensions of the wing model, the size and weight of the mechanism are the most limiting properties. As already mentioned, an electromagnet that fits in the wing and is capable of locking the wingtip is not available, hence the electromagnet cannot be used. On the other hand, both the latch and the friction-based mechanism are suitable options. In general, the latch outperforms the friction-based mechanism but presents an important drawback: unlocking the mechanism when a load is applied would not be possible, since a shear load might lock the movement of the latch and prevent its release.

Table 3.9: Overview of hinge mechanism characteristics, where '+' means that the property is satisfied as desired, '0' indicates the property is satisfied but could be improved and '-' means the property is not satisfied.

Type	Size	Weight	Reaction time	Power consumption	Unlocking under load	Availability
Latch	+	+	+	+	-	+
Electromagnet	-	-	0	-	+	-
Friction	0	0	+	+	+	0

Therefore, the selected solution is a friction-based mechanism, consisting of a pin that would be pressed against the shaft, creating a friction force to lock the hinge, as presented in Figure 3.22. Nevertheless, since the radius of the shaft is limited due to the dimensions of the wing, the required force to compensate the moment at the hinge would be too high. For this reason, the distance from the hinge axis to the contact point is increased by adding an aluminium part following the shape of the 3D printed part. Therefore, as presented in Equation 3.10, the moment arm, r , is increased and the friction force,

F_f , required to compensate the hinge moment, M_h , is reduced. Last, the linear force, F_l required to produce this friction force can be computed with Equation 3.11, where μ_f is the friction coefficient. For the contact between two aluminium parts [2], the required linear force would be 35 N.

$$M_h = rF_f \quad (3.10)$$

$$F_r = \mu_f F_l \quad (3.11)$$

To conclude with the definition of the hinge mechanism and as the final step before manufacturing all the wings, a prototype version of the wingtip has been manufactured to test that the mechanism is capable of locking the wingtip as desired.

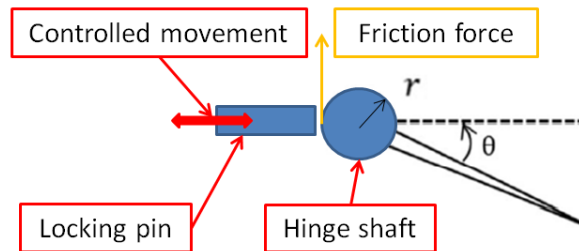


Figure 3.22: Sketch of the friction-based locking mechanism. The pin is pressed against the hinge shaft to create friction and lock the rotation of the wingtip.

3.3.3. Hinge prototype and final design

The prototype used for testing the mechanism is presented in Figure 3.23, which consists of the wingtip and the tip of the main wing. This reduced model allows testing the mechanism without printing the complete wing while still being able to check that the locking principle works and detect possible design deficiencies, such as the dimensions of the holes for cables or the printing tolerances. After the first test, it has been found that the friction-based mechanism is not capable of locking the hinge. The estimations of the force did not take into account possible manufacturing imperfections in the contact surfaces, hence the friction is not as high as required. Therefore, a modification is applied to these surfaces to make the locking possible.

The final mechanism is designed to block the wingtip rotation by creating an interference between the main wing and the FFWT, as can be seen in the realization of the mechanism shown in Figure 3.24. The locking pin is pressed against the hinge axle of the wingtip using an eccentric lever connected to a Blue Bird BMS-A10H rotary actuator³, which is controlled by an Arduino microcontroller⁴ that releases the hinge at the desired instant. By adding a spring and a chamfer at the end of the pin, the system is designed in such a way that the FFWT can start moving as soon as the pressure on the locking pin is released. This way, even if the pin has not moved to the end of its stroke, the FFWT can already rotate freely. In addition, as a result of the axial alignment of the reaction force of the pin and the eccentric lever, the actuator does not have to actively resist the reaction load on the locking pin.

³“BMS-A10H,” Blue Bird Model, 2021. URL https://www.blue-bird-model.com/products_detail/73.htm, retrieved 28 July 2021.

⁴“Arduino Boards and Modules,” Arduino, 2021. URL <https://store.arduino.cc/collections/boards>, retrieved 25 May 2021.

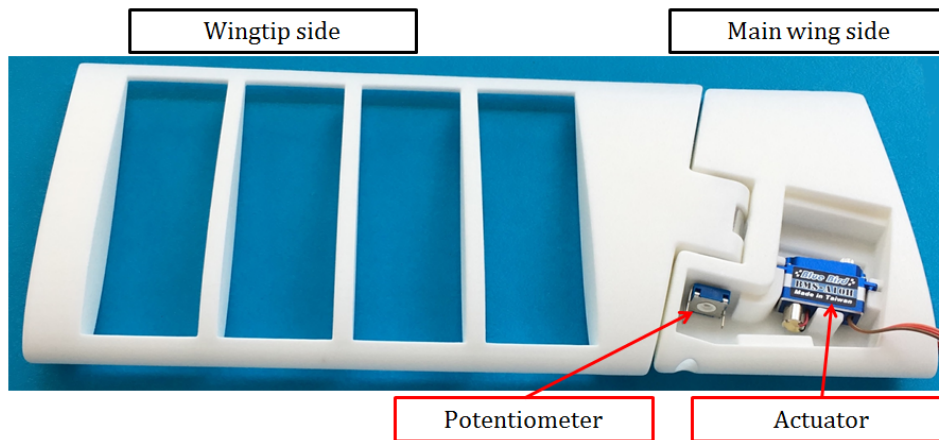


Figure 3.23: Reduced model prototype used for testing the hinge mechanism

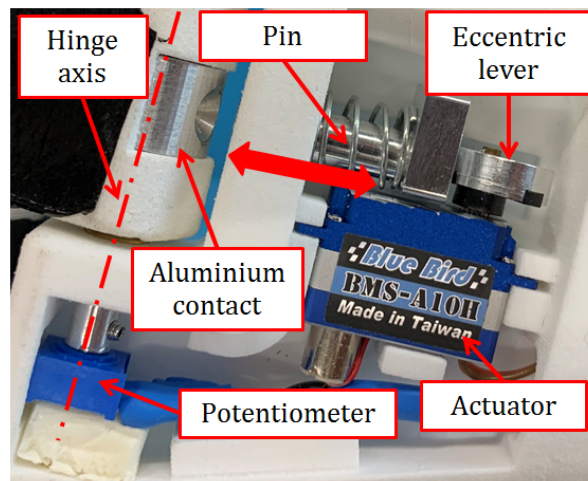
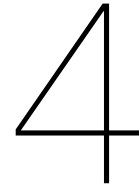


Figure 3.24: Detail of the hinge mechanism in free-hinge condition



Experimental Setup and Procedures

This chapter addresses the experimental setup and definition of the test conditions. In section 4.1, the model used and how it is manufactured is described. Next, the data acquisition system and the processing applied to the measurements are described in section 4.2 and section 4.3 respectively. Then, the wind tunnel facilities and the final setup is presented in section 4.4. Finally, the different parts of the experiment are described in section 4.5.

4.1. Wing model

The wing model used for the experiment is the one presented in chapter 3, which has been manufactured in the Delft Aerospace Structures and Materials Laboratory (DASML) at the TU Delft. The final result can be seen in Figure 4.5, which shows one of the wings before the skin is assembled. Finally, the different parts of the assembly can be divided into two groups: structural elements (orange) and sensors (red).

4.1.1. Structural elements

The structural elements of the wing are considered those that carry the loads and give the aerodynamic shape of the wing. In addition, those parts used to actuate the hinge are also considered in this section, i.e. the hinge mechanism. The main structural elements of the wing are:

- **3D printed parts:** The 3D printed parts are printed in nylon PA12¹ using Selective Laser Sintering (SLS) technology, which allows printing complex geometries without the need of supports. The 3D printed elements are:
 - Main wing: printed as a single part with a round base used to fix the model to the test setup. This part includes two compartments at the tip to house the sensors and the hinge release mechanism.
 - Covers for the sensor compartments: used to keep the shape of the airfoil at the tip of the main wing.
 - Folding wingtip: printed as a single part with important weight reduction modifications such as holes in the ribs and designed to fit the metallic parts of the hinge mechanism. In addition, before closing the assembly with the skin, foam pieces are added between ribs to give a better aerodynamic shape without an important increase in weight.
- **Core plate:** main load-bearing element manufactured with the 0.05 mm thickness NTPT TP135

¹PA2200 Product Information. EOS GmbH, 2001. URL https://cdn2.hubspot.net/hubfs/5154612/Material%20documentation/Nylon%20PA12/PA2200_Product_information_03-10_en.pdf. Last accessed: 28 July 2021

carbon fibre prepreg², which allows precise control of the tailoring.

- **Skin:** manufactured using shrinking Oralight foil³. It is applied on top of the 3D printed parts and then heated to shrink and adapt to the 3D printed chassis. Due to this shrinking, the skin does not follow the airfoil shape along the wingspan but bends inwards between ribs, as can be seen in Figure 4.1. Consequently, the edges of the 3D printed part can cause boundary layer tripping, which could affect the final results of the experiments. To minimize this effect, the foam parts are used in the FFWT and the covers in the main wing.
- **Release mechanism:** aluminium mechanism presented in section 3.3, which is designed and machined considering the tolerances of the 3D printing, ensuring a proper locking of the rotational movement of the FFWT.

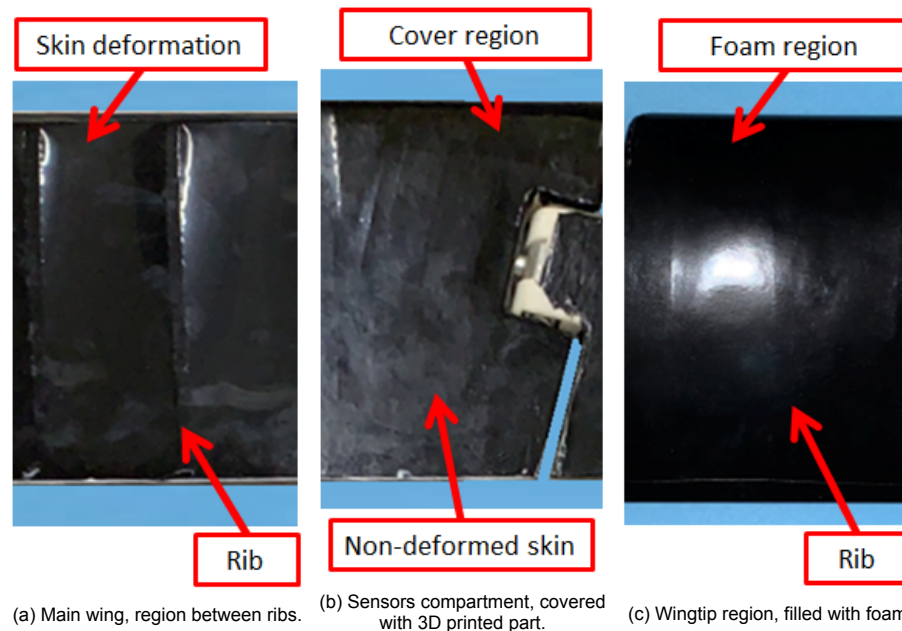


Figure 4.1: Details of skin deformation at the different regions of the wing.

4.1.2. Sensors

The measurements carried out in the wind tunnel investigation are done using three types of sensors. First, two Kyowa KFGS-10-120-D17-16⁴ triaxial 0°/90°/45° strain gauge rosettes are used on the top and bottom faces of the plates to measure the strains at the root of the wing, which can be related to the WRBM. The central strain gauge, 45°, is positioned in the spanwise direction, leaving the 0° and 90° strain gauges at $\pm 45^\circ$ from the spanwise direction of the wing, as shown in Figure 4.2. Each of the top strain gauges is connected to the corresponding parallel strain gauge from the bottom rosette in half-bridge configuration for an improved signal-to-noise ratio with respect to a quarter bridge configuration. For example, the strain gauge from the top rosette at 45° is connected to the strain gauge from the bottom rosette at -45°, as the rosette is turned by 180° around the spanwise direction, as represented in Figure 4.3.

For a better understanding of the position of the strain gauge rosettes, Figure 4.4 presents the expected strains for pure bending and pure torque loads. For pure torque, M_S , the central strain gauges

²TP135 Data Sheet. North Thin Ply Technology, 2019. URL https://www.thinplytechnology.com/assets/mesimages/NTPPTDS-TP135_V1-6.pdf. Last accessed: 28 July 2021.

³Oralight. Lanitz-Prena Folien Factory GmbH, 2021. URL https://www.oracover.de/katalog/artikelinfo/4209/oralight-lightiron-on-film---width_60-cm---length_2-m. Last accessed: 28 July 2021.

⁴KFGS Series, General-purpose Foil Strain Gages. KYOWA, 2021. URL https://www.kyowa-ei.com/eng/product/category/strain_gages/kfgs/index.html. Last accessed: 28 July 2021.

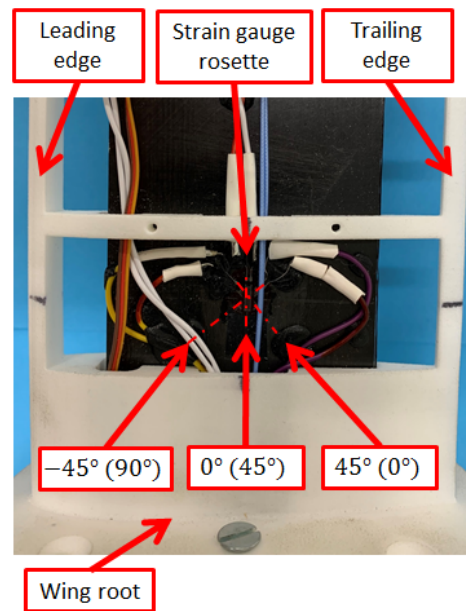


Figure 4.2: Detail of the strain gauge rosette. The directions with respect to the spanwise direction are annotated while their original direction, as named by the manufacturer, is presented between parentheses.

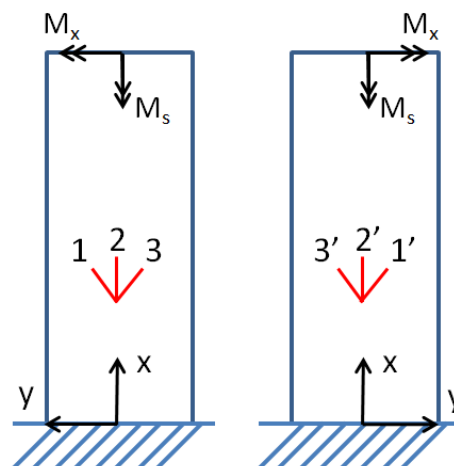


Figure 4.3: Detail of the electrical connections between strain gauges. Each number represents a connection, giving the number to the strain gauge at the top face of the plate and the number with the apostrophe to the strain gauge at the bottom face of the plate.

do not show any strain due to their alignment with the moment direction. Therefore, this type of load only affects the $\pm 45^\circ$ strain gauges, giving strains of different signs between the 45° direction and the -45° . On the other hand, a pure bending load, M_x , affects all of the strain gauges, producing compressive strains on one side of the plate and tensional strains on the other. Notice also that, since the $\pm 45^\circ$ strain gauges are not aligned with the spanwise direction, the magnitude of the strains is lower than the central strain gauge.

Secondly, two PCB 352A24 uniaxial accelerometers⁵ are used to characterize the main wing tip displacement. However, the acceleration signals were affected by the vibrations caused by the hinge release mechanism, hence the noise produced by these vibrations made it impossible to use the measurements from the accelerometers during the gust responses. Therefore, the accelerometers can only be used for the modal analysis. In addition, these sensors can operate between 1Hz and 8000Hz but,

⁵PCB 352A24 Uniaxial Accelerometer. PCB Piezotronics, 2021. URL <https://www.pcb.com/products?model=352A24>. Last accessed: 28 July 2021.

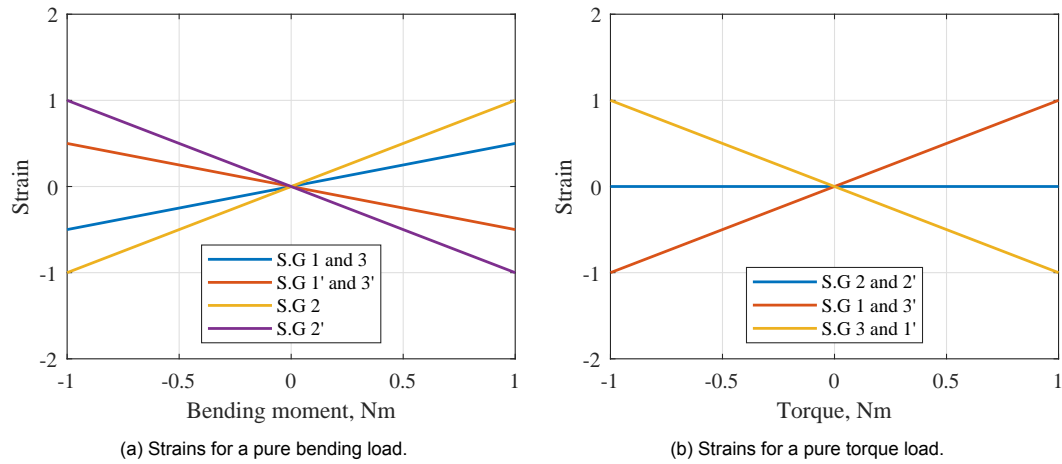


Figure 4.4: Strains on the different strain gauges for pure bending and pure torque loads.

during the experiment, it was found that they cannot reliably detect frequencies below 1.5 Hz, which would compromise the accuracy of the measurements taken for the slowest gusts at 0.5 Hz and 1.5 Hz.

Finally, the fold angle of the wingtip is measured with a Bourns 3310C-125-203L potentiometer⁶ connected to the shaft of the FFWT. This measurement is used to study the reaction time of the system and, since the accelerometers are limited in the low-frequency range, the potentiometer is also used in the modal analysis, addressed in subsection 4.5.2, to detect natural frequencies below 1.5 Hz.

To conclude, two main practical considerations were taken into account when cabling the sensors and connecting them to the data acquisition system:

- The cables were fixed to the wing using a combination of tacky tape and masking tape to provide strain relief and avoid damaging the sensors when manipulating the wings. On the one hand, the tacky tape was only used at the root, reducing the impact of the added weight on the bending load. On the other hand, the masking tape, much lighter than the tacky tape, was used along the wingspan.
- The connection of the strain gauges and the potentiometer to the data acquisition (DAQ) system was done using DB9 connectors. Usually, these sensors would be soldered directly to the cables of the DAQ system but, since the experiment requires switching between wings, it was more practical to install connectors that allow a temporary connection. However, this type of connection can generate noise in the measurements due to the movement of the cable. Therefore, the cables were fixed at different points of the test setup to provide strain relief and minimise the noise.

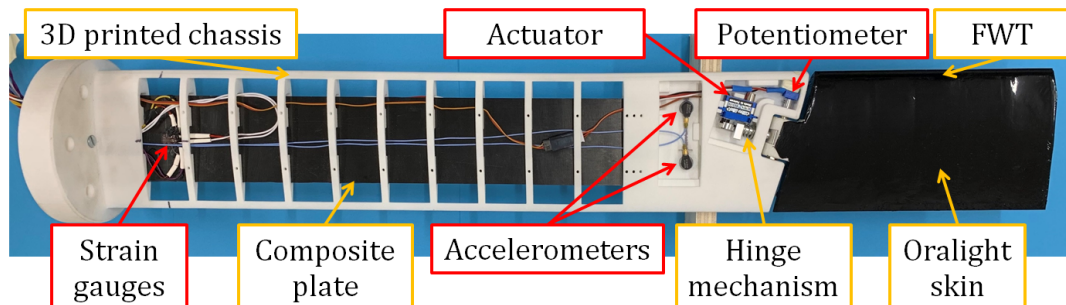


Figure 4.5: Wing model used in the experiments. Image before assembling the skin of the main wing

⁶Bourns 3310 series. Bourns, 2021. URL <https://www.bourns.com/products/potentiometers/industrial-panel-controls/product/3310>. Last accessed: 28 July 2021.

4.2. Data acquisition system

The design philosophy of the hinge mechanism presented in section 3.3 requires a real-time system that can monitor and record the aeroelastic response and actuate the hinge mechanism. For this experiment, the data acquisition and actuation cycles should be able to operate at a consistent frequency that is as high as possible, since this frequency governs part of the time delay between the gust detection and the response introduced by the control system. During the setup, it has been found that the success of the system depends on several factors related to the software and hardware used for the final implementation. Therefore, the simpler the system, the easier it is to control the time delays.

The first implementation of the system is based on the load threshold and hinge release in a closed-loop manner. The idea is to read the measurements from the strain gauges, convert them into loads, evaluate the threshold and then move the actuator accordingly. However, it was found that the hardware used is not capable of processing the signals and controlling the actuator at the desired frequency. Due to a combination of buffer limitations and poor optimization of resources, the actuation cycle is inconsistent and, usually, below the desired frequency. For this reason, the measurements have been decoupled from the control process by converting the feedback loop into a feedforward system that uses a trigger from the gust generator and adds a time delay to control at what load threshold the FFWT is released, hence simplifying the whole process.

The final data acquisition procedure is implemented following the system represented in the schematic in Figure 4.6. The gust generator creates a sequence of 1-cosine gusts with a fixed time interval. At the start of each gust, a trigger signal is generated and sent to both an Arduino UNO⁷ and a SCADAS Mobile⁸. The Arduino UNO is used to control the hinge release: when the trigger is received, the microcontroller waits for a specified time and then releases the mechanism; after a few seconds, the hinge mechanism is taken back to the locked position. The SCADAS is in charge of the data acquisition: it reads all the sensors, as well as the trigger signal from the gust generator and a control signal generated by the Arduino in order to keep track of the actuator motion. This signal is compared to the trigger and potentiometer signals to monitor the delays in the actuation chain. Finally, the SCADAS information is sent to a National Instruments cRIO-9744⁹ using EtherCAT communication. The procedure to set up this communication protocol with the mentioned hardware can be found in Appendix A. Last, the cRIO converts the electrical signals into the respective measurements making use of calibration constants and saves the data into the main computer.

To conclude this section some details about each of the elements of the system are given. First of all, the gust generator creates sequences of 1-cosine gusts of the desired characteristics and time delays between gusts. In addition, at the beginning of each gust, it generates an electric pulse, which can be used as a trigger for the Arduino and as a timestamp at the beginning of each sample to later process the data.

Second, the Arduino works in a cycle in which it waits for the trigger signal from the gust generator, adds the input delay to achieve the desired load threshold and then locks the mechanism once the measurement has finished. Therefore, the tests can run continuously without having to start an independent program.

Last, the Ethercat system integrates the SCADAS and the cRIO, as mentioned before. On the one hand, the SCADAS is configured as an Ethercat slave, cyclically sending the measurements to the cRIO. On the other hand, the cRIO is configured as the Ethercat master to read, process and save the measurements conducted by the SCADAS: during the test, the cRIO records these measurements and, when the test is concluded, the data is processed and sent to the main computer, which controls the cRIO, to be saved in a .txt file.

⁷Arduino UNO & Genuino UNO. Arduino, 2021. URL <https://www.arduino.cc/en/pmwiki.php?n=Main/arduinoBoardUno>. Last accessed: 28 July 2021.

⁸Simcenter SCADAS Mobile and SCADAS Recorder. Siemens - Community support, 2021. URL <https://community.sw.siemens.com/s/article/simcenter-scadas-mobile-and-scadas-recorder>. Last accessed: 28 July 2021.

⁹"cRIO-9074," National Instruments - Support, 2021. URL <https://www.ni.com/nl-nl/support/model.crio-9074.html>. Last accessed: 28 July 2021.

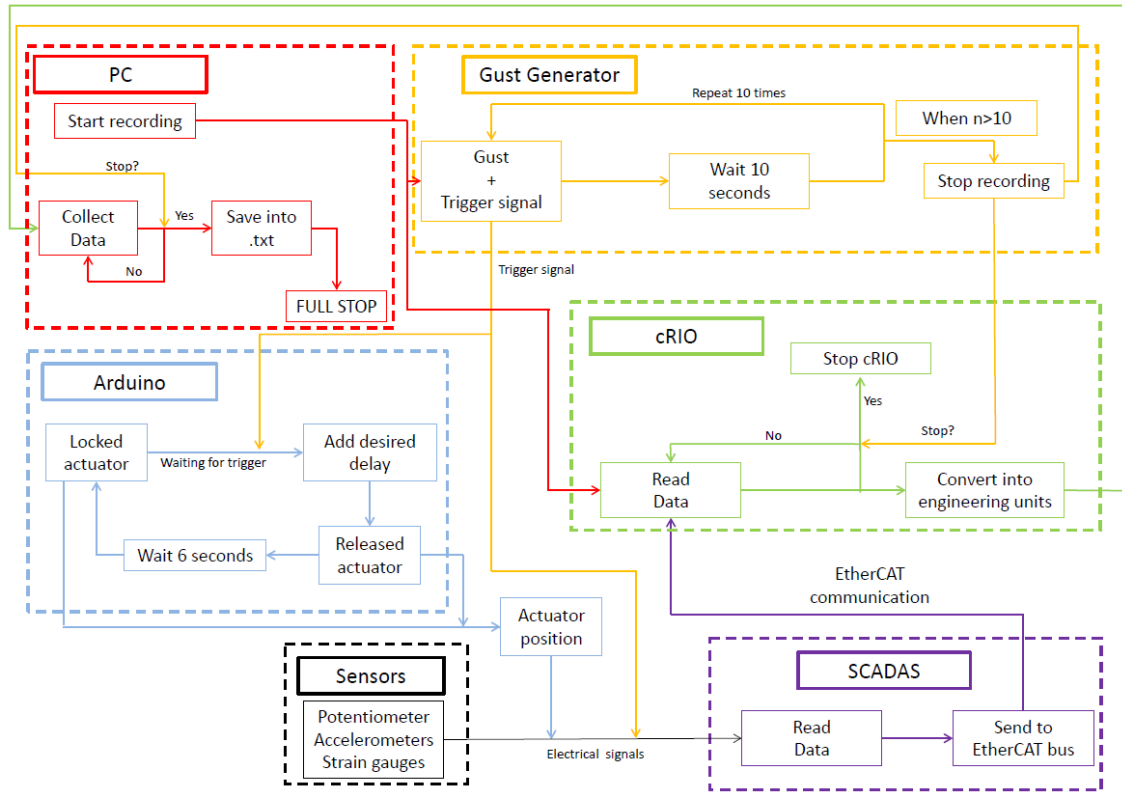


Figure 4.6: Schematic of the data acquisition and control system

4.3. Sensor calibration and data processing

This subsection presents the most relevant data processing steps required for the experiment. On the one hand, subsection 4.3.1 presents the procedure to calibrate the strain gauges and extract load measurements from the electrical signals. On the other hand, subsection 4.3.2 presents the parameters used to assess the results of the experiment. As a side note, notice that the statistical evaluation of the samples is not considered in this section but addressed as part of the acquisition strategy in subsection 4.5.4.

4.3.1. Strain gauge calibration

The strain gauge bridge requires a calibration to allow the determination of the loads from the bridge output. The linear transformation, $\bar{\mathbf{c}}$, is a matrix that relates the bending loads, M_X , and torque loads, M_S , to the strain gauge bridge signals, G , as presented in Equation 4.1.

$$\begin{pmatrix} G_{1-1'} \\ G_{2-2'} \\ G_{3-3'} \end{pmatrix} = \bar{\mathbf{c}} \begin{pmatrix} M_X \\ M_S \end{pmatrix} = \begin{pmatrix} c_{1,1} & c_{1,2} \\ c_{2,1} & c_{2,2} \\ c_{3,1} & c_{3,2} \end{pmatrix} \begin{pmatrix} M_X \\ M_S \end{pmatrix} \quad (4.1)$$

By applying pure bending and torque loads separately [13, 38], it is possible to obtain the calibration constants, $c_{i,j}$, using the least-squares (LS) solution according to Equation 4.2, where \mathbf{M}_j and \mathbf{V}_i are vectors of known loads and the signal of the strain gauge in i direction, respectively.

$$\mathbf{G}_i = c_{i,j} \cdot \mathbf{M}_j \rightarrow c_{i,j} = \left(\mathbf{M}_j^T \mathbf{M}_j \right)^{-1} \mathbf{M}_j^T \mathbf{G}_i \quad (4.2)$$

Once the calibration constants are known, the inverse transformation, $\bar{\mathbf{C}}$, can be computed using the pseudo-inverse concept already used in the LS solution:

$$\mathbf{G} = \bar{\mathbf{c}}\mathbf{M} \rightarrow (\bar{\mathbf{c}}^T \bar{\mathbf{c}})^{-1} \bar{\mathbf{c}}^T \mathbf{G} = \mathbf{M} \rightarrow \mathbf{M} = \bar{\mathbf{C}}\mathbf{G} \quad (4.3)$$

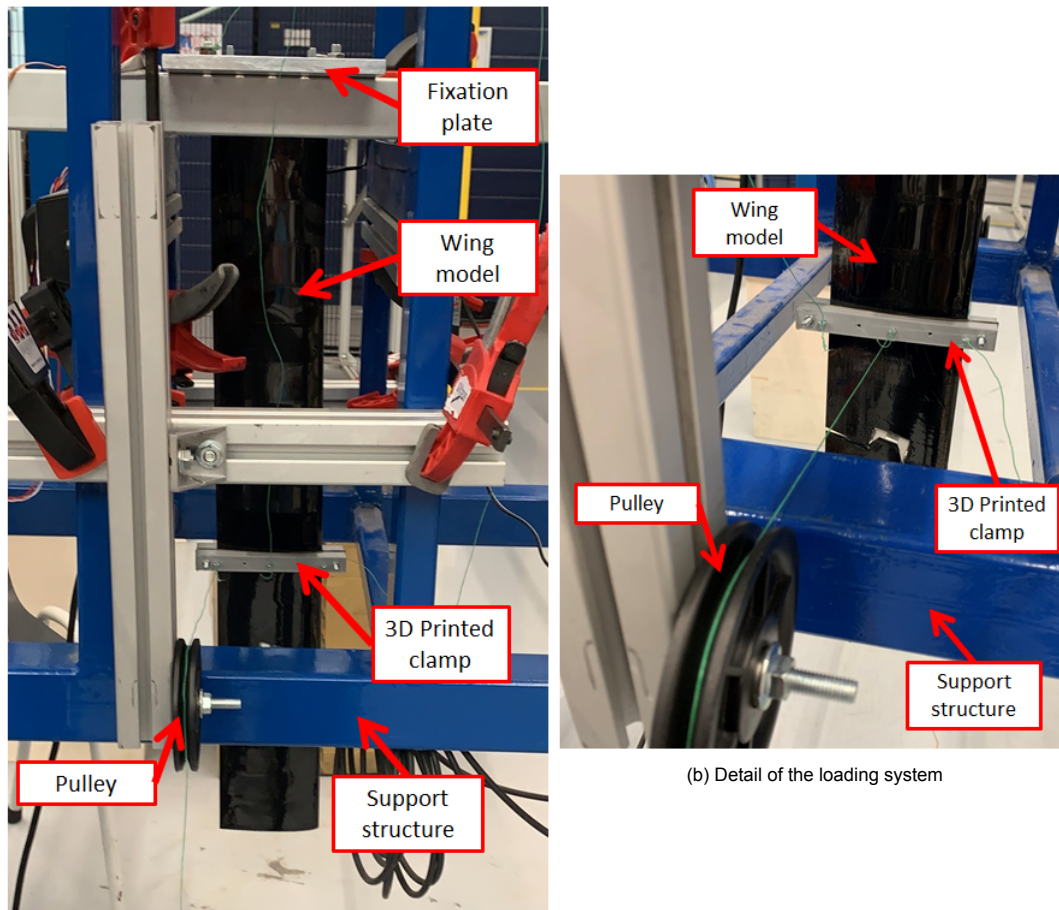
$$\begin{pmatrix} M_X \\ M_S \end{pmatrix} = \begin{pmatrix} C_{1,1} & C_{1,2} & C_{1,3} \\ C_{2,1} & C_{2,2} & C_{2,3} \end{pmatrix} \begin{pmatrix} G_{1-1'} \\ G_{2-2'} \\ G_{3-3'} \end{pmatrix} \quad (4.4)$$

This calibration procedure is carried out using the test rig presented in Figure 4.7. A 3D printed wing clamp is positioned at a known distance, h , from the strain gauges to apply a shear force, which is exerted by a weight that hangs from the pulley. First, Figure 4.8a presents a pure bending load, M_X , which can be related to the weight, W , using Equation 4.5. Next, Figure 4.8b presents a pure torque load, M_S , applied using a force couple that can be related to the torque with Equation 4.6, which uses the mid-chord point, O_M , as the reference point to compute the moment. Finally, a combined load can be obtained by applying the weight as in Figure 4.8c. In this case, the loads are defined by Equation 4.7.

$$M_X = hW \quad (4.5)$$

$$M_S = cW \quad (4.6)$$

$$M_X = hW; M_S = cW/2; \quad (4.7)$$



(a) Overview of the test rig

(b) Detail of the loading system

Figure 4.7: Strain gauges calibration test rig

The results of the strain gauge calibration are presented in Table 4.1, which presents the calibration constants from matrix $\bar{\mathbf{C}}$. In addition, Figure 4.9 shows an example of the load curves used to obtain these constants, in which pure bending loads in the range of ± 1100 Nmm and pure torque in the range

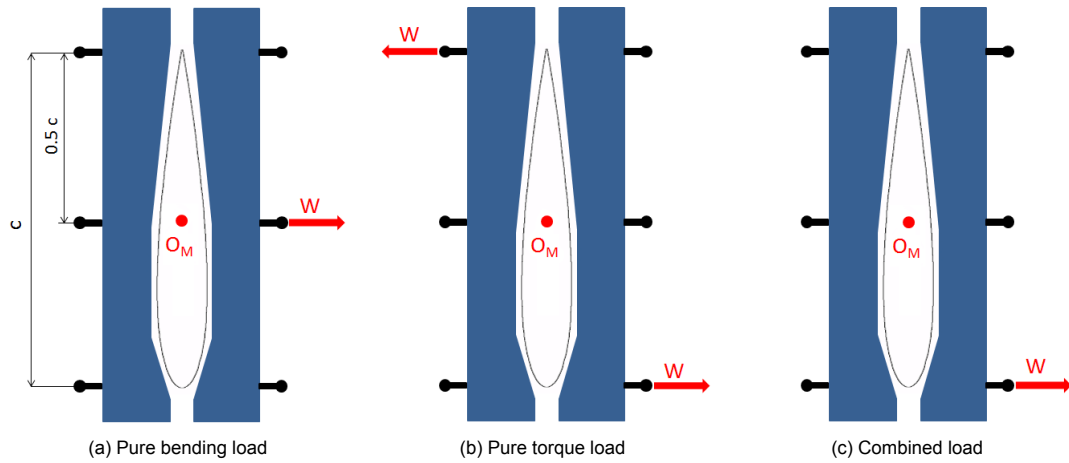


Figure 4.8: Diagrams of applied loads during the calibration procedure

of ± 200 Nmm are used. As a side note, these ranges are based on the expected loads obtained from the simulations to ensure that the calibration encompasses the loads that will be seen in the experiment.

Table 4.1: Calibration constants (Equation 4.4) of each wing computed using the least-squares (LS) methodology.

Wing	C_{11} [Nmm/mv]	C_{12} [Nmm/mv]	C_{13} [Nmm/mv]	C_{21} [Nmm/mv]	C_{22} [Nmm/mv]	C_{23} [Nmm/mv]
A	-164.3	-385.5	-136.5	-411.1	-71.6	432.5
B	-192.8	-497.3	-171.4	-470.8	-125.6	431.3
C	188.1	-639.5	-83.5	424.0	-294.0	721.7
B _{WI}	-178.9	-599.9	-212.9	-469.9	45.1	422.2
B _{WO}	-318.7	-504.6	-16.8	-482.6	-187.5	429.3

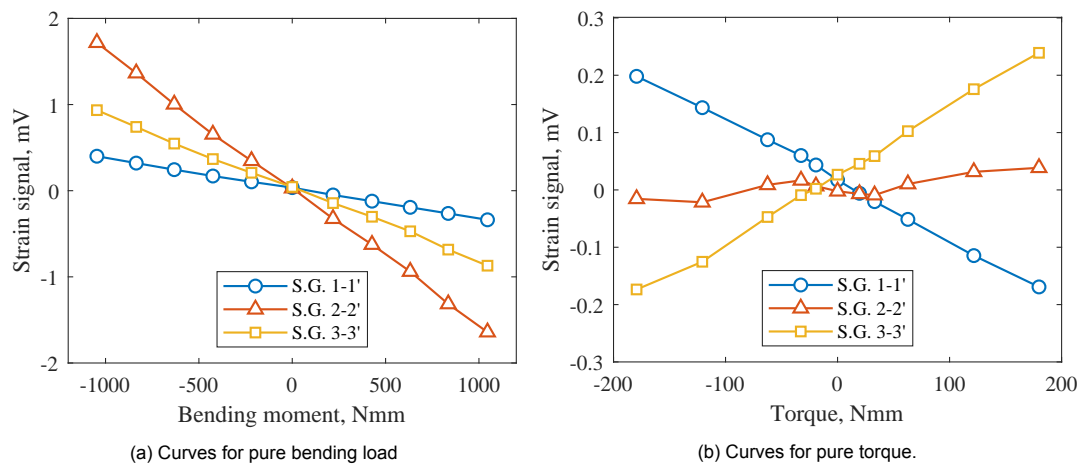


Figure 4.9: Strain-Load curves obtained in the calibration procedure to compute the calibration constants

First of all, both the bending loads and torque present a linear response, which shows that the linear calibration previously described is suitable to compute the loads from the bridge signals. Then, looking at Figure 4.9a, it can be seen that all of the half-bridges respond to bending. Furthermore, the central bridge shows the largest response, agreeing with the expectations presented in Figure 4.4a. On the other hand, the responses to torque from Figure 4.9a are in agreement with the expectations presented in Figure 4.4b: the central bridge does not respond to torque and the other bridges show responses opposed in sign. In addition, it is important to remark that the magnitude of the maximum strains produced by torque is much lower than that produced by the bending loads. Therefore, it is expected that the responses will be dominated by the bending loads.

To conclude, although the calibration is done with pure bending loads and pure torque, the experi-

ment will present combinations of both. Therefore, the calibration is validated by applying combinations of bending and torsion loads and comparing them to the loads obtained after transforming the strain gauge signals with the calibration matrix. The loads are applied as shown in Figure 4.8c, using loads in the range of ± 2.4 N, corresponding to bending moments in the range of ± 840 Nmm and torsion loads in the range of ± 120 Nmm. The results are presented in Figure 4.10, which shows a comparison of the applied loads and the computed loads for each of the wings. As shown in Table 4.2, the maximum error for the bending moment is below 10%. However, the error in the torque measurement can reach up to 80% and is very inconsistent between wings. These differences could be caused by the cross-measurement of the $\pm 45^\circ$ strain gauges since these strain gauges are affected by both bending and torque loads, as previously mentioned. This is not the case for the central strain gauge oriented along the span which is only affected by bending loads. Therefore, given the difference in magnitude of the strains caused by the bending load and those caused by torque, the measurements of the $\pm 45^\circ$ strain gauges are dominated by bending, which reduces the accuracy of the torque measurements obtained from the calibration matrix. In view of this limitation, the torque is not considered in the results.

Table 4.2: Comparison of maximum relative error between the calibrated measured load and the applied load

Wing	A	B	C	B _{WI}	B _{WO}
Bending [%]	5.5	-7.7	6.8	-6.5	-3.6
Torque [%]	81.2	14.4	-23.8	36.7	35.9

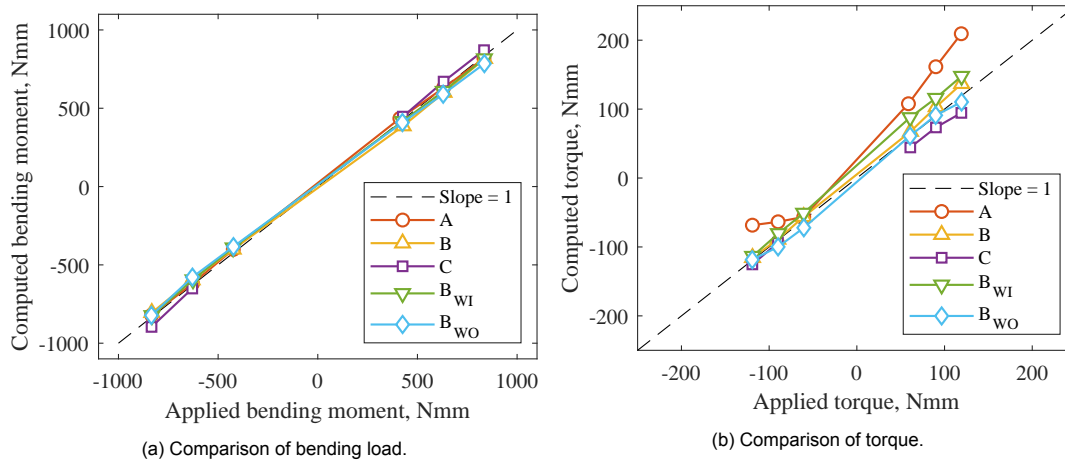


Figure 4.10: Comparison between applied load and loads computed from the strain gauge signals using the calibration matrices from Table 4.2.

4.3.2. Metrics for GLA assessment

The assessment of the results is carried out using the bending moment coefficient, C_B , defined by Equation 4.8. From the load time response, two main parameters are studied: peak loads and root mean square (RMS). Figure 4.11 shows an example of the variation of the bending moment coefficient over time at $\alpha = 5^\circ$. The peak load, ΔC_B , is defined as the difference between the maximum load, $C_{B,max}$, and the mean pre-release steady-state load, $C_{B,pre}$, i.e. the static load before the gust hits the wing.

$$C_B = \frac{M_x}{\frac{1}{2}\rho S B U_\infty^2} \quad (4.8)$$

On the other hand, the RMS is used as an indicator of the persistence of the oscillations in the load signals [52]. As can be seen in Figure 4.11, when the wing is hit by the gust, the load oscillates around a steady load that is achieved after the gust. Accordingly, the RMS gives an indicator of how much the signal deviates from the steady load, hence the oscillations that persist for a longer time result in a

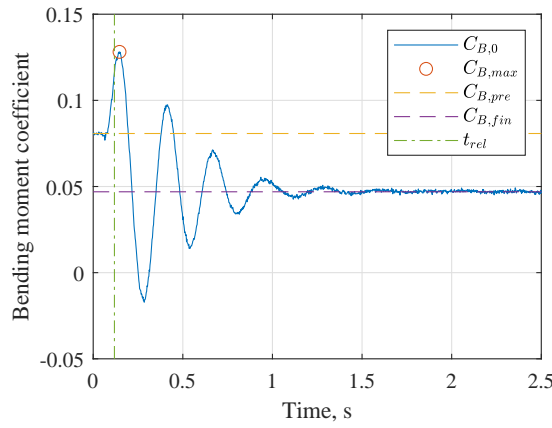


Figure 4.11: Terminology used for processing the data

higher RMS value. Since there are two steady states corresponding to the locked-hinge and free-hinge conditions, the RMS is calculated using $\tilde{C}_B(t)$, as defined in Equation 4.9.

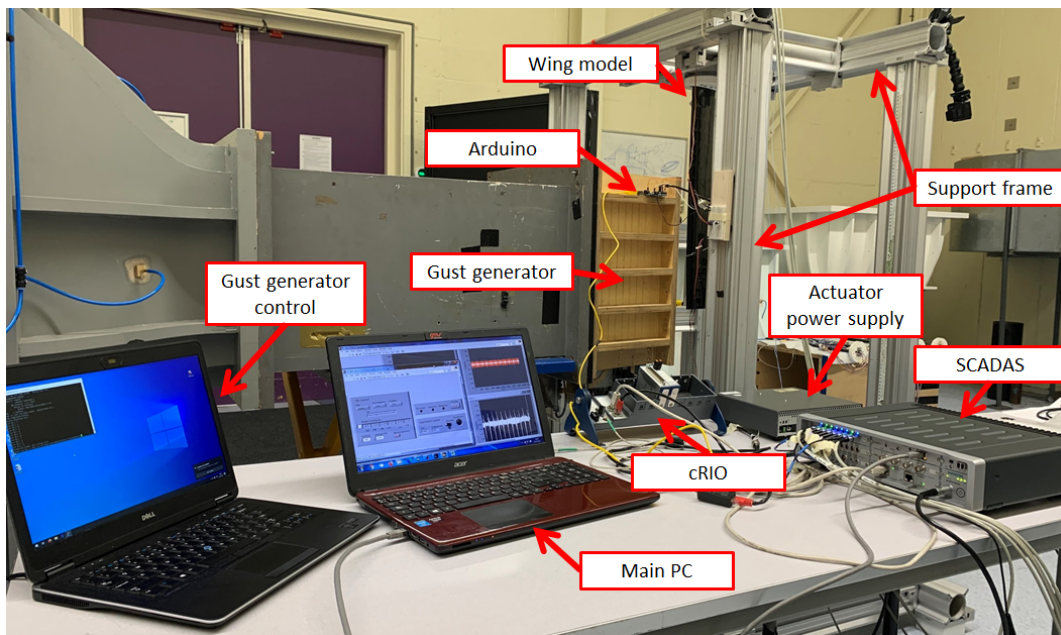
$$\tilde{C}_B(t) = \begin{cases} C_{B,0}(t) - C_{B,pre} & \text{for } 0 < t < t_{rel} \\ C_{B,0}(t) - C_{B,fin} & \text{for } t > t_{rel} \end{cases} \quad (4.9)$$

4.4. Wind tunnel setup

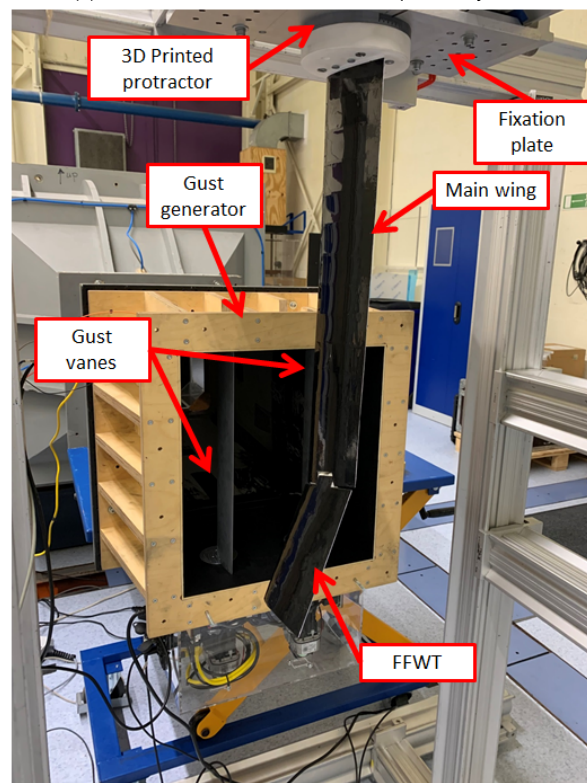
The experiments are conducted in the W-Tunnel at the Delft University of Technology, which is an open jet wind tunnel with a square test section of $0.4 \times 0.4 \text{ m}^2$. The tests are performed at a freestream velocity of 10 m/s ($Re \approx 67000$), which has to be reduced with respect to the original design freestream velocity of 15 m/s ($Re = 100000$) due to the occurrence of flutter, as further addressed in chapter 5. In addition, due to the reduction of the freestream velocity, the aerodynamic loads are reduced and the wing response becomes weight dominated. Therefore, the orientation of the wing is changed to vertical, making the aeroelastic forces dominate the response.

Finally, the different elements involved in the experiment and presented in previous sections are summarized in the following overview of the complete setup. In Figure 4.12, an overview of the data acquisition system and the test object are presented. The main elements of the test setup are the following:

- **Gust generator:** The gust generator is a wooden $0.4 \times 0.4 \text{ m}^2$ extension attached to the wind tunnel nozzle with two aluminium gust vanes operated by electrical motors and controlled through an in-house program. The system can generate continuous sine gusts or discrete 1-cosine gusts. The 1-cosine gusts used in this investigation can be generated at frequencies ranging from 0 Hz to 12 Hz in increments of 0.5 Hz and gust amplitudes, δ_g , between 0° and 7.5° .
- **Wing model:** Wing model discussed in section 4.1 consisting of the main wing and the FFWT.
- **Support structure:** Structure of X95 beams assembled around the wind tunnel section and used to hold the wing model in a vertical position. The wing is attached to an intermediate 3D printed part, used as a protractor with angular marks to measure the geometrical angle of attack. At the same time, these parts are attached to an aluminium plate designed to be attached to the beams using standard clamps for the X95 beams.
- **Data acquisition and control system:** System discussed in section 4.2 consisting of the gust generator, cRIO, SCADAS, Arduino UNO and control PC.
- **Power supply:** Power supply used for the actuator. The actuator could be powered by the Arduino, but the microcontroller has a limited current output. To avoid this limitation, the external power supply is used.



(a) Overview of the control and data acquisition systems



(b) Overview of the gust generator and test object

Figure 4.12: Wind tunnel setup

4.5. Acquisition strategy

The definition of the experiment can be concluded by discussing the measurements that are taken to answer the research questions and the conditions in which the experiment is carried out. For each of the wings, the experiment is divided into four sections: stability analysis, modal analysis, static aerodynamic loads analysis and gust loads analysis.

4.5.1. Stability analysis: flutter

For the investigation of the gust alleviation performance, the model must remain stable across the test cases. Therefore, the first analysis is dedicated to addressing the stability limitations of the wings, so the test conditions for the next sections can be defined.

In this first section, the flow speed is increased in steps of 1 m/s and the wing is excited to observe its response at different angles of attack until the wing becomes unstable. The wing is considered unstable when the transient response becomes divergent. With these results, a flow speed such that all the wings are stable in the test conditions can be selected.

4.5.2. Modal analysis: modal impact test

A modal impact test is carried out to assess the accuracy of the numerical model and define the test cases for the dynamic analysis. On the one hand, the natural frequencies allow a comparison with the results of the numerical modal analysis. This comparison provides insight into how accurate the stiffness and mass distribution of the numerical model is.

On the other hand, it is desired to see the effect on the GLA performance when exciting the wings at their natural frequencies. For this reason, the 1st bending and 1st flapping frequencies are used in the gust analysis, as will be seen in subsection 4.5.4.

4.5.3. Static loads analysis: bending moment coefficient polars

The static behaviour of the wings is characterized by changing the angle of attack, α , between -6° and 14° . These measurements are carried out in both free-hinge and locked-hinge conditions at the flow speed defined by the stability analysis. The results are collected in polar curves of the bending moment coefficient, C_B , defined by Equation 4.8, and the fold angle, β . The test cases are presented in the overview of Table 4.3.

4.5.4. Dynamic loads analysis: 1-cosine gusts

To conclude, the time response of the wings to a 1-cosine gust excitation is recorded for different angles of attack, gust frequencies, and release thresholds. Like in the static analysis, the flow speed is defined by the results of the stability analysis.

The variation in the angle of attack separates a purely dynamic load ($\alpha = 0^\circ$) from a more representative combination of dynamic load and static load introduced by a non-zero angle of attack ($\alpha = 5^\circ$). The gust frequencies selected for the experiment are spread below, above, and close to the natural frequencies in free-hinge and locked-hinge conditions to cover a broad dynamic range. As seen in subsection 4.5.2, these natural frequencies are found with a modal impact test, which is performed in-situ when the wing is mounted in the wind tunnel.

Finally, the threshold variations include the free-hinge and locked-hinge conditions as a reference and different release conditions during the gust: i) released with the gust generator trigger signal before the gust hits the wing, ii) when the gust hits the wing, i.e. the load starts increasing, iii) it is released when the load achieves 50% of its peak load, and iv) at the peak load. These release conditions are referred to as pre-released, 0%, 50%, and 100% release, respectively. In addition, after the first parameter exploration study, it is found that the gust amplitude does not have a strong effect on the results, hence it is decided to fix it at 2.5° . An overview of the test cases and variations of parameters are presented in Table 4.3.

For each specific dynamic testing condition, the experiment is repeated 10 times to allow for statistical evaluation of the measured aeroelastic responses. An example of this evaluation is presented in Figure 4.13, which shows the bending moment coefficient response of wing C at $\alpha = 5^\circ$ for a gust frequency of 3.5 Hz, i.e. 1st bending natural frequency, and a hinge release at 50% of the peak load. Figure 4.13a presents the samples before filtering, from which two problems can be observed. On the one hand, some samples achieve peak values lower than the average. This deviation could be related to the mechanism not properly locking the FFWT before releasing it, hence these samples must be discarded. On the other hand, one sample shows jumps in the signal caused by hardware limitations,

Table 4.3: Overview of test cases

Parameter	Static Load	1-cosine gust
Wing		A, B, C, B _{WI} , B _{WO}
Hinge condition	Free, Locked	Free, Locked, Pre-released, 0%, 50%, 100%
α [°]	[-6, 14]	0, 5
Gust amplitude [°]	-	2.5
Gust frequency [Hz]	-	0.5, 5, 8, 1st Bending, 1st Flapping

thus it also has to be discarded. Next, the results after filtering these samples can be seen in Figure 4.13b. Notice that, in two of the samples, there is a load increase before the measurement stops, which is a consequence of the manual recovery of the FFWT position. In some cases, the FFWT is moved back to the locked position too early, leading to this load change before the end of the sample. Nevertheless, the study focuses on the response until the loads become steady, hence only the first three seconds of the signal are used. This can be seen in Figure 4.13c, which presents the average signal used for the peak load and RMS study and does not include the last second of the sample, in which the manual recovery affected the bending moment. Furthermore, the shaded region around the averaged signal represents the standard deviation of the measurements. In addition to the test case for which the procedure has been presented, Figure 4.13c includes the results of the wing and gust conditions but with the hinge in free and locked conditions. These results show that the deviations in the measurements are consistent across the experiment, although they are higher when the hinge is released in the middle of the gust. To conclude, the final result of this filtering step is an average sampling rate of 450 Hz across the experiment and a minimum of 6 samples per test case.

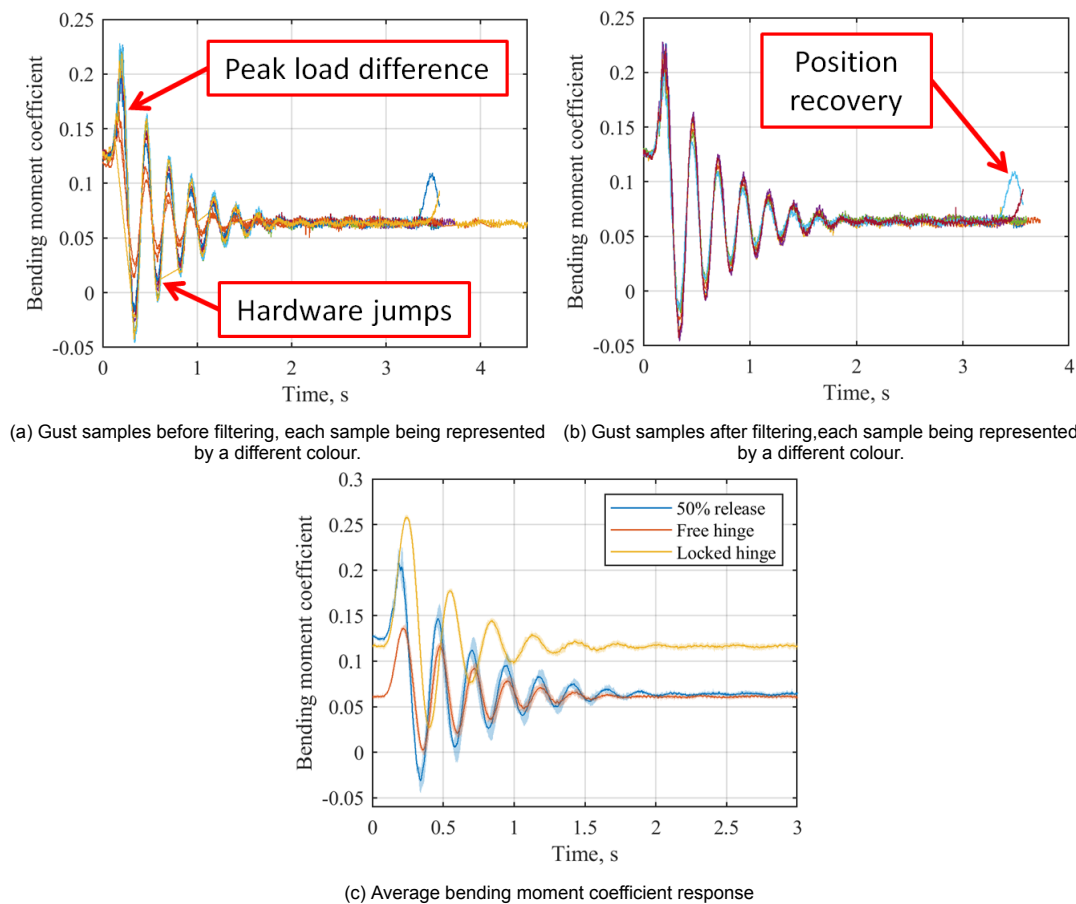


Figure 4.13: Filtering procedure for dynamic test cases. Example from wing C at $\alpha = 5^\circ$, 3.5 Hz (1st bending natural frequency) and hinge release at 50% of the peak load.

5

Results

The experimental results are presented in this chapter and, where possible, compared with the numerical results. In the initial phase of the wind tunnel campaign, it has been discovered that the actual flutter speed is considerably lower than expected. As a result, the free stream velocity has to be reduced to operate in safe, flutter-free conditions across all the wings. As a consequence, it has been decided to measure the wings in a vertical orientation to avoid their response dominated by weight rather than aeroelastic forces.

5.1. Stability study: flutter

After the first design space exploration, in which the flutter speed is found to be below the design speed of 15 m/s used in the simulations, a stability analysis is necessary to redefine the subsequent sections of the experiment. The results of this analysis are presented in the comparison between wings presented in Figure 5.1 and Table 5.1, which presents the simulated flutter speeds and measured flutter speeds at $\alpha = 0^\circ$. Furthermore, the wings are also tested in the locked-hinge condition but do not show sustained or divergent instabilities below 25 m/s. As a side note, higher speeds have not been tested as a safety measure to avoid damage on the wings before completing the tests, which could happen if the sizing loads are exceeded.

It can be seen how the trends observed in the experimental results are the same observed in the simulations but at lower speeds. The increase in the flutter speed across wings A, B, and C shows the expected result of increasing bending stiffness delaying flutter. Considering the tailored wings, the flutter speed of wing B_{WI} is the lowest while the flutter speed of B_{WO} is the highest, which is in agreement

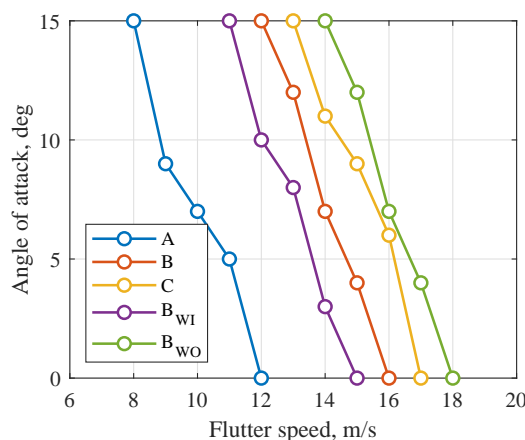


Figure 5.1: Comparison of flutter speeds at different angles of attack for each wing

Table 5.1: Comparison between experimental and simulated flutter speeds at $\alpha = 0^\circ$.

Wing	A	B	C	B _{WI}	B _{WO}
Simulation [m/s]	19.9	21.1	23.0	20.4	22.9
Experiment [m/s]	12 (-40%)	16 (-24%)	17 (-26%)	15 (-26%)	18 (-21%)

with the observations presented in section 3.2. In this regard, the experiments confirm that the FFWT in a hinge-free condition can considerably alter the aeroelastic stability behaviour of tailored composite wings.

In addition, the relative decrease of the flutter speed with respect to the simulation remains approximately constant for all the wings except for wing A. Although the reason for this behaviour is still not clear, two possible explanations have been considered. First, wing A is the most flexible one, hence the one facing the highest deflections and the most affected by structural nonlinearities. Therefore, the limitations of the linear numerical model might be magnified by combining the aerodynamic nonlinearities of the FFWT with the structural nonlinearities. Second, a manufacturing imperfection, such as a difference in the shrinking of the skin foil, could lead to differences in the results. However, the shrinking process has been carried out taking particular care on applying the same shrinking in all of the wings. This can be seen in the approximately constant relative difference in all wings but A, which shows that a manufacturing imperfection to produce such a difference would be noticeable before and after the experiments. Since it is not the case, it is hard to believe that the difference is originated in the manufacturing of the wings.

Finally, the agreement between the trends seen in the experiment and those from the numerical results shows that the model offers a good representation of the aeroelastic problem but needs to be improved to better match in a quantitative sense. Therefore, a ground vibration test (GVT) is planned as future work to correlate the numerical model with the experiment and update the stiffness and mass properties accordingly¹.

5.2. Modal analysis: modal impact test

Table 5.2 compares the numerical and experimental results for the first natural frequencies of the tested wings in both locked-hinge and free-hinge conditions. It can be seen how the simulations follow similar trends as the experiments but there is an offset between the frequencies from the simulation and the experiment. Looking at this offset, it can be seen that each mode has a different offset but is approximately consistent between wings: 0.5 Hz for the 1st bending mode, 0.08 Hz for the 1st flapping and 1.2 Hz for the 2nd flapping. This could be caused by an overprediction of the stiffness and a misprediction of the mass and centre of gravity of the wing. Taking into account that the simulations rely on modal analysis for the flutter predictions, these discrepancies could explain the overprediction of flutter speed and a model update as suggested could improve the results.

Notice also that the 1st flapping frequency is the same for all the wings and the offset is much lower than for the other modes. Looking at the representation of this mode in the simulation, it can be seen that the mode is dominated by the wingtip motion, as shown in Figure 3.12b. Therefore, the mode is mostly affected by the properties of the wingtip and the hinge, which are the same between the different wing models, while the frequency is approximately independent of the properties of the main wing. Hence, the similarity in magnitude between the experiment and the simulations could mean that the wingtip properties have been modelled correctly.

Finally, the 1st bending and 1st flapping frequencies are used as one of the gust excitation frequencies during the gust experiments to study the effect on the GLA performance of exciting the wings at their natural frequencies. However, the gust generator can only produce gusts of frequencies from 0.5 Hz to 12 Hz in steps of 0.5 Hz, therefore the excitation frequencies are rounded to the closest possible frequencies considering the results from the impact test. As a result, the 1st flapping frequency used in the experiment is 1.5 Hz for all the wings and the 1st bending frequency is 3.0 Hz for all but wing C,

¹The tests have already been conducted but the correlation and update of the numerical model have been considered out of the scope of this thesis. For this reason, the methodology and setup used in this test are presented in Appendix B instead of the main body of the thesis.

which is tested at 3.5 Hz.

Table 5.2: Comparison of natural frequencies obtained from modal impact test and simulation

Wing Source	A		B		C		B _{WI}		B _{WO}	
	Exp.	Sim.	Exp.	Sim.	Exp.	Sim.	Exp.	Sim.	Exp.	Sim.
1st Bending [Hz]	2.76	3.28 (+18.8%)	3.03	3.55 (+17.2%)	3.42	3.87 (+13.2%)	3.23	3.62 (+12.1%)	3.23	3.58 (+10.8%)
1st Flapping [Hz]	1.33	1.40 (+5.2%)	1.33	1.41 (+6.0%)	1.33	1.42 (+6.8%)	1.33	1.41 (+6.0%)	1.33	1.41 (+6.0%)
2nd Flapping [Hz]	3.49	4.82 (+38.1%)	3.90	5.13 (+31.5%)	4.40	5.55 (+26.1%)	4.09	5.25 (+28.4%)	4.10	5.17 (+26.1%)

5.3. Static loads analysis: bending moment coefficient polars

The moment coefficient polar is the first step to understanding the impact of the design variations on the exerted aerodynamic loads. Due to the manufacturing deviations between models and the accuracy of the angle of attack measurement, the loads at an angle of attack of 0° are not zero although the airfoil is symmetric. Therefore, for a comparison between wings, the curves are offset to achieve no load at an angle of attack of 0°.

Figure 5.2 shows the example of the bending moment coefficient and fold angle polars for wing B, which shows a behaviour similar to the other wings. The load alleviation due to the released FFWT can be clearly observed by the reduced slope of the bending moment coefficient line, which is in agreement with the observations presented by Cheung et al. [20]. Notice also that, for high angles of attack, the bending moment decreases while the measurement deviations increase, which could be related to boundary layer separation. Furthermore, the fold angle polar shows how the FFWT rotates to keep the load equilibrium at the hinge when the wingtip is released. In addition, for the example of wing B when the hinge is locked, the measured angle is not zero but varies in the range of ±1°. This could be caused by the compliance of the hinge locking mechanism, allowing some displacement of the FFWT. To conclude this section, Table 5.3 presents a summary of the results of the different wings, including

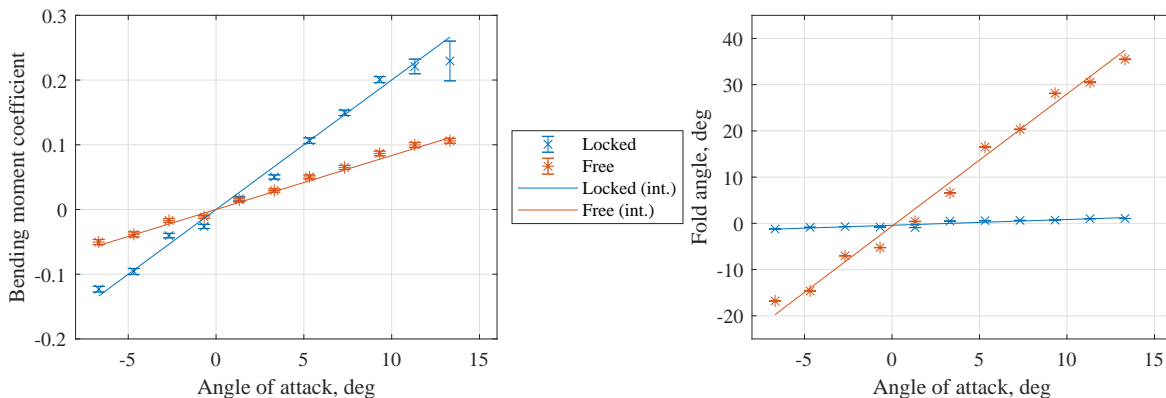


Figure 5.2: Wing B interpolated C_B and β polars

Table 5.3: Slopes and stall angles obtained from C_B polars. Slopes presented in counts ($C_B = 0.0001 = 1$ count)

Wing	Locked $C_{B,\alpha}$ [1/°]	Free $C_{B,\alpha}$ [1/°]
A	200	89
B	200	83
C	199	85
B _{WI}	204	73
B _{WO}	173	75

the polar slope in locked and free conditions. On the one hand, wings A, B, and C present the same locked slope, which shows that the results are not significantly affected by the bending stiffness. On the other hand, the slope for wing B_{WO} decreases due to the added bend-twist coupling caused by the wash-out tailoring. This behaviour is reversed for B_{WI}, although the effect on the slope with respect to

the reference wing, B, is not as clear as for B_{WO} . The asymmetry in the response between the tailored wings could be caused by imperfections in manufacturing, such as the alignment of the plate within the wing or the shrinking of the skin foil. Finally, Figure 5.3 presents the results of the tailored wings to visualize these effects.

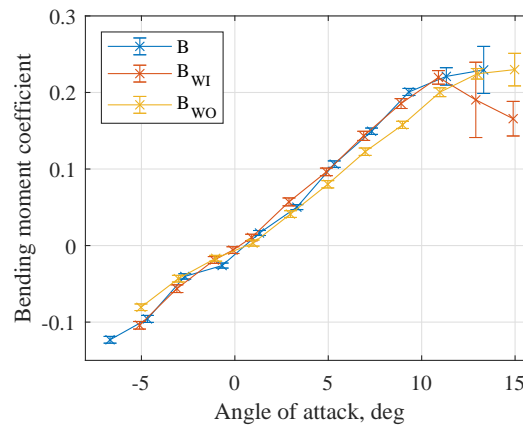


Figure 5.3: Bending moment coefficient polars comparison between tailored wings

Finally, when the hinge is released, wings A, B, and C present different slopes but do not follow a trend that could be related to the differences in bending stiffness. In addition, the slopes presented by the tailored wings are almost the same and lower than the reference slope of wing B, contrary to the expected results seen in the locked condition.

5.4. Dynamic load: 1-cosine gusts

The last part of the experiment studies the dynamic response of the wing when hit by 1-cosine gusts to assess the GLA performance of the FFWT. Before addressing the results, the response of the system is characterized by studying the time delays introduced during the actuation process.

5.4.1. System characterization

When studying the time response of the different wings, it is found that the release time of the hinge mechanism has a great impact on the FFWT performance. For this reason, it has been considered necessary to characterize this response before addressing the GLA performance. Thus, there are two possible sources of time delay.

The first source of time delay originates from the Arduino requiring time to process the input and to release the hinge, as shown in Figure 4.6. Therefore, to know how fast this processing is, the delay given as an input is compared to the time elapsed between reading the trigger signal from the gust generator and the Arduino changing the position signal sent to the actuator. Then, the difference between these times is the time that the microcontroller needs to process the trigger signal. This delay is analysed across all the test cases and amounts to an average delay of 2 ms with a standard deviation of 1.3 ms.

The second source of the time delay originates from the time it takes between sending the signal to move the actuator and the structure to start moving. To study this delay, the release instant given as input is compared to the wingtip position obtained from the measurement of the potentiometer: the structure is considered to start reacting when the potentiometer position changes by more than 1° . A representation of this time delay is presented in Figure 5.4, which shows that the potentiometer does not start moving immediately after sending the signal to the actuator. It is found that this delay is 50 ms on average with a standard deviation of 7 ms.

Finally, the importance of these delays depends on the gust frequency as quantified in Table 5.4 by converting the time delays into relative delays with respect to the gust period. The 2 ms delay introduced by the Arduino can be neglected for all gust cases, as it represents less than a 2% of the

gust period. However, the 50 ms delay required for the structure to react becomes significant for the fast gusts. On the one hand, for the long gusts, 0.5 Hz, the delay remains below 5% of the gust period. On the other hand, this delay represents more than 20% of the gust period for the 5 Hz and 8 Hz gusts. This can be seen in Figure 5.5, where an example of time response at 0.5 Hz is compared to an example at 8 Hz. In the 0.5 Hz gust, when the hinge is released at 50% of the peak load, a 50 ms delay results in an effective release threshold of 60%, while the same delay at 8 Hz leads to an effective release threshold of 90%. Therefore, it is necessary to consider these delays when assessing the load alleviation performance of the wings.

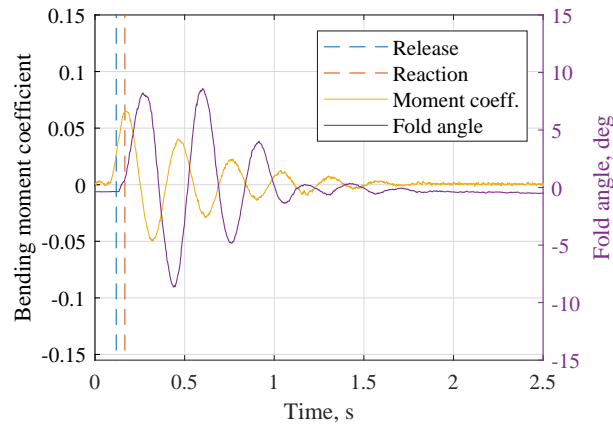
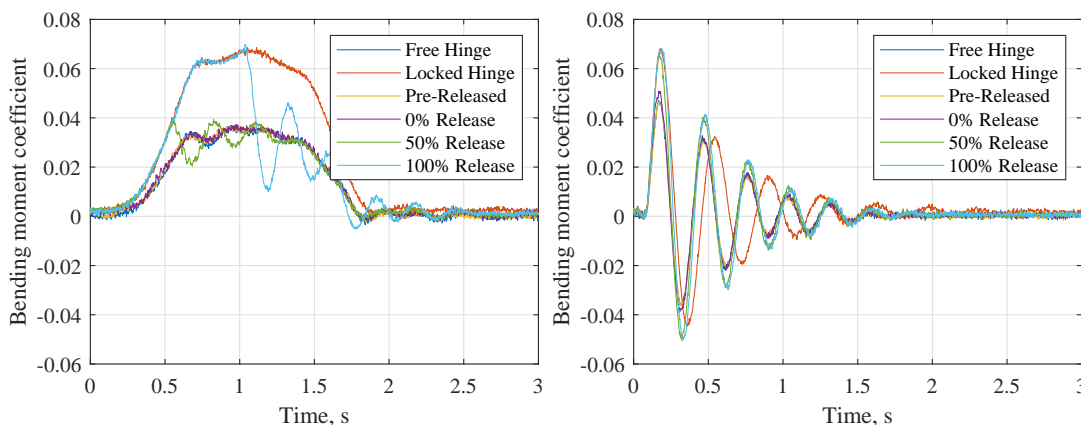


Figure 5.4: Example of delay between actuator signal release and wingtip response. Example of Wing A, $\alpha = 0^\circ$, 5 Hz gust and 50% release

Table 5.4: Comparison between gust periods and time delays introduced during the release

Gust		2 ms delay		50 ms delay	
Frequency [Hz]	Period [ms]	Relative delay [%]	Phase delay [°]	Relative delay [%]	Phase delay [°]
0.5	2000	0.1	0.4	2.5	9
1.5	667	0.3	1.1	7.5	27
3.0	333	0.6	2.2	15.0	54
3.5	286	0.7	2.5	17.5	63
5.0	200	1.0	3.6	25.0	90
8.0	125	1.6	5.8	40	144



(a) Bending moment time response for 0.5 Hz gust

(b) Bending moment time response for 8 Hz gust

Figure 5.5: Comparison of time response for different release thresholds at different gust frequencies. Example from Wing A at $\alpha = 0^\circ$

5.4.2. GLA performance

The GLA performance of the FFWT is assessed by comparing the peak loads and RMS with the performance of the wing with a locked hinge. First, the relative peak loads at $\alpha = 0^\circ$ are addressed to study the case in which no static load is applied. Then, the case in which $\alpha = 5^\circ$ is studied to see the effects of including a static load. Afterwards, the induced oscillations are studied with the relative RMS. Similar to the investigation of the peak loads, the case in which $\alpha = 0^\circ$ is addressed first and then the study is concluded with the $\alpha = 5^\circ$ case.

Figure 5.6 presents a comparison of the relative peak load alleviation between wings for different gust frequencies and release thresholds at $\alpha = 0^\circ$. From these results, interesting remarks can be made regarding the release threshold and the peak loads when the hinge is released close to the peak load. First, the free hinge can produce a peak load reduction between 30% and 50%, depending on the gust frequency and the wing stiffness. In agreement with the expectations, the peak load reduction is reduced with the delay in the release, as the wing is allowed to achieve higher loads before the hinge is released. Nevertheless, when the hinge is released at 100% of the peak load, the FFWT can increase the peak loads with respect to the locked-hinge condition. Notice also that this load increase depends on the gust frequency: for the 0.5 Hz gust, the peak increase can only be seen in the 100% release while, for the gust at 8 Hz, the load increase is also observed at 50% release. Furthermore, it can be seen how the load alleviation for the 50% release is progressively reduced with the increase of the gust frequency: for 0.5 Hz gust, the alleviation is similar to the free-hinge condition while an increase in the loads can be observed for 8 Hz gusts. This change can be explained by the delays introduced by the release system. As seen before, the release threshold is higher than desired as a consequence of the delays and, depending on the gust frequency, the increase in the load threshold becomes more important. Therefore, the reduction in load alleviation seen with the increasing gust frequency is not directly caused by the gust frequency but by the change in release threshold caused by the actuation time.

When comparing the different wings, wing B shows consistently lower load alleviation for all hinge conditions but the free hinge. This is true not only when comparing to the different stiffness wings, A and C, but also when comparing to the tailored wings, B_{WI} and B_{WO} . Overall, all wings but B present similar load alleviation capabilities without consistent trends that could be attributed to the structural properties of the wings. However, when the hinge is free, it is possible to see that the increasing stiffness coincides with an increase in load alleviation.

To find a possible explanation for the lower load alleviation achieved by wing B, the time responses of this wing are further studied. It is found that the processing delay mentioned in subsection 5.4.1 is higher than the average in wing B: while all the wings present an average processing delay of 45 ms, this delay in wing B achieves 65 ms. Therefore, wing B is 20 ms slower when releasing the mechanism, which as seen before, has an impact on the load alleviation. In addition, this delay might explain the difference in the free hinge case, since the mechanism does not have to move in this case and, consequently, the delay does not occur. Finally, the reasons behind this delay are not clear but it is likely related to hardware, as the software is the same for all of the wings. It is possible that the actuator overheated, which could cause a malfunction of the mechanism. This was observed in the preliminary phase of the experiment, in which the actuator speed was reduced due to overheating after running the experiment for an extensive period of time. In addition, it is also possible that the friction at the hinge was higher than in other wings due to a misalignment between the shaft and the bushings at the main wing, which would change the response of the wingtip.

Continuing with the analysis of the results, exciting the wings at their natural frequencies does not seem to have an impact on the alleviation performance of the FFWT. The results do not stand out even for wings B and C, which had the closest 1st bending natural frequencies to the gust frequencies used in the test. Overall, the load alleviation capabilities are similar between wings for all gust frequencies.

Next, the case with the static aerodynamic loads is considered by increasing the angle of attack to $\alpha = 5^\circ$, presented in Figure 5.7 with the respective relative peak load comparison. Similar to the case without the static aerodynamic loads, the increase in peak loads still occurs for short gusts when the FFWT is released beyond the 50% load threshold. Nevertheless, there is an important difference when considering the GLA improvement when the hinge is released before and at the instant when the gust hits the wing. The free-hinge condition allows a load alleviation similar to the $\alpha = 0^\circ$ case. However,

when the hinge is released in advance or at the 0% load threshold, the peak load can be reduced by up to 90%. To understand these results, Figure 5.8a shows a comparison of the load response with a pre-released hinge and the respective response in locked-hinge and free-hinge conditions.

As seen in subsection 4.3.2, there is a difference between the steady-state before the gust in locked-hinge condition and after the gust hits, when the hinge has already been released. When the hinge is released before the gust, the FFWT starts moving towards the second steady-state, reducing the load. Once the gust hits, the increase in load caused by the gust is compensated by the load relief caused by the movement that the FFWT starts when the hinge is released. As a result, the load barely goes above the initial steady load, leading to an almost 100% alleviation of the peak load. Therefore, releasing the wingtip at instants close to the gust hitting the wing provides better load alleviation than when the hinge is free. In addition, this optimal release time also depends on the gust frequency. For the slowest gust at 0.5 Hz, this effect can be found for both the pre-released case and the 0% release. Nevertheless, for the fast gust at 8 Hz, it can only be seen when the hinge is pre-released, hence the time range of the optimal release becomes narrower.

To conclude the peak load assessment, the trends of the results at $\alpha = 5^\circ$ are similar to those at $\alpha = 0^\circ$ when looking at the effects of the different wing designs, but wing B does not stand out as in the previous case. Even though the peak reductions seen at $\alpha = 5^\circ$ are very promising, they are conditioned to a correct timing of releasing the hinge, since releasing at high load thresholds could aggravate the peak loads instead of alleviating them. In addition, there is an important drawback that cannot be seen from the relative peak loads. Figure 5.8b shows a gust response example in which, together with a slight decrease in peak load, there is an important increase in the magnitude and persistence of the oscillation of the signal when the hinge is released. The RMS of the signals is used to study the impact of the release on the oscillations.

Figure 5.9 shows the relative RMS with respect to the locked-hinge condition at $\alpha = 0^\circ$. Contrary to what has been seen for the peak load, not only the hinge release affects the RMS but also the wing stiffness and tailoring are important. On the one hand, the RMS behaviour with respect to the hinge release is similar to that seen on the peak loads. When the hinge is free, the RMS reduction can vary between 20% and 55% depending on the wing and gust frequency. The RMS reduction decreases with the increasing release threshold and, similarly to the peak loads, the oscillations can be aggravated with respect to the locked condition when the hinge is released at 100% of the peak load. For short gusts, this can also happen at 50% release. On the other hand, it is also possible to see the differences between the wings for gusts at 1.5 Hz, 5 Hz, and 8 Hz. Wing A presents lower RMS reduction than wings B and C, while wing B presents the highest RMS reduction of all the wings. Both tailored wings, B_{WI} and B_{WO} , present lower RMS reduction than wing B, but wing B_{WO} achieves higher RMS reductions than B_{WI} . However, these trends cannot be observed for gust frequency of 0.5 Hz and the 1st bending natural frequency. For these cases, the RMS reduction is similar between wings.

When the static aerodynamic load is included in the case of $\alpha = 5^\circ$, three main remarks can be made from the results shown in Figure 5.10. First, the trends observed at $\alpha = 0^\circ$ for the different wings in the 1.5 Hz, 5 Hz, and 8 Hz gusts can still be observed in this case and, this time, they also appear for the 0.5 Hz gust and the 1st bending natural frequency. Second, in contrast to the $\alpha = 0^\circ$ case, the excitation at the natural frequency of the wings has an impact on the RMS at $\alpha = 5^\circ$. When the wings are excited at their natural frequencies, the RMS reduction when the hinge is released in advance is lower than when it is released at the 0% threshold. Last, the increase in RMS seen for hinge releases at 50% and 100% thresholds is amplified at $\alpha = 5^\circ$ and can also be seen for the 5 Hz and 8 Hz gusts when released at 0% of the peak load. For these cases, the RMS can increase with respect to the locked hinge condition by up to 150%, as in the example from Figure 5.8b.

To conclude the discussion of the results, it is shown that it is important to release the hinge instantly after the gust is detected. When the hinge is released close to the peak load, the load can not only be aggravated but also introduce significant oscillations, which tend to persist for a considerable amount of time after the gust has passed the wing. The introduction of these oscillations can be critical, as they can be considered detrimental for reasons such as fatigue of the wing structure, reduction of passenger comfort or altering the effectiveness of the control surfaces due to the unsteady loads. However, the differences seen between the different wings show that it might be possible to minimize this impact with a proper structural design. In addition, other systems, like spoilers or the wingtip tab presented by

Cheung et al. [22], could be combined to try to reduce these oscillations and further improve the GLA performance.

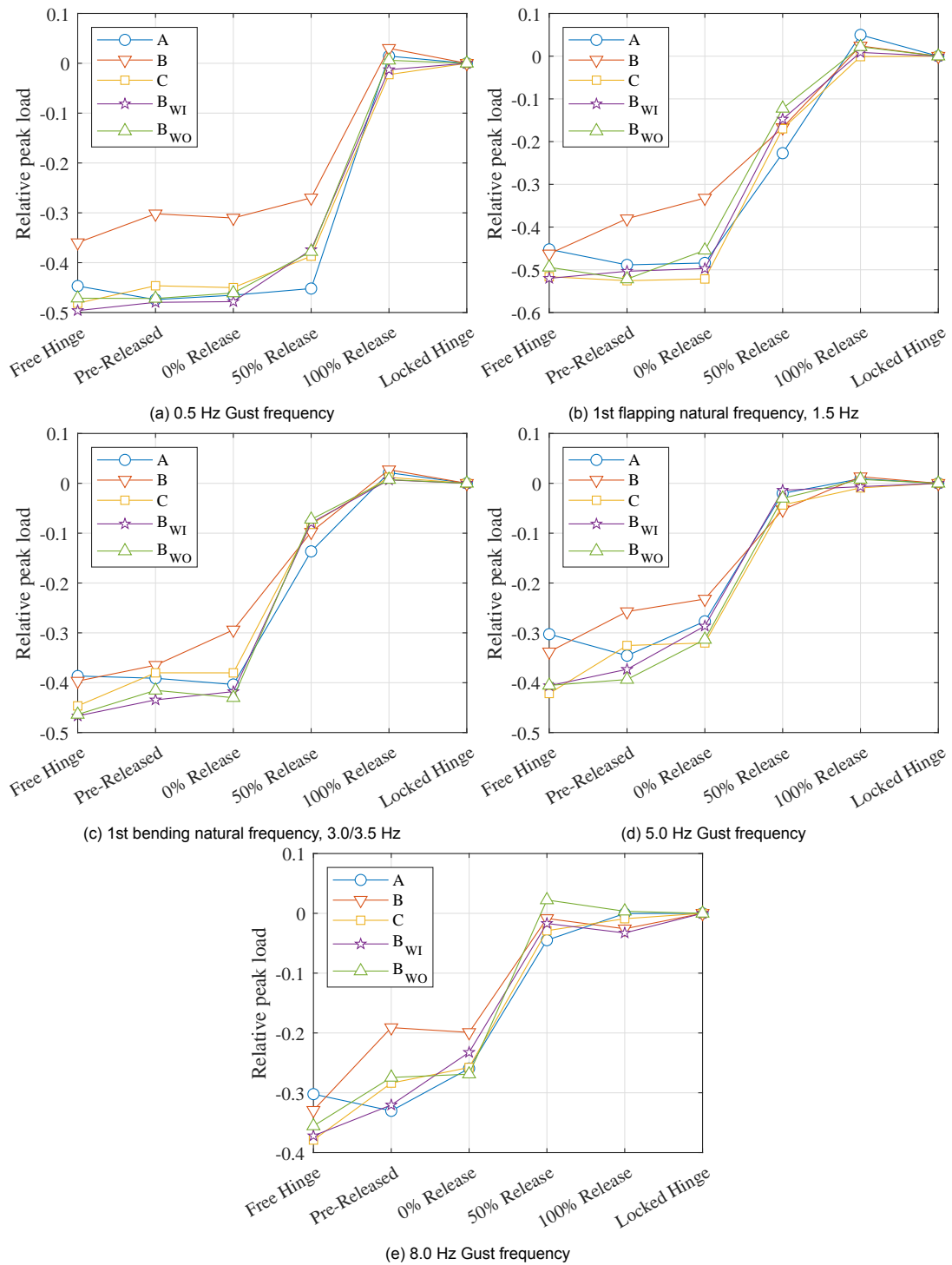


Figure 5.6: Relative peak load reduction with respect to peak load in locked hinge condition for $\alpha = 0^\circ$.

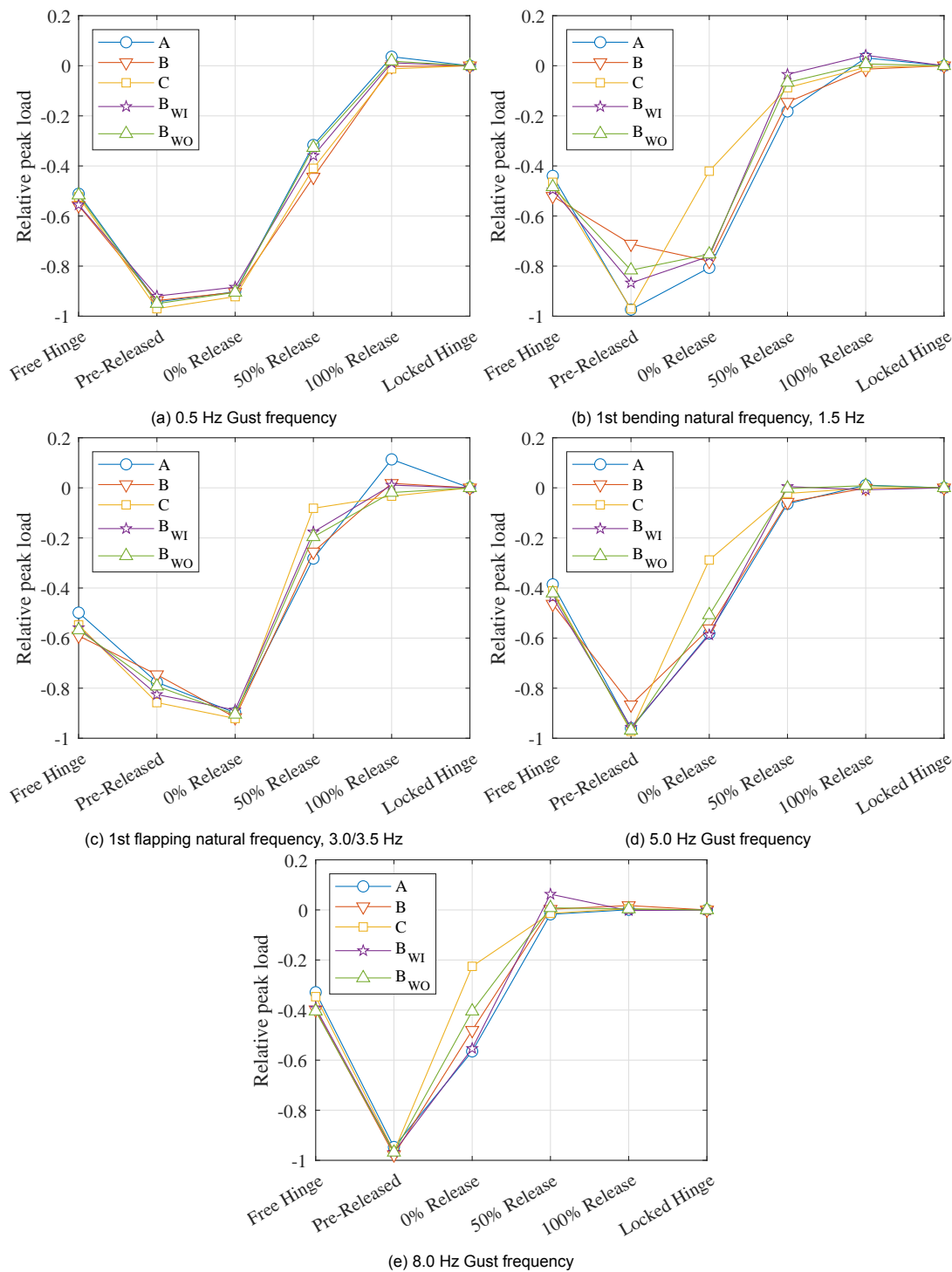


Figure 5.7: Relative peak load reduction with respect to peak load in locked hinge condition for $\alpha = 5^\circ$.

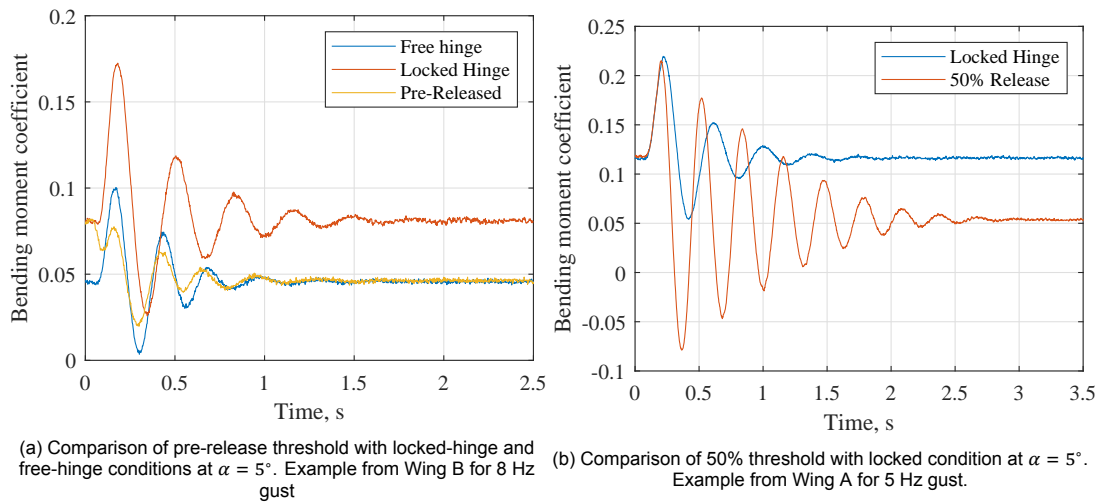


Figure 5.8: Bending moment coefficient time response examples

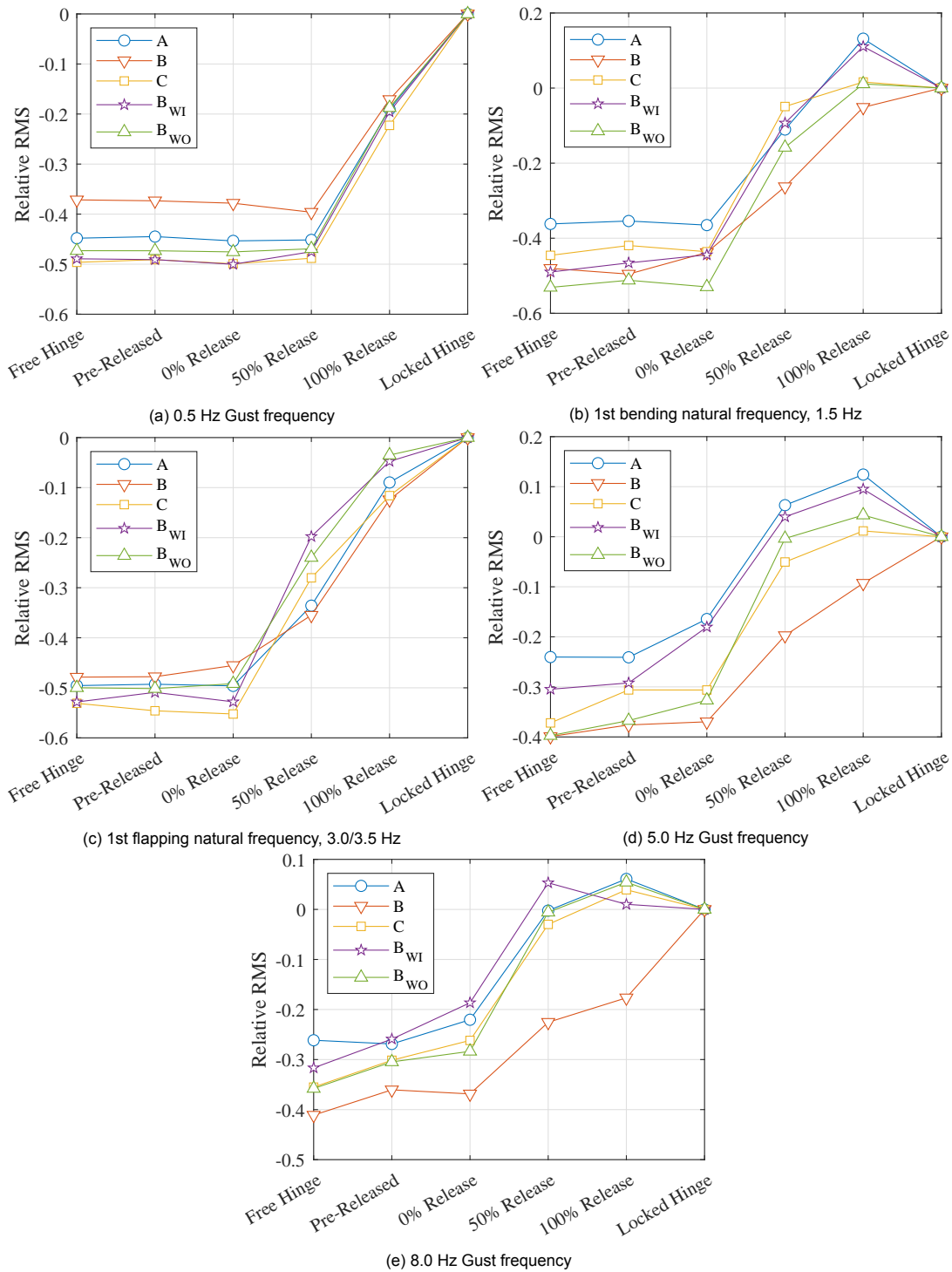


Figure 5.9: Relative RMS reduction with respect to peak load in locked hinge condition for $\alpha = 0^\circ$.

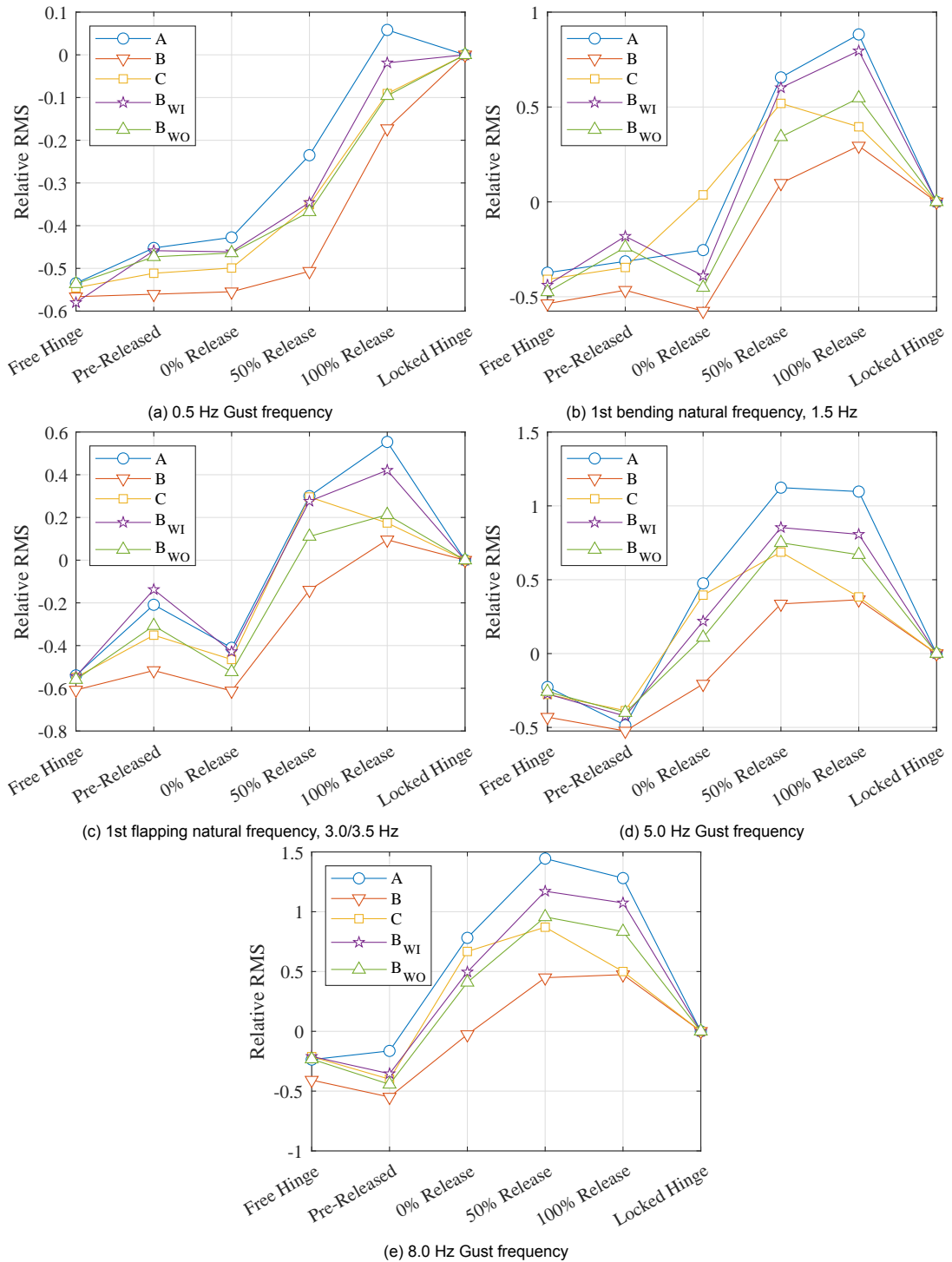


Figure 5.10: Relative RMS reduction with respect to peak load in locked hinge condition for $\alpha = 5^\circ$.

Conclusions and Recommendations

The last chapter of this thesis summarizes the contribution of this study to the state of the art of the flared folding wingtip. The conclusions will present the outcome of the experimental study and, based on these results, recommendations about future work will be given.

6.1. Conclusions

Previous studies have shown that the flared folding wingtip is an effective way to benefit from the increased aspect ratio that a folding wingtip can provide while alleviating the detrimental effects: the released wingtip can reduce the increase in root loads and alleviate the roll rate reduction caused by the wing extension. Consequently, the concept has become an object of aeroelastic research in both numerical and experimental fields. This thesis contributes to the state of the art with an aeroelastic wind tunnel experiment that studies the impact of the wing stiffness, stiffness tailoring and hinge release threshold on the gust load alleviation capabilities.

To address this objective, a wing model featuring a flared folding wingtip has been designed, manufactured and tested in the wind tunnel. The sizing of the model has been based on aeroelastic simulations of a finite element numerical model. As a result, five different wings with composite plates as main load-bearing elements have been manufactured: three wings, A, B and C, with different bending stiffness and two wings, B_{WI} and B_{WO} , with the same bending stiffness as wing B but including composite tailoring to produce wash-in and wash-out response respectively. To maximize the wash-in and wash-out response, the stacking sequence of these laminated plates has been optimized to produce the maximum bend-twist coupling while keeping the same bending stiffness as wing B. In addition, the wings included a hinge release mechanism to study the effects of releasing the hinge at different instants of the gust.

The experiments have been conducted in the W-Tunnel at the Delft University of Technology, in which different types of sensors have been used to measure the aeroelastic response of the wing: the motion of the wing has been tracked with accelerometers, the wing root bending moment has been measured with strain gauges and the rotational angle of the wingtip has been measured with a potentiometer. Furthermore, a complex real-time data acquisition system has been designed to collect the measurements and control the hinge mechanism using a feed-forward control system. Finally, the test procedure can be divided into two phases. First, a stability analysis and a modal impact test are conducted to define the test cases conducted in the second phase, those cases necessary to study the effects of the structural properties of the wing and the hinge release threshold on the gust load alleviation capabilities. In this second phase, the wings are tested in static conditions to obtain the polar curves and later tested against discrete 1-cosine gusts of different gust frequencies to study their dynamic response.

The first observation found in the experiment is that the linear model used as a sizing tool overpredicts the flutter speed by more than 40%. In addition, when studying the effect of the hinge condition

on flutter speed, a change in the flutter mechanism is found. This change would explain the unexpected effect of the tailoring on the stability of the wing: while wash-in tailoring would delay flutter in conventional wings, it promotes it when the folding wingtip is free.

Regarding the loads, the bending moment coefficient, C_B , polars show that the bending stiffness does not influence the static loads, leading to constant slope, $C_{B,\alpha}$, across the stiffness range. However, tailoring does affect the loads. The wash-out tailoring decreases $C_{B,\alpha}$ due to the bending-twist coupling, which reduces the angle of attack when bending the wing. For the wash-in, this behaviour is reversed.

Finally, there is no clear relationship between the peak load alleviation and the structural properties of the wing. Although in some test cases there is a clear difference in load alleviation, it is not consistent across the design space. On the other hand, there is a remarkable effect of the hinge release timing on the load alleviation. For statically unloaded conditions, corresponding to $\alpha = 0^\circ$, releasing the hinge before the gust hits the wing is as effective as a released hinge. However, the later it is released the worse the load alleviation becomes, even increasing the peak loads when it is released close to the peak load. When there is a static load, in the case of $\alpha = 5^\circ$, there is a significant difference between releasing the hinge on time or not. When the hinge is released in advance, the difference between the static load in the locked-hinge condition and free-hinge condition makes the wingtip start moving before the gust hits, compensating the gust load and reducing the peak load by more than 90%.

Although the dynamic release can alleviate the peak loads, it increases the oscillations of the wing, which can be considered detrimental for reasons such as fatigue of the wing structure or passenger comfort. For $\alpha = 0^\circ$ and releases close to the maximum load, these oscillations can become higher in amplitude and more persistent than if the hinge remained locked. For $\alpha = 5^\circ$, this effect is magnified, leading to increments in the RMS values of more than 100% with respect to the locked condition.

All in all, these results emphasize the importance of detecting the gusts and being able to react on time. If the aircraft can detect them in advance and release the hinge before they hit the wing, the trade-off between peak load reduction and oscillations can be positive. However, if the gust can only be detected when it hits the wing, the release and reaction time of the system needs to be small enough to avoid entering the "late release" region, for which the loads can be worsened and the oscillations doubled.

6.2. Recommendations

This last section presents the recommendations that originate from this study. The recommendation can be grouped into three types: i) practical tips to improve the manufacturing and testing procedure, ii) future work to extend the results of this thesis and iii) possible research directions derived from the observations in the numerical and experimental results.

6.2.1. Practical tips

This first set of recommendations addresses different complications seen during the design and testing procedure. In case that such a model and methodology had to be used again, these recommendations would improve and simplify the experiment.

First of all, two main remarks should be taken into account if a similar model has to be manufactured. On the one hand, the use of 3D printed parts simplified the design but introduced some imperfections on the biggest part, the main wing. These imperfections, such as deformations or cracks produced by air bubbles, can occur during the printing process but their effect can be amplified by the slender design of the printed part, introducing small differences between wings. The first and simpler proposed solution would be increasing the stiffness of the wing by thickening the leading and trailing edge beams that connect the ribs. This way, the deflections during the printing process would be reduced. Alternatively, the 3D printed part could be redesigned to make the wing modular, hence making the printed elements more compact. In essence, the 3D printing manufacturing process should be better considered during the design of the wing.

On the other hand, the material used for the composite plates was not practical to work with. The reduced ply thickness made it difficult to handle and, given the desired plate thickness, a large number

of layers was required. These two facts led to a long lamination process that could be avoided using a thicker material. In this study, the selection of the material was based on the ability to control the stiffness properties of the tailored wings that the thin layers gave. For studies where this control is not necessary, an alternative material would speed up the lamination process.

Secondly, the original concept of the data acquisition system required a complex combination of SCADAS, cRIO and Ethercat communication. However, this complexity made the system unreliable for the experiment and required an on-site modification to an alternative approach. The alternative system proved to work but was still limited by the original selection of hardware. For future experiments using the feed-forward control, the cRIO could be removed and conduct both the data acquisition and signal processing using the SCADAS. Therefore, the Ethercat communication would not be necessary, the system would become simpler and the sampling rates could be increased drastically.

Last, the accelerometers could not be used during the gust excitation cases because of the noise introduced by the mechanism. However, the accelerometers could be moved far from the mechanism to avoid the vibrations so the motion of the main wing could be studied. Alternatively, a different methodology could be used, such as Particle Tracking Velocimetry or trailing edge tracking using image processing on video recordings.

6.2.2. Future work

The next recommendations address the continuation of this study. Given the differences between numerical and experimental results, future work should be directed towards solving the modelling uncertainties seen during the experiment.

On the one hand, the modal analysis showed that it is necessary to update the structural properties of the numerical model to improve the quantitative agreement with the experiments. Therefore, the immediate continuation of this study should be ground vibration tests of the wings to correlate the numerical model with the actual wings. Then, the structural properties of the simulation could be updated to understand to what extent does the difference between the numerical model and experimental model affects the predictions of the solver used in this study.

On the other hand, alternative solvers need to be investigated to account for the nonlinearities caused by the aerodynamics of the flared folding wingtip. For the gust response simulations, the results were limited to small wingtip deflections due to the aerodynamic loads not following the structural deformations. Therefore a solver capable of adapting the aerodynamic model to the large deflections of the wingtip would improve the predictions. For the flutter analysis, the drop in critical speed and the limit cycle oscillations seen in the experiment show the complexity of the dynamic behaviour of the system. Therefore, it is necessary to account for these nonlinearities to improve the prediction of flutter speed, which can be achieved with a nonlinear solver.

Finally, it has been seen that the hinge release must be optimised to avoid inducing oscillations. Given the impact that the delays in the actuation process have, the optimal release instant can be posed as a multi-objective optimisation problem to maximise the load alleviation while minimising the induced oscillations. Alternatively, since the release instant is constrained by the capabilities of detecting the gusts and providing a fast reaction, the problem can be addressed from a different perspective and assess the reaction time that the mechanism has to achieve. Later, this reaction time could be compared to the reaction times that current gust detection systems can provide, as it might not be possible to benefit from the hinge release with the capabilities of current gust detection technologies.

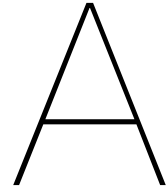
6.2.3. New research directions

To conclude this study, new research directions based on the obtained results are summarised. First, the already mentioned complexity of the system presents the necessity to understand the dynamic behaviour of the folding wingtip and how it interacts with the main wing. The dynamic response of the wing in the free-hinge condition can lead to surprising results both in terms of aeroelastic stability margins as well as the aeroelastic response and gust load alleviation performance. Furthermore, the unexpected behaviour of the aeroelastic tailoring when combined with the folding wingtip shows that the design rules applied for conventional wings might not be applicable for this concept and require

further investigation.

Second, the increased persistence of the oscillations introduces the necessity of investigating control means to reduce them. One possible solution already studied in the literature would be the implementation of a control surface on the folding wingtip, which would increase the complexity of the design but can provide further load alleviation and a means to control de wingtip.

Last, the folding wingtip could be combined with other gust load alleviation control systems, such as ailerons or spoilers, to reduce the oscillations and further reduce the peak loads. However, the control laws used for each system are not necessarily compatible with those of other systems, hence combined control laws might be necessary. If they are not compatible, a trade-off study between the different options would be required.



Set Up of Real-time Measurements

As presented in section 4.2, the approach taken in these experiments requires real-time measurement. This appendix presents a guide to set up the real-time system using EtherCAT communication between the data acquisition system and the control module. This guide gathers the information given by National Instruments and Siemens either in their online support pages or in direct communication with their support team. For the first case, references will be given; for the second, the files are collected in “Eth_files.zip”, which can be obtained under request from Jurij Sodja. The first section presents the requirements to carry out the real-time measurements. Afterwards, the procedure to set up the different systems is presented. The last section includes some problems that can be found during the procedure and how to solve them.

A.1. Requirements

The hardware used for this system is:

- **National Instruments cRIO-9074:** chassis that acts as Ethercat master. The scan rate, the rate at which the chassis sends/receives information from other elements of the network, is limited by hardware to 1 kHz. However, the different modules of the chassis can be configured in FPGA mode and achieve frequencies up to 1 MHz. Thus, the control signal can be sent at 1 MHz but the setpoint, coming from another element of the network, will be modified at 1 kHz. Depending on the application, this might not be enough but it is always possible to replace the chassis with a faster alternative ¹.
- **Siemens SCADAS Mobile:** DAQ system that acts as EtherCAT slave. It offers a compact solution for data acquisition. Its VB8-III-RT module allows real-time measurements and supports signal conditioning for a wide range of configurations, including an internal bridge that can be automatically calibrated from the TestLab interface. As explained in the next section, for EtherCAT communication, the sampling rate has to be set up at 102 kHz but will be limited by the 1kHz scan frequency previously mentioned.

The software requirements are presented in Table A.1. If they are not installed during the first installation, the links to the respective downloads can be found in the EtherCAT setup tutorial, which has been used as a reference for the configuration of the National Instruments part of the network ².

¹Building a Real-Time System With NI Hardware and Software. National Instruments - Support, 2021. URL <https://www.ni.com/nl-nl/innovations/white-papers/06/building-a-real-time-system-with-ni-hardware-and-software.html>. Last accessed: 10 August 2021.

²Setting Up EtherCAT on NI Programmable Automation Controllers. National Instruments - Support, 2020. URL <https://knowledge.ni.com/KnowledgeArticleDetails?id=kA03q000000YHbbCAG&l=nl-NL>. Last accessed: 10 August 2021.

Table A.1: Software requirements for real-time system setup

Provider	Software	Description
National Instruments	LabVIEW	Core installation
	LabVIEW FPGA	Module for FPGA programming (up to 1 MHz)
	LabVIEW Real-Time	Module for real-time programming (up to 1 kHz)
	NI-RIO driver	Drivers for the cRIO chassis
	Industrial communications for EtherCAT driver	Drivers for EtherCAT communication
Siemens	Simcenter TestLab with Simcenter Turbine Testing	Software to set up and run Siemens hardware. "Simcenter Turbine Testing" is the module required to run in EtherCAT mode. It is included in the general installation

As a final note, this procedure has been tested in LabVIEW 18.5 and running on a 32-bit version. For newer versions, it is possible that not all the modules can run on 64-bit versions, as they are released months later. Furthermore, some modules might not be available in the student license. For the complete license, contact the technicians at the aircraft hall.

A.2. Procedure

The procedure can be divided into three subsections: setting up TestLab, setting up LabVIEW and running a program.

A.2.1. Setting up TestLab

The procedure explained in this subsection can be found in "ESO64_configuration.pdf" inside "Eth_files.zip".

To run real-time measurements, the ESO64 module, presented in Figure A.1, is required. This module is an EtherCAT slave that can send information of up to 64 channels to the network. It requires an external EtherCAT master, which is not supported by Siemens. Thus, the cRIO is used as EtherCAT master. The module is only supported by "Simcenter Turbine Testing" and can only use real-time (-RT) modules, like the VB8-III-RT previously mentioned.



Figure A.1: Representation of the ESO64 card

Before starting TestLab and connecting the SCADAS to the computer, it is necessary to modify some PC settings:

- "TRMConfig.xml" file: Includes the user's computer in the SCADAS configuration to start recording data.
 1. Copy the file from:
 - "C:\ProgramFiles(x86)\Simcenter\TestLabXX\central\Configuration"
 - To:
 - "C:\Simcenter\UserConfiguration\[user]\TestLabXX\Configuration".
 2. Open the file in a txt editor and modify Lines 22 and 26 as shown in Figure A.2.

- Modify user running “RemTRM”, as shown in Figure A.3.
 1. Go to Component services.
 2. Select: “Computer” → “My Computer” → “DCOM Config”
 3. Locate “RemTRM”
 4. Right-click on it and select “Properties”
 5. Select the “Identity” tab and set it to “Interactive User”
 6. Press “Apply” and “OK”
- “TurbineTesting” folder:
 - (1.) Create a folder named “TurbineTesting” on the C: directory
 - (2.) Share the folder with all the users on the PC following the procedure in Figure A.4:
 - (a) Right-click, select “Properties”.
 - (b) In the “Sharing” tab, click on “Advanced Sharing” (Admin rights)
 - (c) Toggle the “Share this folder”
 - (d) Click on “Permissions”
 - (e) Allow all the Permissions (Full Control, Change and Read)
 - (f) “Apply” and “OK”

Now, TestLab could be prepared to run. Connect the SCADAS to the PC using the SYSCON card and an ethernet cable ³. Turn it on and open the “Turbine Test Recording Manager” application, the only one that supports EtherCAT communication. Then, create a new project and save it. Afterwards, follow the steps presented in Figure A.5:

1. Select “Recording Setup” workbook
2. Select the “Recording system”, which matches with the modification in the “TRMConfig.xml” file.
3. Click “Start Recording System”

After loading, the “HighSpeedTimeDataRecordingStandard” application should open. In this application:

1. Load the “EtherCAT” add-in, as shown in Figure A.6a.
2. Configure the “Channel setup”. This is not exclusive to the EtherCAT communication, this tab allows configuring the channels to be measured.
3. Move to the “Acquisition Setup” tab and set the “ADC Bandwidth” to 102400 Hz, as in Figure A.6b. This is necessary for the EtherCAT communication and will cause an error if not configured as such (see subsection A.3.1).
4. Change to the “EtherCAT” tab, which should be available after Step 1.
5. Map the “Input Channels” with the EtherCAT channels, as shown in Figure A.7a.
6. If a Channel is not used, select “Not mapped”.
7. The channel information can be exported by clicking “Export Transducer Data...”, as shown in Figure A.7b.
8. Select the “EtherCAT Low Pass filter”
9. Now the system could be released by clicking the Play button. This action releases the ESO64 and blocks the acquisition settings to prevent interference with the real-time data transfer.

³What's in the box? Getting Started with Simcenter SCADAS. Siemens - Community Support, 2020. URL <https://community.sw.siemens.com/s/article/What-s-in-the-box-Unpacking-Simcenter-SCADAS-hardware>. Last accessed: 10 August 2021.

TRMConfig.xml

Line 22:
 <EthercatMode Value = "Yes"/>

Line 26:
 <Item Name="pcname" IP="pcname" Port = "600" TDFName = "a" SmartMoveTDFPort = "2222" MulticastAdapter = "192.168.10.10"/>

```

22      <EthercatMode Value = "Yes"/>
23      <Multicast Value = "Yes" MulticastAddress = "239.10.10.10" Multicas
24      </Config>
25      <Recording>
26      <Item Name="GBLONUP1UFX1" IP="GBLONUP1UFX1" Port = "600" TDFNam
27      <Item Name="RecordingSystem2" IP="RecordingSystem2" Port = "601"
28      <Item Name="RecordingSystem3" IP="RecordingSystem3" Port = "602"
  
```

To find the "pcname" go to your PC Settings and find the Device name:

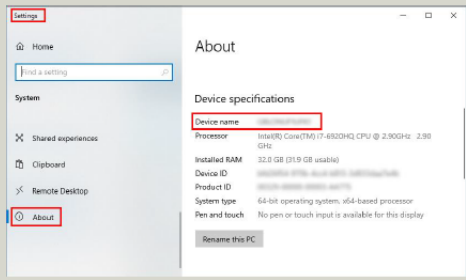
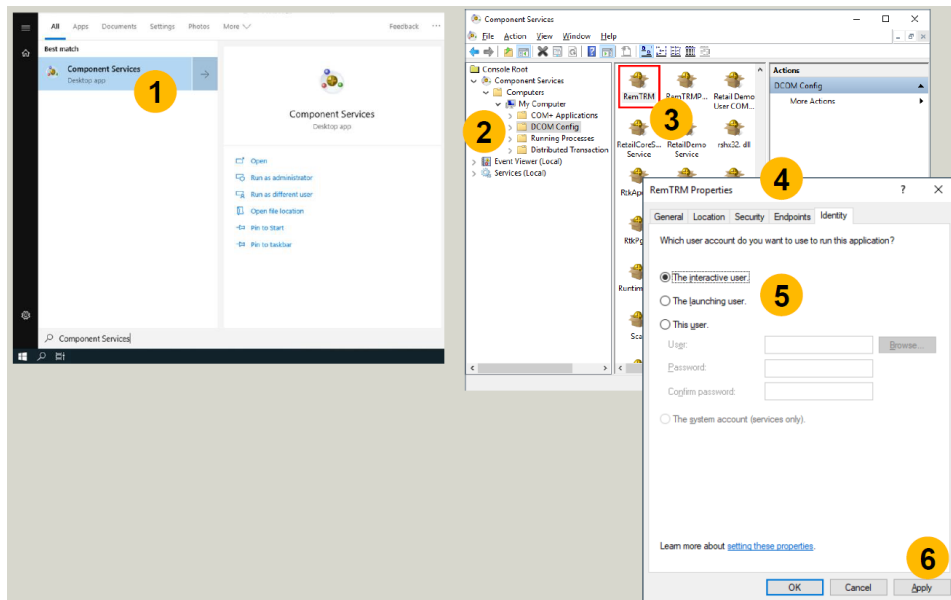


Figure A.2: Modifications required on the "TRMConfig.xml" file



1. Search for Component Services in Windows Start menu.
2. Open Component Services console.
3. Right-click on RemTRM in the console tree.
4. Open RemTRM Properties dialog box.
5. Select 'The interactive user' as the user account.
6. Click 'Apply' to save the configuration.

Figure A.3: Instructions to modify "RemTRM" configuration

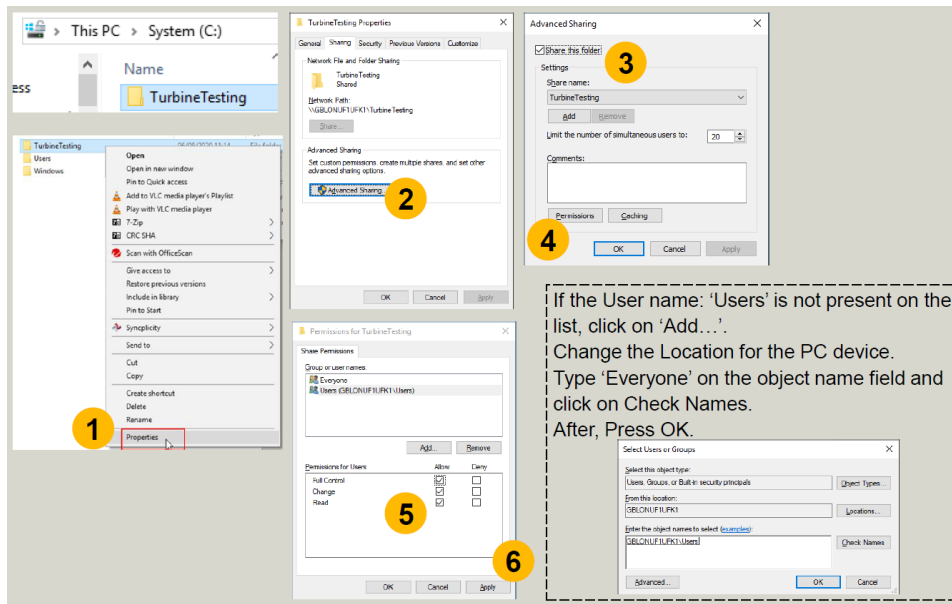


Figure A.4: Instructions to share the “TurbineTesting” folder

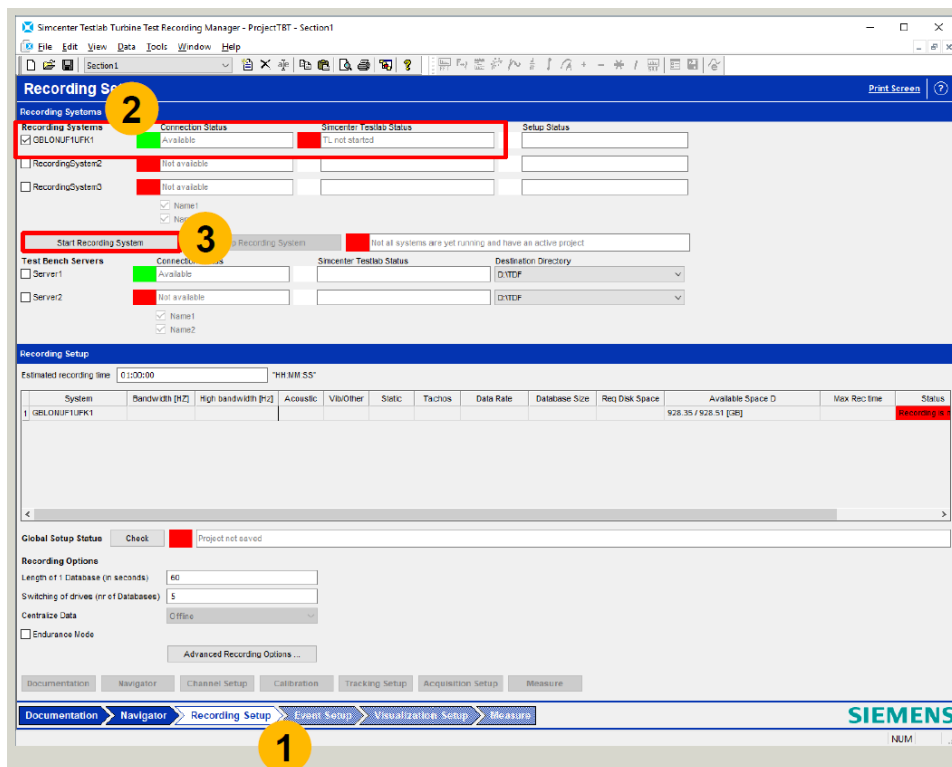
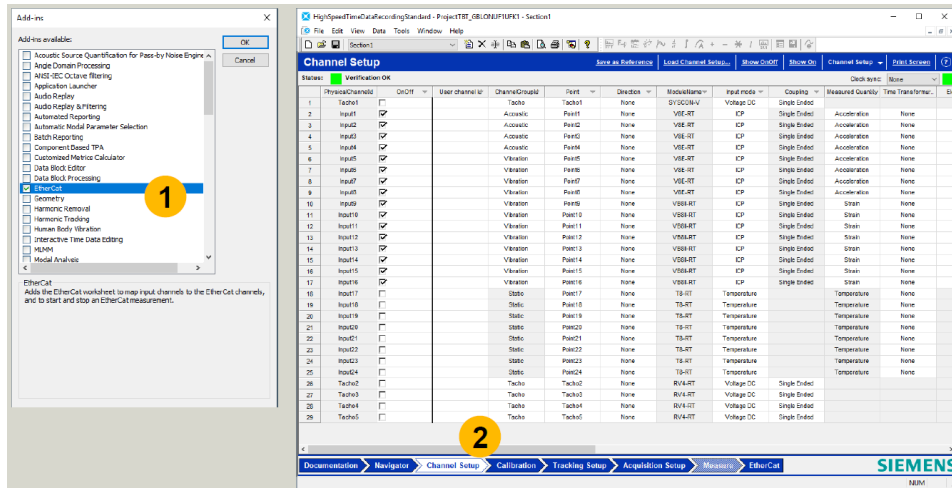
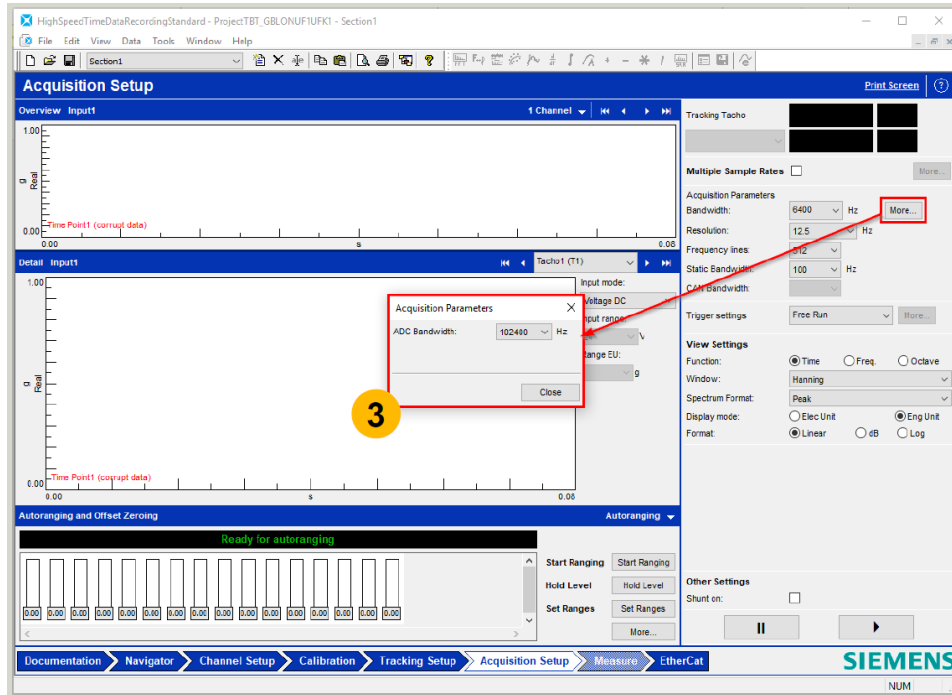


Figure A.5: Instructions to follow in the “Turbine Test Recording Manager” application

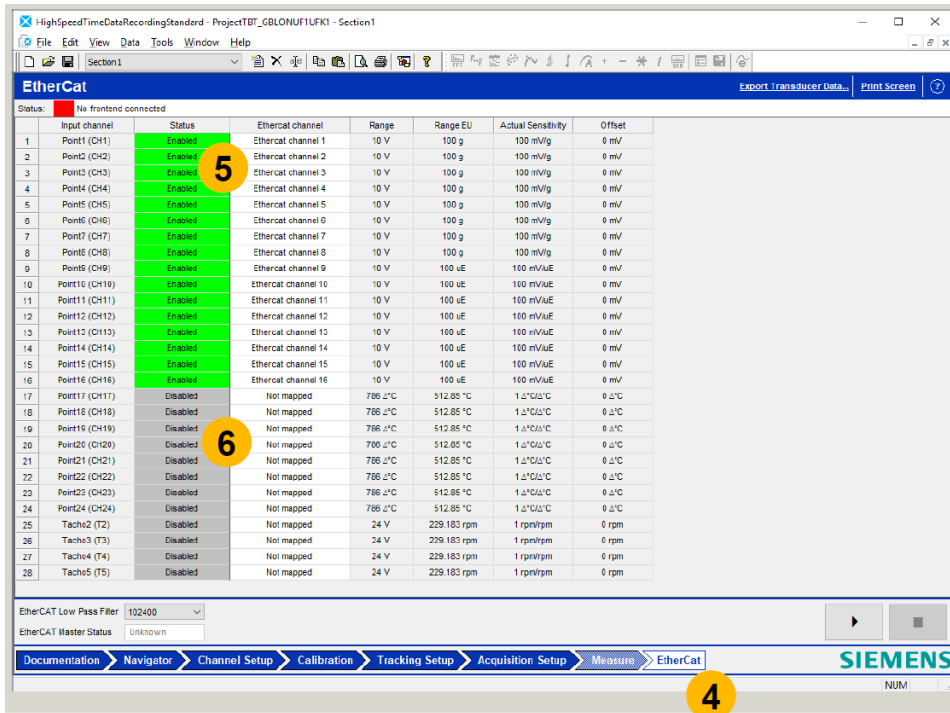


(a) Steps 1 and 2

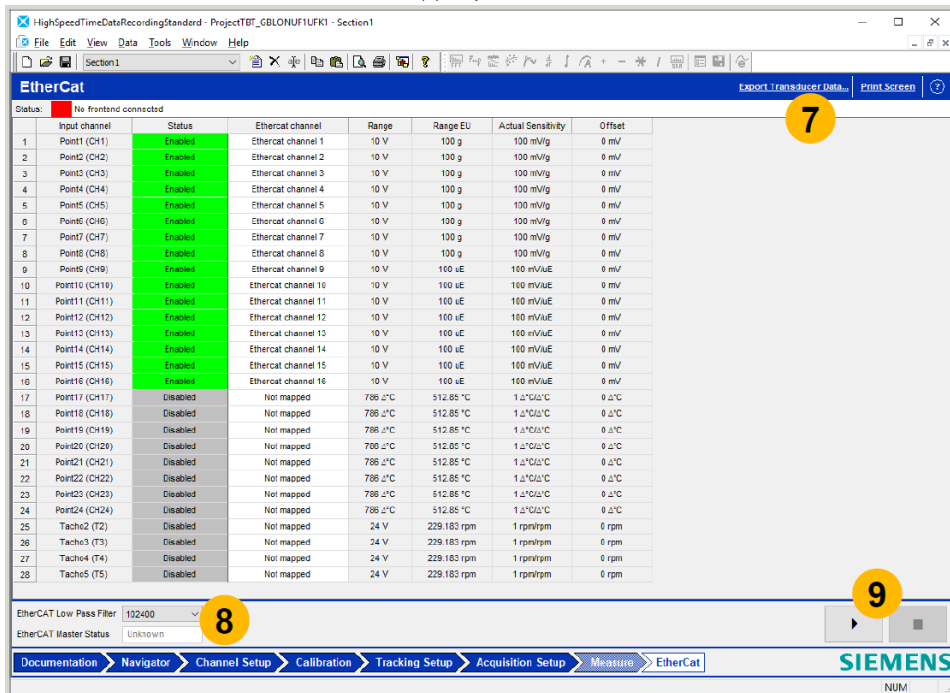


(b) Step3

Figure A.6: Instructions in the “HighSpeedTimeDataRecordingStandard”, steps 1 to 3



(a) Steps 4 to 6



(b) Steps 7 to 9

Figure A.7: Instructions in the “HighSpeedTimeDataRecordingStandard”, steps 4 to 9

A.2.2. Setting up LabVIEW

This part of the guide can be found in the National Instruments support articles ⁴.

Before start programming in LabVIEW, the cRIO Ethernet ports have to be configured to allow EtherCAT communication:

1. Use an Ethernet cable to connect cRIO-9074 Ethernet Port 1 to the same network as the host PC.
2. Launch the NI Measurement & Automation Explorer (MAX) configuration utility from “Start → Programs → National Instruments → Measurement & Automation”. Double-click on “Remote Systems” in the Configuration panel tree on the left to auto-discover the cRIO-9074 on the network, and click on the CompactRIO controller.
3. Change the name of the master controller (Optional) and select “Obtain IP address from DHCP server” under “IP Settings”, as presented in Figure A.8. Once modified, reboot the cRIO. (To use a static IP address, see the related support article ⁵.)
4. To install the software on the real-time master controller, expand the cRIO-9074 under “Remote Systems”. Right-click “Software” and select “Add/Remove Software”, as shown in Figure A.9.
5. Install the recommended software set—NI-RIO driver software with the NI Scan Engine as well as NI-Industrial Communications for EtherCAT driver software—onto the CompactRIO controller. Notice that if one of the components does not appear in the software list, it has not been properly installed on the computer. Go back to section A.1 and install the required software.
6. Once the controller has rebooted, find the CompactRIO controller under “Remote Systems” again. Click on “Advanced Ethernet Settings” in the lower right-hand corner.
7. Select cRIO-9074 Ethernet Port 2 (the MAC address that is not primary). Then select “EtherCAT” in the pull-down box under “Mode” and click “OK”, as shown in Figure A.10.

Next, a LabVIEW project can be created:

1. Launch LabVIEW from “Start → Programs → National Instruments → LabVIEW X.X → LabVIEW”. Click on “Empty Project”.
2. Right-click on “Project” and select “New → Targets and Devices”.
3. In the “Add Targets and Devices” dialog window, select “Existing target or device” and expand the category “Real-Time CompactRIO” to auto-discover the EtherCAT master on the host PC’s subnet. Select the cRIO-9074 and click “OK”. If the controller is not connected, it can be added by selecting “New target or device” and defining the IP address later.
4. In the LabVIEW Project window, right-click on the cRIO-9074 and select “New → Targets and Devices”, as in Figure A.11.
5. Select the available EtherCAT master port and click “OK”. The “Scan Slaves” dialog window appears, presented in Figure A.12. The first option Scan Interface auto-discovers any slaves connected to the controller. Click “OK”. The LabVIEW Project now lists each slave device, its I/O modules, and the physical I/O on each module (called I/O variables).

Since the EtherCAT slave, the SCADAS, is from a third party, LabVIEW will not detect it. To do so, it is first necessary to import the configuration file:

⁴Setting Up EtherCAT on NI Programmable Automation Controllers. National Instruments - Support, 2020. URL <https://knowledge.ni.com/KnowledgeArticleDetails?id=kA03q000000YHbbCAG&l=n1-NL>. Last accessed: 10 August 2021.

⁵Configure CompactRIO With a Static IP Address. National Instruments - Support, 2021. URL <https://www.ni.com/getting-started/set-up-hardware/compactrio/static-ip>. Last accessed: 10 August 2021.

1. Locate the EtherCAT XML Device Description File: "ESO64.xml". This file can be found in "File.zip"
2. In the LabVIEW project, right-click the "EtherCAT master" node and select "Utilities → Import Device Profiles" to display the "Import Device Profile" dialog box.
3. Click the "File Browse" button to select the device profile(s) in either of the following ways.
 - Select a file and click "Open" to import a device profile.
 - Open a folder and click "Current Folder" to import all device profiles under the folder.
4. After selecting the device profiles, the file import results can be seen. The file is imported successfully if "Import Result" reads "Succeed". Otherwise, the file is not imported due to an invalid format or other reasons.
5. Click "Close" to exit the dialog.
6. LabVIEW has to reboot to use the newly imported device profile.

Finally, to detect the SCADAS:

1. In the LabVIEW project, right-click the "EtherCAT master" node and select "New → Targets and Devices".
2. If the SCADAS is connected to the Ethernet port 2 of the cRIO (see the connection in next subsection), LabVIEW will automatically detect the ESO64 card. Otherwise, as with the cRIO, the ESO64 can be added offline and introduce the IP address later.

In Figure A.13, the final look of the LabVIEW project is presented. Under the cRIO node, there is the "Chassis" node, under which all the modules installed on the chassis can be found, and the "EtherCAT Master" node, under which the ESO64 and its 64 channels can be found (and other slaves, if connected).

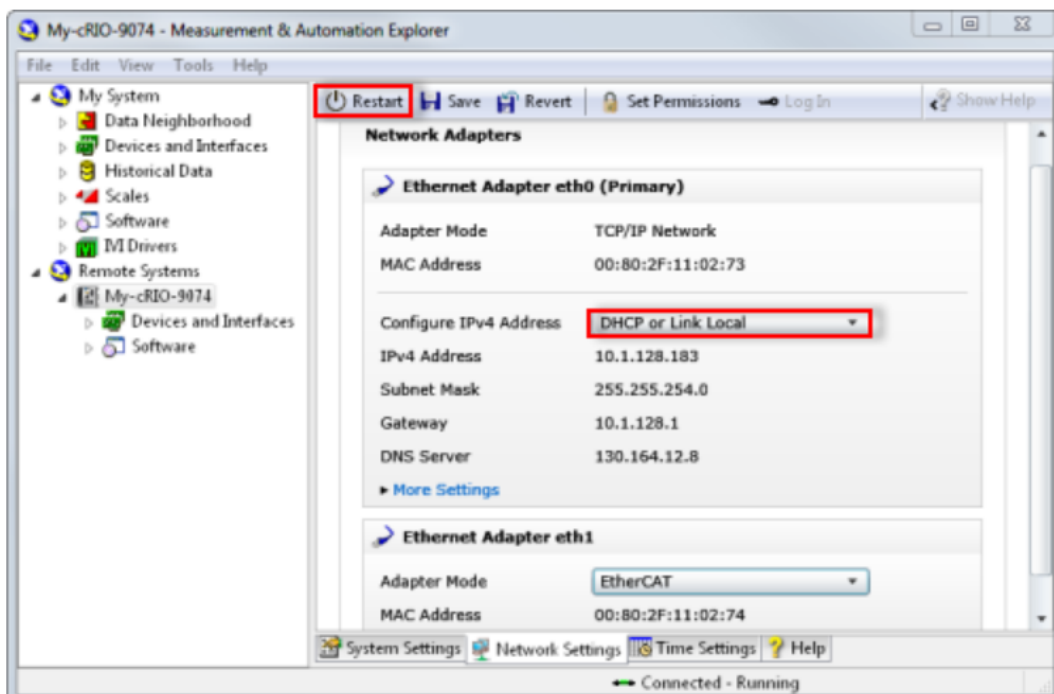


Figure A.8: Setting the IP Address for the Real-Time Controller.

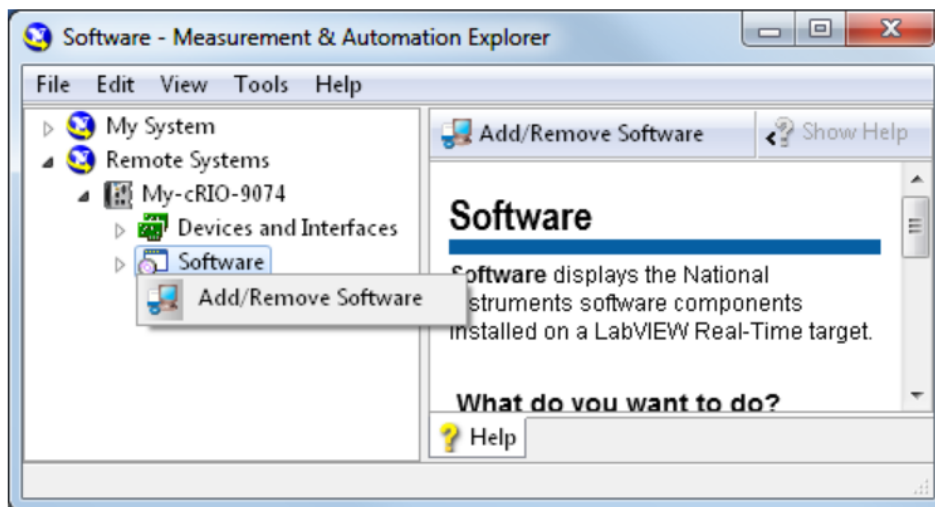


Figure A.9: Installing Software on the Real-Time Controller.

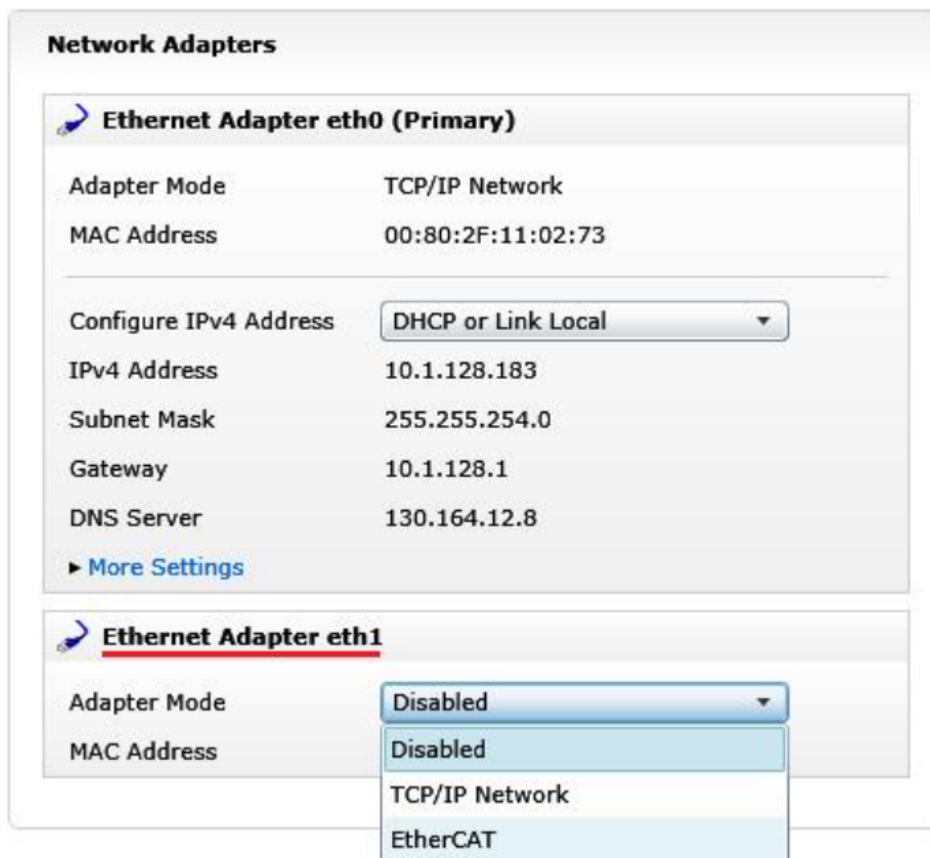


Figure A.10: Selecting EtherCAT Mode for the Ethernet Port of the Real-Time Controller.

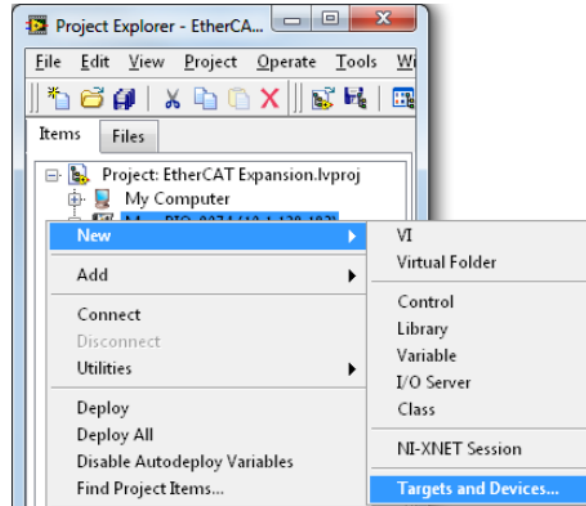


Figure A.11: Using LabVIEW to discover controllers connected to the network.



Figure A.12: Selecting the EtherCAT Master Port on the Real-Time Controller.

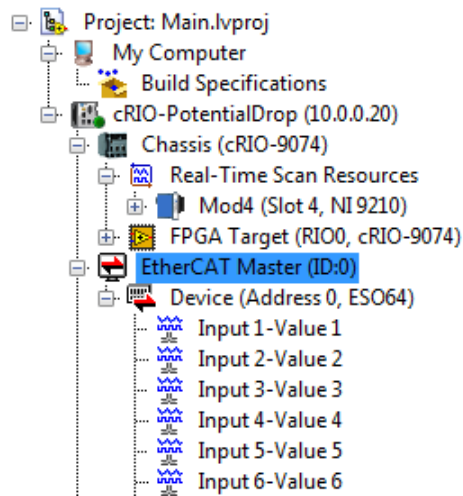


Figure A.13: Final look of the LabVIEW project after configuring the EtherCAT network.

A.2.3. Running a program

Once LabVIEW and TestLab have been configured, the system can already run programs.

The different elements of the network should be connected as in Figure A.14. Notice then that it is necessary to have 2 ethernet ports in the host computer. It is possible to disconnect the SCADAS from the computer once the EtherCAT communication is running, as the system is thought to be used independently from the computer. This way, only one port would be needed, as the cRIO could be connected after configuring the SCADAS. However, it is not recommended, as, sometimes, the TestLab interface freezes. When this happens, it is necessary to reboot the computer.

Once the connection is done, the program should be saved under the Master node and run directly, as the example in Figure A.15. To read variables from the SCADAS, drag and drop the channels from the ESO64 node to the program, as presented in Figure A.16.

As a final note, the EtherCAT communication presented in this document sends the electrical signal instead of the converted signal. Siemens presents its conversion functions in “EtherCAT data description.pdf”, which can be found in “Eth_files.zip”. The different values within Equation A.1 to Equation A.3 are explained in the previously mentioned file and can be found in TestLab, so the conversion can be included in the LabVIEW program and avoid extra work in post-processing the data.

$$\text{Scale factor} = \frac{\text{Polarity}}{\text{Actual Sensitivity} \cdot \text{Pregain1} \cdot \text{Pregain2}} \quad (\text{A.1})$$

$$\text{Constant} = \frac{\text{Offset} \cdot \text{Polarity}}{\text{Actual Sensitivity}} \quad (\text{A.2})$$

$$\text{Engineering Value} = \text{Electrical Value} \cdot \text{Scale factor} - \text{Constant} \quad (\text{A.3})$$

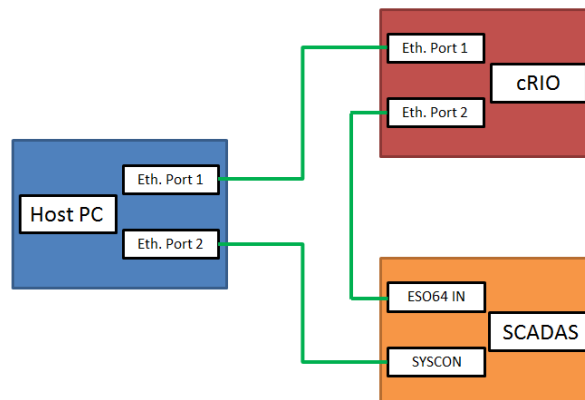


Figure A.14: Sketch of connections between elements in the network.

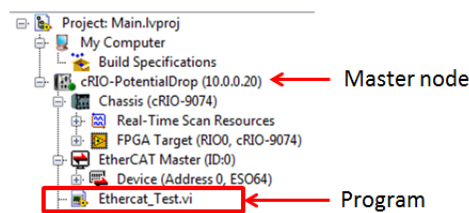


Figure A.15: The program to run should be saved under the chassis node (EtherCAT Master).

A.3. Troubleshooting

A.3.1. TestLab

- If the “Status” shows the message “AdcBandwidht needs to be set to 102400 Hz”, as in Figure A.17, the ADC bandwidth was not set up correctly. Go back to the “Acquisition Setup” tab



Figure A.16: Dragging I/O variables from the LabVIEW project to the block diagram

and modify the frequency.

- If a channel is not enabled in the “Channel Setup” tab and it is mapped in the “Ethercat channel” column of the “Ethercat” tab, an “Invalid mapping:...” message will appear, as in Figure A.18. Change the “Ethercat channel” of the “Disabled” channel to “Not mapped”.
- Some other known errors related to IP addresses and their solution can be found in Siemens community articles ⁶.

EtherCat				
Status: ■ AdcBandwidth needs to be set to 102400 Hz				
	Input channel	Status	Ethercat channel	Range
1	Point1 (CH1)	Enabled	Ethercat channel 1	10 V
2	Point2 (CH2)	Enabled	Ethercat channel 2	10 V
3	Point3 (CH3)	Disabled	Ethercat channel 3	0.1 V

Figure A.17: Error message when the ADC bandwidth is not set up correctly

EtherCat				
Status: ■ Invalid mapping: Channel input3 is mapped but not enabled				
	Input channel	Status	Ethercat channel	
1	Point1 (CH1)	Enabled	Ethercat channel 1	
2	Point2 (CH2)	Enabled	Ethercat channel 2	
3	Point3 (CH3)	Disabled	Ethercat channel 3	
4	Point4 (CH4)	Disabled	Ethercat channel 4	

Figure A.18: Error message when mapping a disabled channel

A.3.2. LabVIEW

- When detecting slave devices, ESO64 might not appear in the slaves list. This happens when the configuration file “ESO64.xml” has not been imported. Import the file as explained in subsection A.2.2 and reboot LabVIEW. Afterwards, the device should appear in the list. Notice that, to be detected automatically, the ESO64 has to be connected to the cRIO, as shown in Figure A.14. Otherwise, it can be added manually and configure the IP address once it is connected.

⁶What’s in the box? Getting Started with Simcenter SCADAS. Siemens - Community Support, 2020. URL <https://community.sw.siemens.com/s/article/What-s-in-the-box-Unpacking-Simcenter-SCADAS-hardware>. Last accessed: 10 August 2021.

A.3.3. Running real-time program

- If the program runs before starting the EtherCAT communication in TestLab, LabVIEW will deploy the ESO64 channels but won't read values, even if the EtherCAT connection is established afterwards. To solve this problem, stop the program and redeploy the "EtherCAT Master": right-click and "Undeploy", ensure that the SCADAS is connected and sending information (see section), and right-click and "Deploy".
- For the data acquisition, it is necessary to save files on the computer. Since the program is running in the cRIO, the file is saved there instead of the computer. To save the files on the computer, a parallel program can run on the computer. This program can read a global variable, updated by the cRIO program.
- The EtherCAT communication runs at the same frequency as the Scan Engine in the cRIO. For the 9074, the real-time module is then limited to 1 kHz. If the control loop is included in the same program, the control signal will be limited to this frequency as well. However, it is possible to separate the data acquisition from the control signals so they can run at higher frequencies. The control program can be written in FPGA programming (I/O modules programmed at hardware level), run parallel to the data acquisition and communicate with it making use of global variables within the project. The maximum frequency with FPGA is 1 MHz, although this mode adds some problems:
 - FPGA programming requires compiling the program in the cRIO and program the different modules at the hardware level. This is automatically done by LabVIEW when running the program but takes several minutes to compile, which is not desirable when debugging.
 - Although the control program can run at 1 MHz, the setpoint, which is read from the network, will still be updated at 1 kHz. For some applications, this might not be enough.

B

Ground Vibration Test

As seen in the main body of the thesis, the numerical model requires an update of the physical properties of the wing. Therefore, GVTs have been carried out to obtain the modal properties and later update the model to match the experimental results. However, the correlation and update of the model has been considered out of the scope of the thesis and will be conducted in future work. Therefore, since the GVTs have already been carried out, the procedure and setup are presented in this appendix.

B.1. Methodology

A GVT is an experimental procedure that uses modal analysis to obtain the modal model of a structure [33], which assumes a linear time-invariant dynamic system. Therefore, the dynamic response of this system can be described as a combination of its natural modes, which are determined by the mass, stiffness and damping of the structure. For a detailed definition of modal analysis and its different applications, please refer to He et al. [34].

Focusing on the experimental application, the objective is to obtain the modal properties of a structure which can be done by establishing the relationship between excitation and the vibrations it produces. This relationship is known as the frequency response function (FRF) and can be obtained by exciting the structure and measuring the vibrations at one or more points of the structure, which can be done using different methodologies.

In subsection 4.5.2, the modal impact test using a modal hammer to introduce the excitation has been presented. In this case, the vibrations are captured with the accelerometers and the potentiometer, which describe the tip and wingtip motion. However, as seen in the results, the information that can be extracted from this method is limited. In addition, the introduction of the sensors adds mass to the structure, which will modify the modal properties. Therefore, it is desirable to use alternative methods that are non-intrusive.

For this reason, these GVTs have been conducted using a scanning laser doppler vibrometer (SLDV), which uses a laser to measure the vibrations instead of accelerometers. In this case, the accelerometers could not be removed from the structure, as they are used for data acquisition during the test, hence the modification of the mass properties cannot be avoided. Nevertheless, this alternative system allows introducing as many measurement points as desired, improving the mode shapes that can be extracted from the test.

B.2. Setup

The setup used for these tests is that presented in Figure B.1. The main elements of the setup are the following:

- **Test rig:** it is the same test rig that is used in the calibration of the strain gauges but changing

the position of the wing to facilitate the measurements of the laser system.

- **SLDV system:** the system is a Polytec PSV-500¹, which incorporates the laser head to conduct the measurements and the control system to perform the test and process the data.
- **Impact hammer:** it is an OMS vImpact Hammer², which is an automatic impact hammer with a load cell at the tip, allowing a precise and repeatable impact. The impact point is the same for every wing and coincides with one of the measurement points, detailed in red in the grid of Figure B.2.
- **Wing model:** wing presented in section 4.1 and tested in the locked hinge configuration.

B.3. Procedure

The procedure of the test can be summarised in the following steps:

1. **Calibration:** both the impact hammer and the SLDV need to be calibrated before testing. In the case of the laser, its intensity has to be calibrated to correctly measure the distance to the measurement point. For the hammer, its position needs to be corrected to avoid double impacts when exciting the wing and do not overload the load cell.
2. **Mesh:** it is necessary to define the points where the measurements will be taken, hence a mesh is generated. Given the simplicity of the wing geometry, the mesh can reduce the wing to a total of 24 grid points, half on the leading edge and the other half on the trailing edge. From these 24 nodes, 6 define the wingtip and 18 define the main wing, as seen in Figure B.2.
3. **Impact test:** the test consists of a series of successive impacts while the laser measures each of the points in the mesh. For each of them, the system makes a measurement 10 times and average the results, obtaining an average FRF for each of the points in the mesh. Knowing the impact point and the response at each of the points, it is possible to extract the modal properties of the wing.
4. **Export the results:** the results will be later processed in Simcenter to update the numerical model, hence they are exported in universal file format (.uff) to ensure compatibility between software.

¹PSV-500 Scanning Vibrometer. Polytec, 2022. URL <https://www.polytec.com/us/vibrometry/products/full-field-vibrometers/psv-500-scanning-vibrometer>. Last accessed: 25th January 2022.

²vImpact Hammer. OMS Corporation, 2018. URL <https://www.omscorporation.com/products/hammer/index.html>. Last accessed: 25th January 2022.

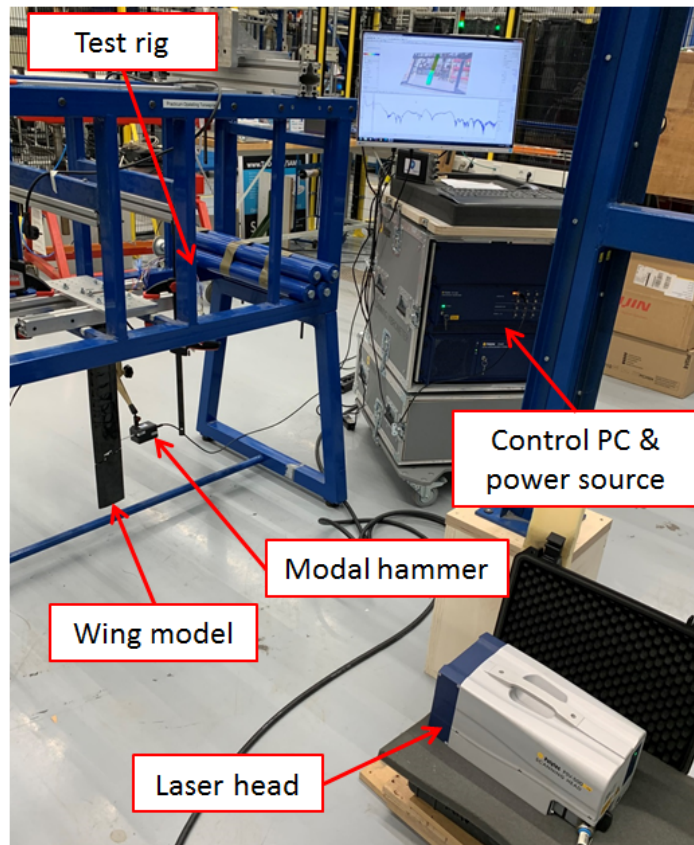


Figure B.1: Test setup used for the GVT using the SLDV system.

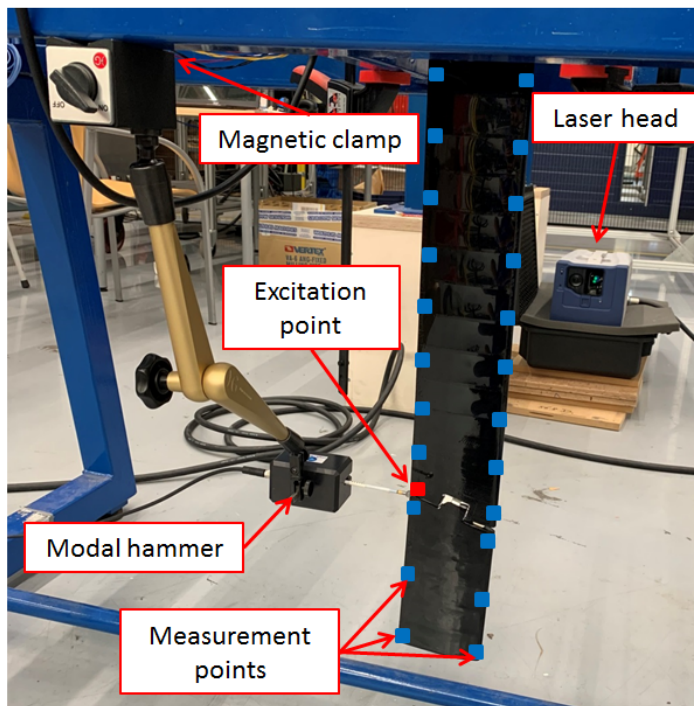


Figure B.2: Detail of the setup seen from behind including a grid with the measurement points and the point where the excitation is applied.

Bibliography

- [1] ZEROe. Airbus. URL: <https://www.airbus.com/innovation/zero-emission/hydrogen/zeroe.html>. Last accessed: 08 March 2021.
- [2] *Volume 18: Friction, Lubrication and Wear Technology*. ASM International, 10th edition, 1992. ISBN 978-0-87170-380-4.
- [3] *Annex 14 to the Convention on International Civil Aviation - Aerodromes*. ICAO, Montreal, Canada, 8th edition, 2018.
- [4] The albatross is inspiring tomorrow's aircraft wings. Airbus, 2019. URL: <https://www.airbus.com/newsroom/stories/the-albatross-is-inspiring-tomorrows-next-generation-of-aircraft-wings.html>. Last accessed: 18 February 2021.
- [5] AlbatrossONE - A revolutionary approach to aircraft wing design. Airbus, 2020. URL: <https://www.airbus.com/innovation/future-concepts/biomimicry/albatrossone.html>. Last accessed: 18 February 2021.
- [6] Freely flapping wing-tips on future aircraft just took a leap forward. Airbus, 2020. URL: <https://www.airbus.com/newsroom/stories/freely-flapping-wing-tips-took-a-leap-forward.html>. Last accessed: 18 February 2021.
- [7] CS-25 Amendment 26: Certification specifications and acceptable means of compliance for large aeroplanes. EASA, 2020. URL: <https://www.easa.europa.eu/document-library/certification-specifications/cs-25-amendment-26-0>. Last accessed: 18 March 2021.
- [8] 14 CFR § 25.341 - Gust and turbulence loads. FAA, 2020. URL: <https://www.govinfo.gov/app/details/CFR-2020-title14-vol1/CFR-2020-title14-vol1-sec25-341>. Last accessed: 18 March 2021.
- [9] Airbus. AlbatrossOne: Revolutionising Aircraft Wing Design. Youtube, 2019. URL: <https://www.youtube.com/watch?v=Rq2poT9pW3w>. Last accessed: 23 February 2021.
- [10] Airbus. AlbatrossONE achieves proof-of-concept on a small scale. Youtube, 2020. URL: <https://www.youtube.com/watch?v=R9SRn5n7enQ>. Last accessed: 23 February 2021.
- [11] John D Anderson. *Fundamentals of aerodynamics*. McGraw Hill, New York, 6th edition, 2017. ISBN 9781259129919.
- [12] O. Avin, D.E. Raveh, A. Drachinsky, Y. Ben-Shmuel, and M. Tur. An Experimental Benchmark of a Very Flexible Wing. In *AIAA Scitech 2021 Forum*, 2021. DOI: 10.2514/6.2021-1709.
- [13] P. J. Berkelman, L. L. Whitcomb, R. H. Taylor, and P. Jensen. A miniature microsurgical instrument tip force sensor for enhanced force feedback during robot-assisted manipulation. *IEEE Transactions on Robotics and Automation*, 19(5):917–921, 2003. DOI: 10.1109/TRA.2003.817526.
- [14] A. Castrichini, V. Hodigere Siddaramaiah, D.E. Calderon, J.E. Cooper, T. Wilson, and Y. Lemmens. Preliminary Investigation of Use of Flexible Folding Wing-Tips for Static and Dynamic Loads Alleviation. In *4th RAeS Aircraft Structural Design Conference*, 2014.

- [15] A. Castrichini, V. Hodigere Siddaramaiah, D.E. Calderon, J.E. Cooper, T. Wilson, and Y. Lemmens. Nonlinear Folding Wing Tips for Gust Loads Alleviation. *Journal of Aircraft*, 53(5):1391–1399, 2016. DOI: 10.2514/1.C033474.
- [16] A. Castrichini, J.E. Cooper, T. Wilson, A. Carrella, and Y. Lemmens. Nonlinear Negative Stiffness Wingtip Spring Device for Gust Loads Alleviation. *Journal of Aircraft*, 54(2):627–641, 2017. DOI: 10.2514/1.C033887.
- [17] A. Castrichini, T. Wilson, and J.E. Cooper. On the Dynamic Release of the Semi Aeroelastic Wing-Tip Hinge Device. In *6th RAeS Aircraft Structural Design Conference*, 2018.
- [18] A. Castrichini, T. Wilson, F. Saltari, F. Mastroddi, N. Viceconti, and J.E. Cooper. Aeroelastics Flight Dynamics Coupling Effects of the Semi-Aeroelastic Hinge Device. *Journal of Aircraft*, 57(2): 333–341, 2020. DOI: 10.2514/1.C035602.
- [19] Krishan K Chawla. *Composite materials*. Springer, New York, 3rd edition, 2012. ISBN 978-0-387-74365-3. DOI: 10.1007/978-0-387-74365-3.
- [20] R.C. Cheung, D. Rezgui, J.E. Cooper, and T. Wilson. Testing of a hinged wingtip device for gust loads alleviation. *Journal of Aircraft*, 55:1–18, 2018. DOI: 10.2514/1.C034811.
- [21] R.C. Cheung, C. Wales, D. Rezgui, J. E. Cooper, and T. Wilson. *Modelling of Folding Wing-Tip Devices for Gust Loads Alleviation*. 2018. DOI: 10.2514/6.2018-0462.
- [22] R.C. Cheung, D. Rezgui, J.E. Cooper, and T. Wilson. Testing of Folding Wingtip for Gust Load Alleviation of Flexible High-Aspect-Ratio Wing. *Journal of Aircraft*, 57(5):876–888, 2020. DOI: 10.2514/1.C035732.
- [23] A. Collar. The Expanding Domain of Aeroelasticity. *The Aeronautical Journal*, 50:613–636, 1946. DOI: 10.1017/S0368393100120358.
- [24] European Comission. The European Green Deal, 2019. URL: <https://eur-lex.europa.eu/legal-content/EN/TXT/?uri=CELEX:52019DC0640>. Last accessed: 08 March 2021.
- [25] European Comission. Sustainable and Smart Mobility Strategy - putting European transport on track for the future, 2020. URL: <https://ec.europa.eu/transport/sites/transport/files/legislation/com20200789.pdf>. Last accessed: 08 March 2021.
- [26] J. De la Cierva. Rotor-equipped aircraft (U.S. Patent No. 2,380,580). U.S. Patent Office, 1932. URL: <https://patents.google.com/patent/US2380580>.
- [27] J K S Dillinger, T Klimmek, M M Abdalla, and Z Gürdal. Stiffness Optimization of Composite Wings with Aeroelastic Constraints. *Journal of Aircraft*, 50(4):1159–1168, 2013. DOI: 10.2514/1.C032084.
- [28] G. Dussart, C. O’rourke, and T. Wilson. In-flight Wingtip Folding: Inspiration from the XB-70 Valkyrie. *International Journal of Aviation, Aeronautics, and Aerospace*, 6, 2019. DOI: 10.15394/ijaaa.2019.1343.
- [29] G. Dussart, S. Yusuf, and M. Lone. Identification of In-Flight Wingtip Folding Effects on the Roll Characteristics of a Flexible Aircraft. *Aerospace*, 6:63, 2019. DOI: 10.3390/aerospace6060063.
- [30] Y. Gibbs. NASA Tests New Alloy to Fold Wings in Flight. NASA, 2020. URL: <https://www.nasa.gov/centers/armstrong/feature/nasa-tests-new-alloy-to-fold-wings-in-flight.html>. Last accessed: 07 March 2021.
- [31] S. Guo, J. de Los Monteros, and Y. Liu. Gust Alleviation of a Large Aircraft with a Passive Twist Wingtip. *Aerospace*, 2:135–154, 2015. DOI: 10.3390/aerospace2020135.
- [32] V. Handojo, P. Lancelot, and R. De Breuker. *Implementation of Active and Passive Load Alleviation Methods on a Generic mid-Range Aircraft Configuration*. 2018. DOI: 10.2514/6.2018-3573.

- [33] Jimin He and Zhi-Fang Fu. *1 - Overview of modal analysis*, pages 1–11. Butterworth-Heinemann, Oxford, 2001. ISBN 978-0-7506-5079-3. DOI: 10.1016/B978-075065079-3/50001-2. URL: <https://www.sciencedirect.com/science/article/pii/B9780750650793500012>.
- [34] Jimin He and Zhi-Fang Fu. *Modal Analysis*. Butterworth-Heinemann, Oxford, 2001. ISBN 978-0-7506-5079-3. DOI: 10.1016/B978-0-7506-5079-3.X5000-1.
- [35] F. Healy, R.C. Cheung, T. Neofet, M.H. Lowenberg, D. Rezgui, J.E. Cooper, A. Castrichini, and T. Wilson. *Folding Wingtips for Improved Roll Performance*. 2021. DOI: 10.2514/6.2021-1153.
- [36] V. Hodigere Siddaramaiah, D.E. Calderon, J.E. Cooper, and T. Wilson. Preliminary Studies in the use of Folding Wing-Tips for Loads Alleviation. 2014.
- [37] J. Irving and R. Davies. Wingtip Device (U.S. Patent No. 7,275,722), 2007. URL: <https://patents.google.com/patent/US7275722B2/en>.
- [38] J. W. Joo, K. S. Na, and D. I. Kang. Design and evaluation of a six-component load cell. *Measurement*, 32(2):125–133, 2002. ISSN 0263-2241. DOI: 10.1016/S0263-2241(02)00002-7.
- [39] Christos Kassapoglou. *Review of Classical Laminated Plate Theory*, chapter 3, pages 33–53. John Wiley & Sons, Ltd, 2013. ISBN 9781118536933. DOI: 10.1002/9781118536933.ch3.
- [40] W.R. Krüger, J. Dillinger, R. De Breuker, and K. Haydn. Investigations of passive wing technologies for load reduction. *CEAS Aeronautical Journal*, 10(4):977–993, dec 2019. ISSN 18695590. DOI: 10.1007/s13272-019-00393-2.
- [41] United Nations. Paris Agreement, 2015. URL: https://unfccc.int/sites/default/files/english_paris_agreement.pdf. Last accessed: 08 March 2021.
- [42] J. Pattinson, T. Wilson, and M. Herring. High fidelity simulation of the folding wingtip for loads alleviation. In *15th International Forum on Aeroelasticity and Structural Dynamics (IFASD 2015)*, 2015.
- [43] Michiel Plooi, Glenn Mathijssen, Pierre Cherelle, Dirk Lefeber, and Bram Vanderborght. Lock your robot: A review of locking devices in robotics. *IEEE Robotics Automation Magazine*, 22(1): 106–117, 2015. DOI: 10.1109/MRA.2014.2381368.
- [44] R.L.M.F. Rouanet and F.V.A.J. Rey. Aircraft (U.S. Patent No. 2,186,558), 1940. URL: <https://patents.google.com/patent/US2186558A/en>.
- [45] M.H. Shirk, T.J. Hertz, and T.A. Weisshaar. Aeroelastic tailoring - Theory, practice, and promise. *Journal of Aircraft*, 23(1):6–18, 1986. DOI: 10.2514/3.45260.
- [46] Mark H. Smith, Michael E. Renzelmann, and Alan D. Marx. Folding Wing-Tip System (U.S. Patent No. 5,381,986), 1995. URL: <https://patents.google.com/patent/US5381986A/en>.
- [47] Terrence Weisshaar. Aeroelastic Tailoring - Creative Uses of Unusual Materials. In *28th Structures, Structural Dynamics and Materials Conference*, 1987. DOI: 10.2514/6.1987-976.
- [48] T. Wilson, A. Castrichini, A. Azabal, J.E. Cooper, R. Ajaj, and M. Herring. Aeroelastic Behaviour of Hinged Wing Tips. In *17th International Forum on Aeroelasticity and Structural Dynamics (IFASD 2017)*, 2017.
- [49] T. Wilson, M. Herring, J. Pattinson, J.E. Cooper, A. Castrichini, R. Ajaj, and H. Dhoru. An aircraft wing with a moveable wingtip device for load alleviation (WIPO Patent No. 2017/18832), 2017. URL: <https://patents.google.com/patent/WO20171118832A1/en>.
- [50] T. Wilson, A. Castrichini, J. Paterson, and R. Arribas Ardura. Non-linear aeroelastic behaviour of hinged wing tips. In *6th RAeS Aircraft Structural Design Conference*, 2018.
- [51] T. Wilson, J. Kirk, J. Hobday, and A. Castrichini. Small scale flying demonstration of semi aeroelastic hinged wing tips. In *19th International Forum on Aeroelasticity and Structural Dynamics (IFASD 2019)*, 2019.

-
- [52] Jan R. Wright and J.E. Cooper. *Introduction to Aircraft Aeroelasticity and Loads*. John Wiley & Sons, Ltd., 1st editio edition, 2007. ISBN 978-0470-85840-0.
- [53] Z. Wu, Y. Cao, and M. Ismail. Gust loads on aircraft. *The Aeronautical Journal*, 123(1266):1216–1274, 2019. DOI: 10.1017/aer.2019.48.